

LIQUID-INFUSED SURFACES FOR BOILING HEAT TRANSFER ENHANCEMENT AND MITIGATION OF CORROSION AND INORGANIC SCALING

Thesis

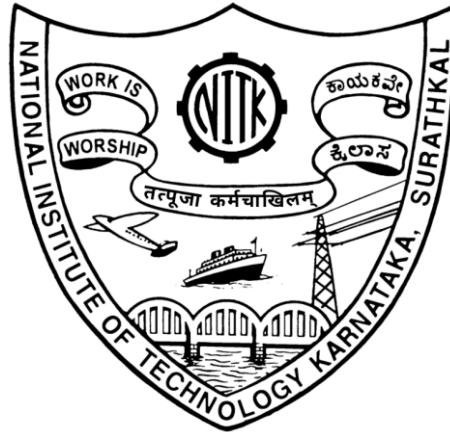
Submitted in partial fulfilment of the requirements for the degree of

DOCTOR OF PHILOSOPHY

by

A V V R PRASAD Y

(187027ME001)



DEPARTMENT OF MECHANICAL ENGINEERING
NATIONAL INSTITUTE OF TECHNOLOGY KARNATAKA,
SURATHKAL, MANGALORE-575025

OCTOBER 2024

LIQUID-INFUSED SURFACES FOR BOILING HEAT TRANSFER ENHANCEMENT AND MITIGATION OF CORROSION AND INORGANIC SCALING

Thesis

Submitted in partial fulfilment of the requirements for the degree of

DOCTOR OF PHILOSOPHY

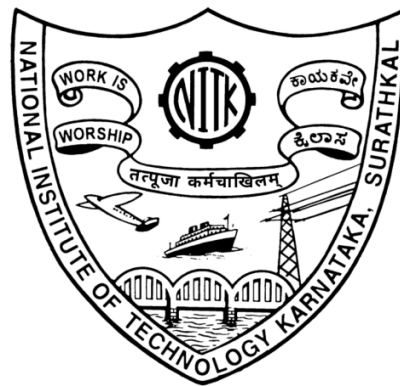
by

A V V R PRASAD Y

(187027ME001)

Under the guidance of

Prof. A. SATHYABHAMA



DEPARTMENT OF MECHANICAL ENGINEERING
NATIONAL INSTITUTE OF TECHNOLOGY KARNATAKA,
SURATHKAL, MANGALORE-575025

OCTOBER 2024

DECLARATION

I hereby declare that the Research Thesis entitled “**LIQUID-INFUSED SURFACES FOR ENHANCED BOILING HEAT TRANSFER AND MITIGATION OF CORROSION AND INORGANIC SCALING**” which is being submitted to the **National Institute of Technology Karnataka, Surathkal** in partial fulfilment of the requirements for the award of the Degree of **Doctor of Philosophy** in **Mechanical Engineering** is a *bonafide report of the research work carried out by me*. The material contained in this Research Thesis has not been submitted to any other Universities or Institutes for the award of any degree.

A V V R Prasad Y

Name and Signature of the Research Scholar

Register Number: **187027ME001**

Department of Mechanical Engineering

NITK, Surathkal - 575 025

Place: NITK, Surathkal

Date:

CERTIFICATE

This is to certify that the Research Thesis entitled “**LIQUID-INFUSED SURFACES FOR ENHANCED BOILING HEAT TRANSFER AND MITIGATION OF CORROSION AND INORGANIC SCALING**” submitted by **A V V R PRASAD Y (Register Number: 187027ME001)** as the record of the research work carried out by him, *is accepted as the Research Thesis submission* in partial fulfilment of the requirements for the award of the degree of Doctor of Philosophy.

Research Guide

Dr. A Sathyabhama

Professor

Department of Mechanical Engineering

National Institute of Technology Karnataka, Surathkal

Chairman-DRPC

Department of Mechanical Engineering

National Institute of Technology Karnataka, Surathkal

Date:

ACKNOWLEDGMENT

I wish to express my deepest gratitude to my research supervisor, **Prof. A Sathyabhama**, Department of Mechanical Engineering, National Institute of Technology Karnataka (NITK), Surathkal, for her unwavering support, guidance, and encouragement throughout my research journey. Her insights and suggestions have been invaluable, and her constant motivation has been a driving force behind the successful completion of this thesis. I extend my heartfelt thanks to the RPAC committee members, **Dr. N. Gnanasekaran** and **Dr. Darshak R. Trivedi** for their invaluable support and feedback during my research. Their expert opinions and constructive criticism have significantly contributed to my work. I am extremely grateful to **Dr. S.M. Murugendrappa**, Head of the Department of Mechanical Engineering, for his support and for providing the necessary resources and facilities. I also wish to thank the former Heads of the Department, **Dr. Ravikiran Kadoli**, **Dr. S. M. Kulkarni**, **Dr. Srikantha S. Rao**, **Dr Narendranath S** for their continuous encouragement.

My sincere thanks to **Dr. Krishna Kota** for inviting me to New Mexico State University, USA as an exchange visiting scholar, which was crucial for framing my research objectives. I am fortunate to have had the support of wonderful friends who stood by me through thick and thin. Special thanks to **Dr. Addisu**, **Ganesh**, **Rajan**, **Madan**, **Arjun**, **Dr. Jaypal**, **Dr. Jeena**, **Dr. Sreejith**, **Dr. Avdooth**, **Erick M**, **Kayla F**, **Javed Akthar**, **Sridhar Patgar**, **Surya Chand**, and **Jai Krishna** for their unwavering support.

I am blessed to have had the company of talented colleagues: **Dr. Prakash**, **Dr. Muthamil**, **Dr. Syam**, **Dr. Neeraj**, **Gopi**, **Dr. Rambabu**, **Vikas**, **Harish**, **Phani**, **Venkatapathy**, **Trilok**, **Kishore**, **Dr. Jagadeesh**, **Dr. Ujwal**, **Dr. Surya** and **Dr Prudhvi**. Their knowledge and companionship have been a constant source of support. Finally, I would like to thank my wife, dad, mom, brother and sister for being the pillars of strength and support all my life. Your unconditional love and confidence in me really helped me get through all the challenges I faced.

A V V R Prasad Y

ABSTRACT

One of the key sustainable development objectives of the United Nations is to ensure a reliable and consistent supply of fresh water. However, the growing population, industrialization, and urbanization have made it increasingly difficult to access an adequate amount of potable water. Consequently, desalination of brackish and seawater, which accounts for 97% of the global water resources, has emerged as an effective solution to provide potable water. In recent years, advancements in desalination research have led to increased capacity in large-scale commercial desalination plants using traditional technologies such as membrane and thermal desalination. However, these methods consume significant amounts of energy, typically obtained by burning fossil fuels and coal, leading to inevitable environmental concerns. Therefore, desalination methods those work on alternative/renewable energy sources, such as solar still, holds great potential for replacing traditional methods on a large scale.

Conventional solar still desalination works by evaporating fresh water from brackish sources, a process that is extremely slow. Research has been focused on enhancing the efficiency of solar stills. Historically, efforts were directed at maximizing the evaporation process to increase distillate output. A recent study suggested that instead of relying on evaporation, inducing nucleate boiling in the solar still basin by integrating it with tools that achieve concentrated solar power could significantly enhance distillate output. To maximize distillate output when nucleate boiling is induced, modifying the morphology of the solar still basin to enhance boiling heat transfer is necessary. Additionally, continuous and enhanced fresh water recovery from brackish sources poses challenges such as inorganic scaling and corrosion. In recent years, novel methods such as superhydrophobic surfaces and slippery liquid-infused surfaces have demonstrated excellent capabilities in inhibiting corrosion and inorganic scaling. However, concerns have been raised about their heat transfer capabilities due to insufficient liquid-surface contact on these surfaces.

In view of the above facts, the aim of this study was to demonstrate the effectiveness of a type of liquid-infused surface called binary surface (BiS) to inhibit scaling and corrosion without compromising the heat exchange efficiency. To this end, a highly-wetting Ultra-Omniphilic Surface (UOS) was prepared from a plain aluminum alloy surface (PS) using a bulk micro-manufacturing approach. Later, the sub-surface micro/nanocavities of UOS were infused with

a liquid lubricant to get BiS, which has two distinct superficial phases — solid phase as islands and liquid phase as puddles.

Saturated boiling heat transfer experiments were conducted on the BiS and the critical heat flux (CHF) and the boiling heat transfer coefficient (HTC) were measured. The results were compared with the UOS and PS. In addition, high-speed visualization was employed for capturing the bubble dynamics at different heat fluxes and parameters such as bubble departure diameter (D_d), bubble departure frequency (f), and nucleation site density (NSD) were measured. The results revealed that the boiling heat transfer performance of water on the BiS surpasses both the PS and the UOS. The HTC on the BiS was 1.33 times and two times larger than those on UOS and the PS, respectively. The CHF obtained on the BiS was comparable to that on the UOS and 1.47 times larger than that on the PS even though a considerable portion of the BiS surface area was covered with the liquid lubricant and unavailable for boiling. Remarkably, an inspection of the high-speed videos has suggested the presence of the same liquid lubricant as the reason for the better boiling heat transfer performance of the BiS. The liquid lubricant that was spread over the BiS as puddles was found to prevent the growth of large vapor bubbles and extend the isolated bubble regime by delaying the lateral coalescence of adjacent bubbles.

Lab-scale corrosion and scaling experiments were conducted on BiS in a simulated brackish water environment. Results indicated that BiS significantly outperformed PS and UOS in hindering scaling and corrosion. BiS exhibited nearly 50% less mass gain due to mineral deposition than on PS and UOS. Moreover, corrosion rates obtained from electrochemical and immersion tests showcased a notably slower metal degradation on BiS than on PS and UOS. This enhancement is attributed to well-distributed liquid puddles on BiS, promoting a smooth, defect-free surface that reduces foulants adhesion and shields the underlying metal from corrosion.

Keywords: Boiling heat transfer, Heat transfer coefficient, Critical heat flux, Bubble dynamics, Inorganic scaling, corrosion.

TABLE OF CONTENTS

TABLE OF CONTENTS	i
LIST OF FIGURES	v
LIST OF TABLES	ix
ABBREVIATIONS	xi
NOMENCLATURE	xiii
GREEK LETTERS	xv
SUBSCRIPTS	xv
CHAPTER 1	1
INTRODUCTION	1
1.1 BACKGROUND	1
1.2 MEMBRANE DESALINATION METHODS	2
1.3 THERMAL DESALINATION METHODS	2
1.4 SOLAR STILL	4
1.5 FACTORS AFFECTING THE PRODUCTIVITY OF THE SOLAR STILL	5
1.6 BOILING HEAT TRANSFER	10
1.7 INORGANIC SCALING	12
1.8 CORROSION	14
1.9 SCOPE OF THE PRESENT WORK	14
1.10 ORGANIZATION OF THE THESIS	15
CHAPTER 2	17
LITERATURE REVIEW	17
2.1 STUDIES ON ENHANCEMENT OF POOL BOILING HEAT TRANSFER THROUGH SURFACE MODIFICATIONS	17
2.2 STUDIES ON BUBBLE DYNAMICS	30
2.3 STUDIES ON MITIGATION OF INORGANIC FOULING	34
2.4 STUDIES ON CORROSION INHIBITION	39

2.5 CRITICAL LITERATURE REVIEW AND OBJECTIVES OF PRESENT WORK ...	44
CHAPTER 3	47
ENHANCEMENT OF BOILING HEAT TRANSFER	47
3.1 TEST SURFACE PREPARATION AND CHARACTERIZATION.....	47
3.1.1 SURFACE PREPARATION.....	47
3.1.2 BIS CHARACTERIZATION.....	49
3.2 EXPERIMENTAL TEST SETUP AND PROCEDURE.....	51
3.2.1 BOILING TEST SETUP.....	51
3.2.2 EXPERIMENTAL PROCEDURE.....	54
3.2.3 DATA REDUCTION.....	55
3.2.4 UNCERTAINTY IN MEASUREMENTS.....	56
3.2.5 REPEATABILITY AND VALIDATION OF THE TEST SETUP.....	58
3.3 HIGH-SPEED VISUALIZATION.....	61
3.3.1 PROCEDURE AND EQUIPMENT FOR HIGH-SPEED VISUALIZATION.....	61
3.3.2 ESTIMATION OF BUBBLE DEPARTURE DIAMETER.....	61
3.3.3 ESTIMATION OF BUBBLE DEPARTURE FREQUENCY.....	63
3.3.4 ESTIMATION OF NUCLEATION SITE DENSITY.....	64
3.4 RESULTS AND DISCUSSION.....	64
3.4.1 BOILING CURVES.....	64
3.4.2 HIGH-SPEED VISUALIZATION.....	71
CHAPTER 4.....	81
MITIGATION OF INORGANIC SCALING AND CORROSION.....	81
4.1 SIMULATED BRACKISH WATER.....	81
4.2 INORGANIC SCALING.....	82
4.2.1 TEST SECTION AND EXPERIMENTAL PROCEDURE.....	82
4.3 CORROSION.....	85
4.3.1 ELECTROCHEMICAL CORROSION TEST.....	85
4.3.2 IMMERSION CORROSION TEST.....	86
4.3 RESULTS AND DISCUSSION.....	87
4.3.1 MITIGATION OF INORGANIC SCALING.....	87
4.3.2 MITIGATION OF CORROSION.....	94

CHAPTER 5	105
CONCLUSIONS AND FUTURE SCOPE	105
5.1 CONCLUSIVE REMARKS	105
5.2 FUTURE SCOPE.....	108
5.3 Contribution of the present work to the United Nations Sustainable Development Goal	108
REFERENCES	111
LIST OF PUBLICATIONS BASED ON PH.D. RESEARCH WORK	123
BIO-DATA	125

LIST OF FIGURES

Figure 1.1 Projected water stress in each region by 2040 (Huang et al. 2024).....	1
Figure 1.2 Schematic of membrane desalination systems (a) RO (b) FO (Shahid et al. 2023).	3
Figure 1.3 Schematic of thermal desalination systems (a) MSF (b) MED (Al-hotmani et al. 2021).	4
Figure 1.4 Schematic of a conventional solar still (Pangwa and Msomi 2022).....	5
Figure 1.5 Self powered single slope solar still coupled with a flat plate collector (Al-Harashseh et al. 2022).	7
Figure 1.6 a)Single slope solar still with parabolic concentrator (Arunkumar et al. 2013) b) Solar still with parabolic concentrator associated to a self-traceable tracker (Maliani et al. 2020).	8
Figure 1.7 Double slope solar still with Fresnel lens (Choong et al. 2020).....	9
Figure 1.8 a) Single slope solar still with Fresnel lens b) Formation of nucleation site at focal point, Mu et al. (2019).	10
Figure 1.9 Various stages of water-formed scale deposition (b) Stability of the solution (Amjad and Demadis 2015).	13
Figure 3.1 Flow sequence of the BiS fabrication.....	48
Figure 3.2 Fluorescent spectrum of oil and BiS.....	49
Figure 3.3 Overlay of BiS reflection and fluorescence spectrums.	50
Figure 3.4 (a) BiS topography captured by optical microscope (b) Average contact angle on the BiS.....	51
Figure 3.5 Boiling heat transfer experimental test setip.	52
Figure 3.6 Test section.	54
Figure 3.7 Repeatability of test setup.....	59
Figure 3.8 Validation of test setup.	60
Figure 3.9 Measurement of bubble departure diameter.	62
Figure 3.10 Bounding box inserted on a) reference object and b) departing bubble.....	63
Figure 3.11 Boiling curve of PS showing regression lines in natural convection and nucleate boiling heat transfer.	66
Figure 3.12 Heat flux as a function of wall superheat.	67
Figure 3.13 HTC as a function of heat flux.	69
Figure 3.14 Jacob number as a function of heat flux	70
Figure 3.15 Comparison of measured bubble departure diameter with correlations.	72

Figure 3.16 Comparison of measured bubble departure diameter with literature.	74
Figure 3.17 Schematic of the observed bubble behavior on PS, UOS and BiS at various ebullition stages.	75
Figure 3.18 Variation of measured bubble departure frequency of PS, UoS, and BiS with Jakob number and comparison with other experimental works.	76
Figure 3.19 Comparison of the $f \cdot D_d$ of PS, UoS and BiS with those predicted from the correlations at different Jakob numbers.	77
Figure 3.20 Variation of the active NSD of PS,UOS, and BiS with Jakob number and comparison with predicted results and literature data.	78
Figure 3.21 Snap shots of boiling phenomenon at different heat fluxes (a-d) PS (e-h) UoS (i-l) BiS.	80
Figure 4.1 Laboratory scale setup to test the inorganic fouling effect on test surface.	84
Figure 4.2 The schematic of electrochemical corrosion test rig.	86
Figure 4.3 Variation of condensate collected with time on each test surface.	88
Figure 4.4 Depiction of precipitation mechanism on a) PS and b) BiS.	89
Figure 4.5 Variation of the net increase in the weight and condensate collected due to boiling of brackish water on each test surface.	90
Figure 4.6 Average roughness profile of the fouled surfaces captured by 3 D Profilometer on a) PS b) UOS and c) BiS.	92
Figure 4.7 FESEM images of PS, UOS, and BiS at various magnifications captured after exposure to boiling.	93
Figure 4.8 FESEM images of PS, UOS, and BiS captured after exposure to boiling for five hours.	94
Figure 4.9 OCP curves of PS, UoS, and BiS.	95
Figure 4.10 PDP curves of PS, UoS, and BiS.	97
Figure 4.11 Nyquist plots of PS, UoS, and BiS.	98
Figure 4.12 Equivalent Randle circuit.	99
Figure 4.13 Surface morphology of (a) PS (b) UOS, and (c) BiS subjected to electrochemical corrosion.	100

Figure 4.14 Corrosion rate of PS, UoS, and BiS at different temperatures obtained by weight loss method.	101
Figure 4.15 $\ln(\text{CR})$ Vs $1/T$ plots of PS, UOS, and BiS.....	104
Figure 4.16 $\ln(\text{CR}/T)$ Vs $1/T$ plots of PS, UOS, and BiS.	104

LIST OF TABLES

Table 2. 1 Summary of literature on boiling heat transfer enhancement	27
Table 2. 2 Summary of literature on bubble dynamics	33
Table 2. 3 Summary of literature on inorganic scaling mitigation strategies	38
Table 2. 4 Summary of literature on corrosion mitigation strategies	43
Table 3.1 Thermo-physical properties of cutting board (mineral) oil at $T = 40\text{ }^{\circ}\text{C}$	48
Table 3.2 Instruments used in boiling heat transfer equipment	53
Table 3.3 Bubble incipient temperature.	65
Table 3.4 Correlations for the prediction of bubble departure diameter.	73
Table 3.5 Correlations for the prediction of $f \cdot D_d$	76
Table 3.6 Correlations for the prediction of NSD.	78
Table 4. 1 The concentrations of cations and anions in the simulated brackish water.	82
Table 4.2 Results of the PDP measurements in simulated brackish water.	96
Table 4.3 Fitting results of EIS data in simulated brackish water.	99
Table 4.4 Activation parameters of PS UOS and BiS in simulated brackish water.	103

ABBREVIATIONS

AAO:	Aluminum Anodic Oxidation
BiS:	Binary Surface
BHT:	Boiling Heat Transfer
CA:	Contact Angle
CHF:	Critical Heat Flux
EIS:	Electro-chemical Impedance Spectroscopy
FESEM:	Field Emission Scanning Electron Microscope
FFF:	Fused Filament Fabrication
FO:	Forward Osmosis
HTC:	Heat Transfer Coefficient
IMRC:	Interconnected Microchannels with Re-entrant Cavities
LSP:	Laser Shock Processing
MAND:	Micro reactor Assisted Nano Deposition
MED:	Multi Effect Distillation
MSF:	Multi Stage Flash
NRFC:	Nucleating Reactor with Feeder Channels
NSD:	Nucleation Site Density
OCP:	Open Circuit Potential
PDP:	Potential Dynamic Polarization
PID:	Proportional Integral Derivative
PS:	Plain Surface
PTFE:	Poly Tetra Fluoro Ethylene
RO:	Reverse Osmosis
RT:	Room Temperature
SLIPS:	Slippery Liquid Infused Porous Surfaces
SNS:	Salt Nucleation Sites
TDS:	Total Dissolved Salts

UOS: Ultra Omniphilic Surface
VCI: Volatile Corrosion Inhibitor
WEDM: Wire Electrode Discharge Machining

NOMENCLATURE

A;	Surface area of specimen, m ²
B:	Arrhenius constant
C:	Constant used in Lemmert and Chawla correlation
C _p :	Specific heat, J/Kg·K
C _{sf} :	Surface-liquid constant used in Rohsenow correlation
D _d :	Bubble departure diameter (mm)
D _{max} :	Maximum diameter used in Tolubinsky and Kostanchuk correlation (mm)
D _{ref} :	Reference diameter used in Tolubinsky and Kostanchuk correlation (mm)
E _a :	Energy of activation
E _{corr} :	Corrosion potential
f:	Bubble departure frequency, s ⁻¹
g:	Acceleration due to gravity, m ² /s
h:	Planks constant
h _{lv} :	Latent heat, J/kg
I _{corr} :	Corrosion current density
Ja:	Jakob number, $\frac{c_p(T_s - T_{sat})}{h_{fg}}$
K _{Al} :	Thermal conductivity, W/m·K
N;	Avagadro's number
Pr:	Prandtl number
R:	Universal gas constant
T _s :	Test surface temperature, K
T _{sat} :	Saturation temperature of boiling liquid, K
t _g :	Bubble growth time
w:	Mass, grams
t _w :	Bubble waiting time
x:	Horizontal dimension of departing bubble in pixels
y:	Vertical dimension of departing bubble in pixels

Z' : Resistance
 Z'' : Capacitance

GREEK LETTERS

Δx :	Distance between consecutive thermocouples, mm
ΔH :	Enthalpy of activation
ΔS :	Activation entropy
ΔT_{ref}	Reference temperature used in Tolubinsky and Kostanchuk correlation, K
θ :	Contact angle, degree or radian
μ :	Dynamic viscosity, Pa.s
ρ :	Density, Kg/m ³
ρ^* :	$\frac{(\rho_l - \rho_v)}{\rho_v}$
σ :	Surface tension, N/m
σ_q :	Standard deviation of heat flux in repeatability tests
σ_{T_s} :	Standard deviation of surface temperature in repeatability tests
σ_{HTC} :	Standard deviation of HTC in repeatability tests

SUBSCRIPTS

ct:	Charge transfer
l:	Liquid
v:	Vapor
s:	Solution

CHAPTER 1

INTRODUCTION

1.1 BACKGROUND

The scarcity of safe and clean drinking water remains a significant challenge in modern day world. It is projected that approximately 70% of the global population will face inadequate access to water resources by 2025 (Huang et al. 2024). As illustrated in Fig 1.1, by 2040, several continents will confront extreme water stress due to rapid industrialization, population growth, and climate change. According to a report published by international desalination association (Buros 2000), 94% of the water available on the earth is seawater and saline aquifers. Of the remaining 6% freshwater, 27% is stored in glaciers, 72% is underground water, and less than 1% is directly available for human consumption. Consequently, in order to achieve "water security" defined as the availability of adequate and clean water resources to meet growing demand while ensuring the sustainability of water ecosystems—there is a growing global trend towards extracting potable water from unusable sources such as brackish and seawater.

Global water stress by 2040

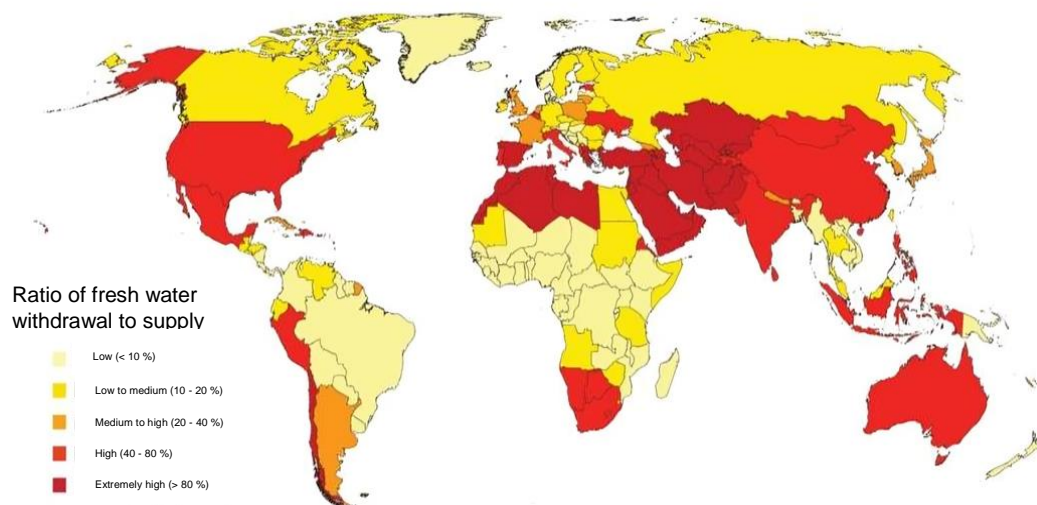


Figure 1.1 Projected water stress in each region by 2040 (Huang et al. 2024).

Over 15,900 desalination plants are operational across the world with a capacity of producing a fresh water of 95.37 million m³/day (Jones et al. 2019). With the increase in the rate of fresh water consumption, the desalination capacity has to be increased proportionally. Based on the operation technique, traditional desalination methods are broadly classified into two main categories, Membrane desalination and Thermal desalination(Lin et al. 2021).

1.2 MEMBRANE DESALINATION METHODS

Membrane desalination processes, such as Reverse Osmosis (RO) and Forward Osmosis (FO), use a semi-permeable membrane that allows water molecules to pass through while blocking salts and other dissolved solids (Shahid et al. 2023). These processes have become popular for domestic use due to their simple operating principles and compact designs. However, a major concern with membrane desalination is that the amount of water rejected is higher than the amount produced. The rejection rate increases over time due to the fouling of the membrane pores, which eventually leads to a decline in healthy minerals required in potable water, reducing its pH value and making the water acidic. For the past few decades, research has been focused on developing innovative methods to reduce the fouling effect in membrane desalination and increase productivity (Al-Abri et al. 2019; Najid et al. 2022). Additionally, it is important to note that membrane desalination is energy-intensive. The energy required to diffuse the feed water through the membrane varies with the type of feed water supply. For example, a seawater RO plant consumes 3-6 kWh of electricity for every cubic meter of fresh water produced (Liyanaarachchi et al. 2014). This energy consumption further increases with membrane fouling.

1.3 THERMAL DESALINATION METHODS

Thermal desalination systems (Fig. 1.3), such as Multi-Stage Flash (MSF) desalination and Multi-Effect Distillation (MED), involve the heating and phase change of saline water into steam, which is then condensed back into liquid form, leaving salts and impurities behind (Al-hotmani et al. 2021). Thermal desalination systems have lower brine rejection rates and produce high-purity water with low salt content after a single

desalination cycle. Before 1980's, MED and MSF were the major desalination techniques around the globe, accounting for 84% of the total desalinated water. However, higher capital costs and lower energy efficiencies in the installation and operation of MSF and MED throttled the usage of thermal desalination methods (Shaffer et al. 2013).

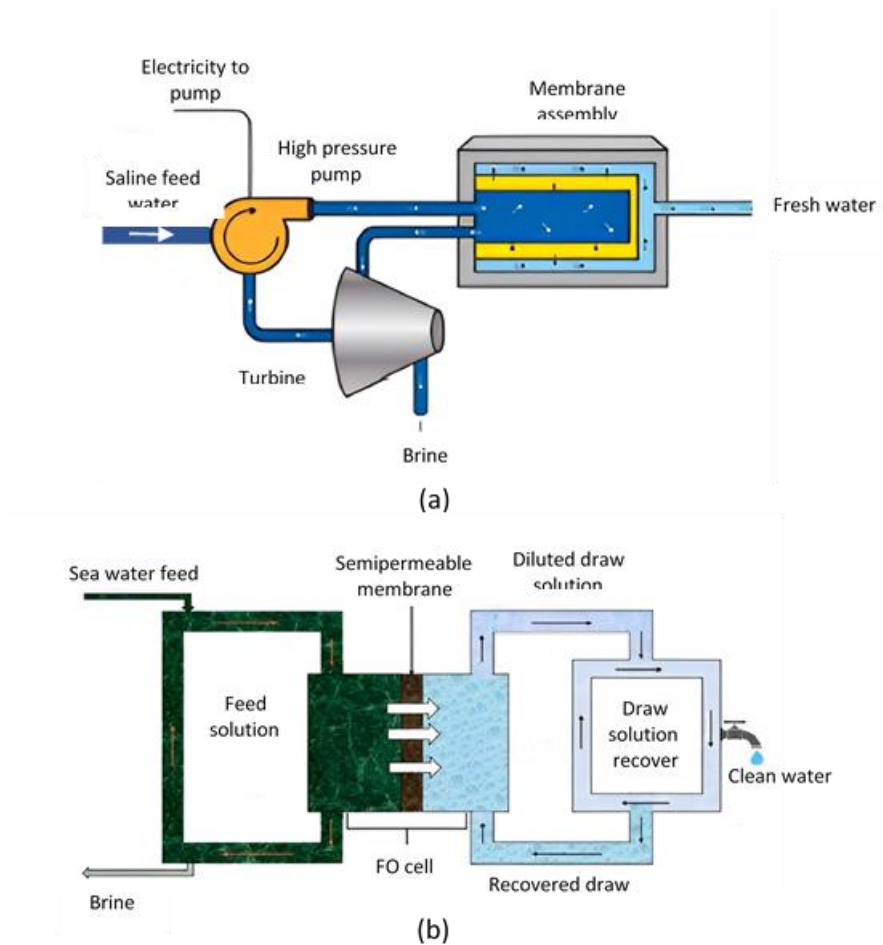


Figure 1.2 Schematic of membrane desalination systems (a) RO (b) FO (Shahid et al. 2023).

Further, it is noteworthy to mention that the energy supply for both membrane and thermal desalination methods is usually fulfilled by burning large amounts of coal/fossil fuels (Ghaffour et al. 2013). Consequently, installing large-capacity desalination plants is feasible only in energy-affluent areas, but using such energy sources leads to severe

environmental pollution. Therefore, it is essential to explore desalination methods that utilize alternative energy sources, such as solar stills.

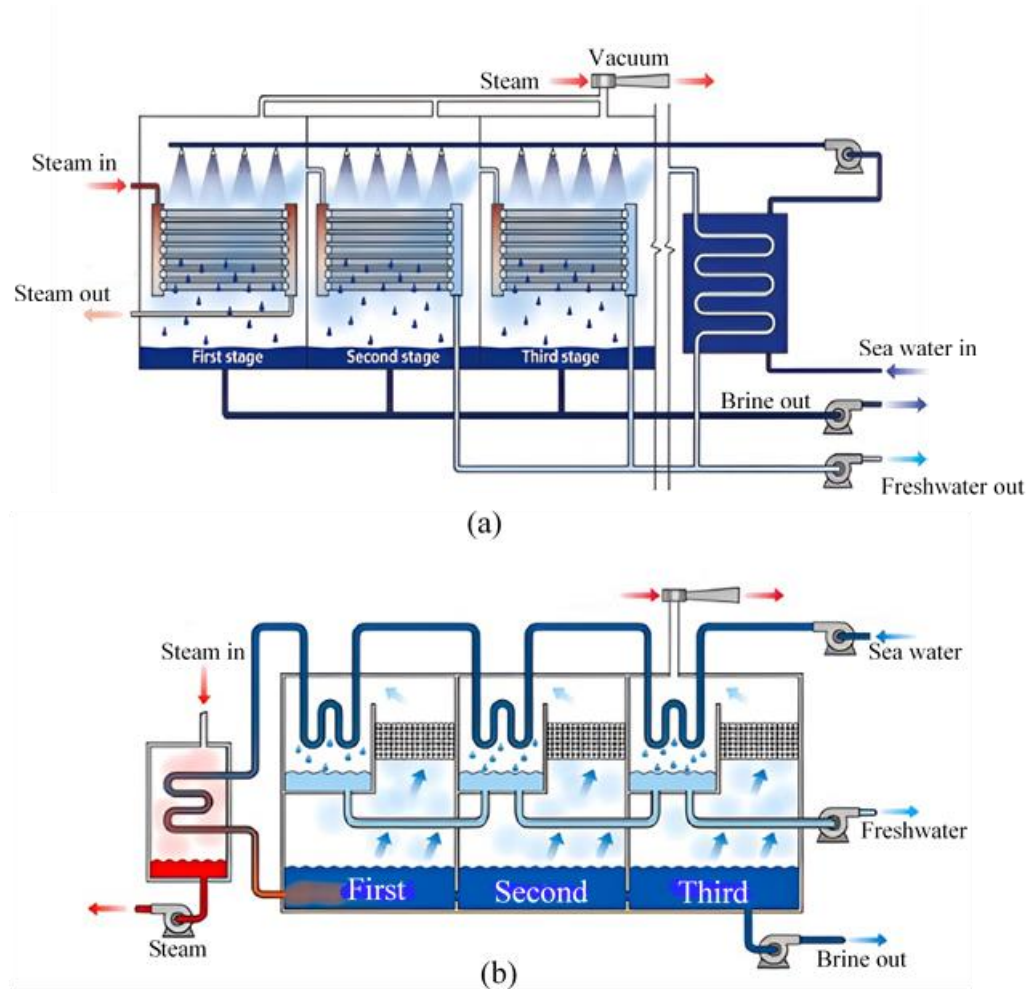


Figure 1.3 Schematic of thermal desalination systems (a) MSF (b) MED (Al-hotmani et al. 2021).

1.4 SOLAR STILL

Due to the geographical coincidence between high solar energy availability and a severe water shortage, solar stills are potential alternative to the traditional desalination methods. Solar stills operate by evaporating sea or brackish water using solar energy and then condensing the generated vapor into safe drinking water. The process of desalination in a solar still is very slow and less productive. Moreover, large-

scale desalination requires vast open spaces and significant capital investments, increasing the production cost of potable water. Therefore, despite the ability of a solar still to produce fresh water without consuming high-grade energy, it can only be commercialized if its productivity is increased.

1.5 FACTORS AFFECTING THE PRODUCTIVITY OF THE SOLAR STILL

Climatic conditions, operational and design parameters influence the productivity of the solar still. Over the past few decades, decent progress has been made to improve the productivity of the solar still (Pangwa and Msomi 2022). The main components of a conventional solar still (Fig. 1.4) are an insulated water basin, feed water supply tank, freshwater collecting tray coupled with a collecting tank, and a transparent glass cover positioned at an angle facing the sun. The productivity of the solar still is directly proportional to the intensity of solar radiation (Almuhanna 2013). But, a few other factors can also be optimized to increase the productivity of the solar still.

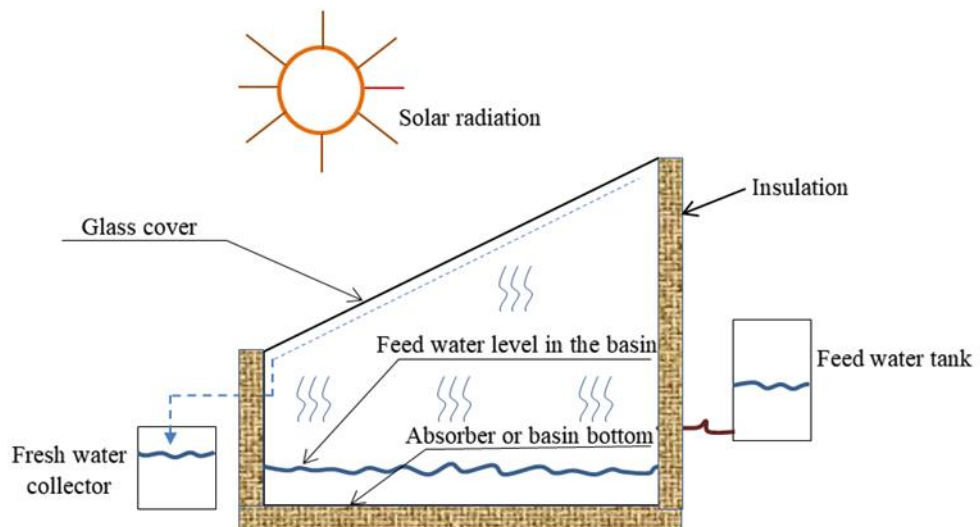


Figure 1.4 Schematic of a conventional solar still (Pangwa and Msomi 2022).

The temperature difference between the feed water in the basin and the condensing glass cover is the key factor for enhanced distillate output. In order to increase this

temperature difference, it is necessary to either reduce the average temperature of the glass cover or increase the average temperature of the working fluid. Khechekhouché et al. (2021) investigated the impact of glass cover thickness on its average temperature. The results showed that reducing the glass cover thickness leads to minimized heat losses to the surroundings, improved solar transmittance, and a higher temperature difference between the glass cover and feed water. El-Sebaey et al. (2022) observed that lowering the level of feed water in the basin results in a faster rise in temperature, as the solar radiation directly affects the feed water. Elango and Kalidasa Murugavel (2015) demonstrated that insulating the basin effectively reduces heat losses and helps maintain feed water temperatures. To ensure a constant temperature difference during off-shine periods, researchers have modified the basin surface in various ways, such as embedding black-coated jute cloth (Sakthivel et al. 2010), using floating wicks (Manikandan et al. 2014), employing V-shaped corrugated wicks (Shalaby et al. 2016), incorporating phase-change materials (Faegh and Shafii 2017), using porous fins (Panchal and Sathyamurthy 2020), and experimenting with pond fibres (Suraparaju et al. 2021). Despite these efforts to enhance productivity, the limited intensity of solar radiation remains a constraint on the production capacity of the solar still.

In order to maximize the possible radiation to reach the basin absorber, the orientation and inclination of the glass cover were tested in various studies. The results suggested that the tilt angle of the glass cover should be equivalent to the local latitude (Singh and Tiwari 2004). In the regions of higher latitudes, single slope solar stills were more productive when placed in such a manner that the glass cover faces towards the north in the southern hemisphere and towards the south in the northern hemisphere. Whereas in the areas of lower latitude, double slope solar stills perform well when the slopes of the glass cover face east and west directions (Jani and Modi 2018). Besides channelizing solar radiation, external aids were also investigated to concentrate and amplify the solar radiation.

An external flat plate solar collector/concentrator was attached to a conventional solar still (Fig. 1.5) to increase the distillate output (Al-Harashseh et al. 2022). Solar concentrators are devices that absorb solar energy. When feed water circulates in the pipes passing through the collector, the feed water gets heated up and flows into the

solar-still basin at higher temperatures, resulting in enhanced freshwater output. However, this process brings more surface area in contact with the saline water, which is susceptible to scaling and corrosion. Therefore, instead of running the feed water through a flat plate collector, Arunkumar et al. (2013) replaced a conventional solar still basin with a hemispherical basin and associated a parabolic concentrator to it (Fig. 1.6 (a)). The sun-light which reflected from the concentrator focusses on the absorber basin and was able to increase the feed water temperatures in the basin to 90 °C during the maximum radiation hours. The effectiveness of this combination was further increased when a self-traceable solar tracker was added to it (Fig. 1.6 (b)) (Maliani et al. 2020).

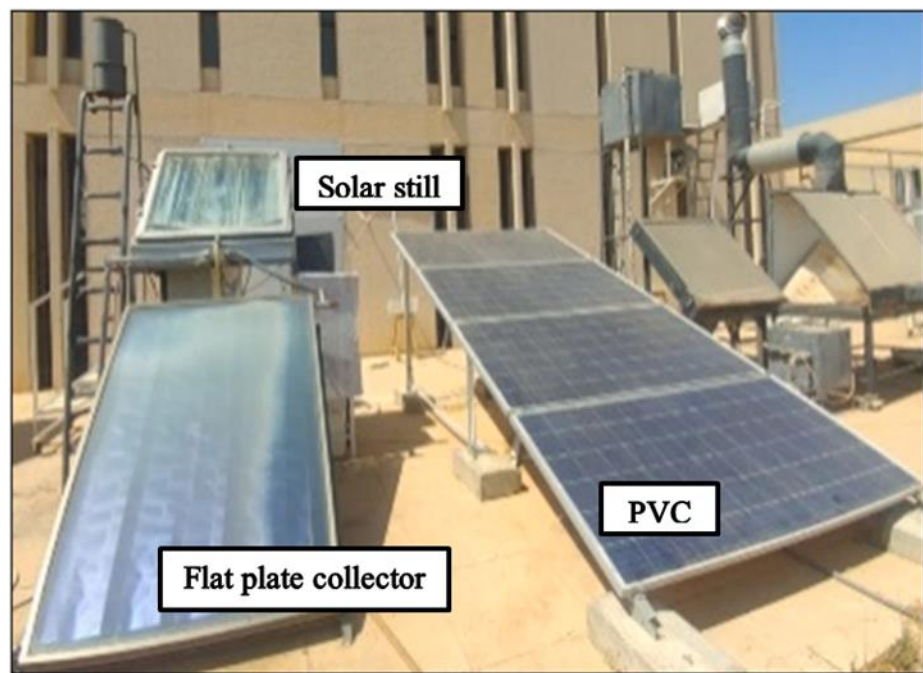
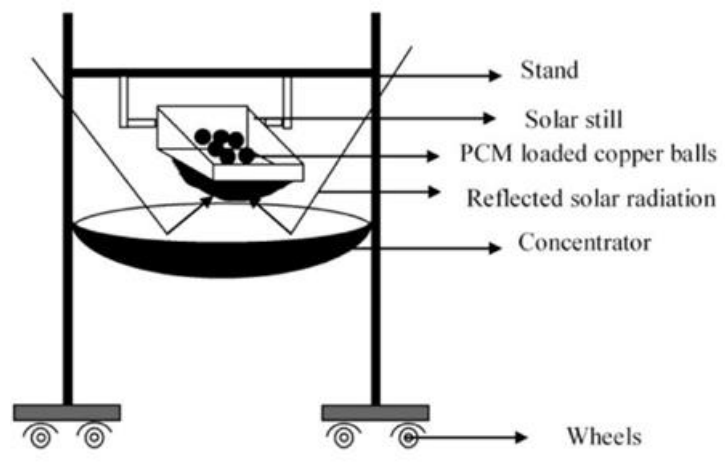
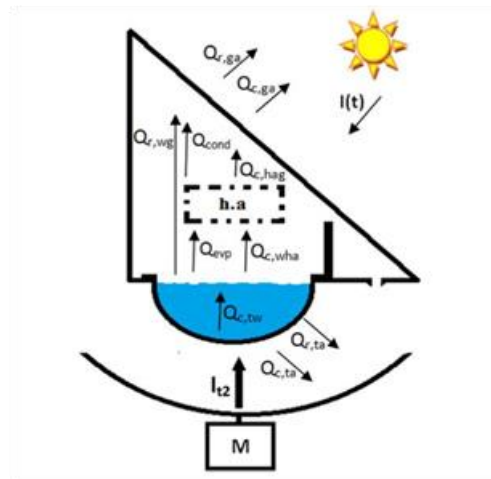


Figure 1.5 Self powered single slope solar still coupled with a flat plate collector (Al-Harashsheh et al. 2022).



(a)



(b)

Figure 1.6 a) Single slope solar still with parabolic concentrator (Arunkumar et al. 2013) b) Solar still with parabolic concentrator associated to a self-traceable tracker (Maliani et al. 2020).

Recent studies on solar desalination examined the feasibility of refraction based optical methods to improve the distillate output. Flat Fresnel lens were assembled on a double slope solar still (Fig. 1.7) to improve the distillate outputs for small-scale applications (Choong et al. 2020). The Fresnel lens refracts the sunlight to create a hot spot at the focal point and was observed to increase the absorber temperature. It was concluded that the average daily output has increased with the addition of Fresnel lens, although

the location does not receive strong direct normal irradiation. Mu et al. (2019) designed a single slope solar still integrated with Fresnel lens (Fig. 1.8 (a)) such that the focal point was constantly located at the basin bottom. It was observed that bubble nucleation takes place at the focal point (as shown in Fig. 1.8 (b)). It was reported that the obtained distillate output from the solar still integrated with Fresnel lens was significantly higher (467%) than the distillate collected from a conventional solar still. The enhanced distillate output was attributed to the occurrence of nucleate boiling at basin bottom.



Figure 1.7 Double slope solar still with Fresnel lens (Choong et al. 2020).

In summary, considerable progress has been made over the years in improving the efficiency of solar stills. While the focus has traditionally been on enhancing the evaporation process to boost distillate output, recent research indicates that inducing nucleate boiling at the basin bottom plays a significant role in the phase-change process. Despite these advancements, continuous freshwater generation inevitably leads to issues like scaling and corrosion at the basin bottom. To address these challenges, the materials used for the solar still basin should be replaced with those that resist corrosion in marine environments, such as aluminum Al 6061 (Peng et al. 2022). Additionally, the basin topography should be modified to improve boiling heat transfer and prevent scale formation.

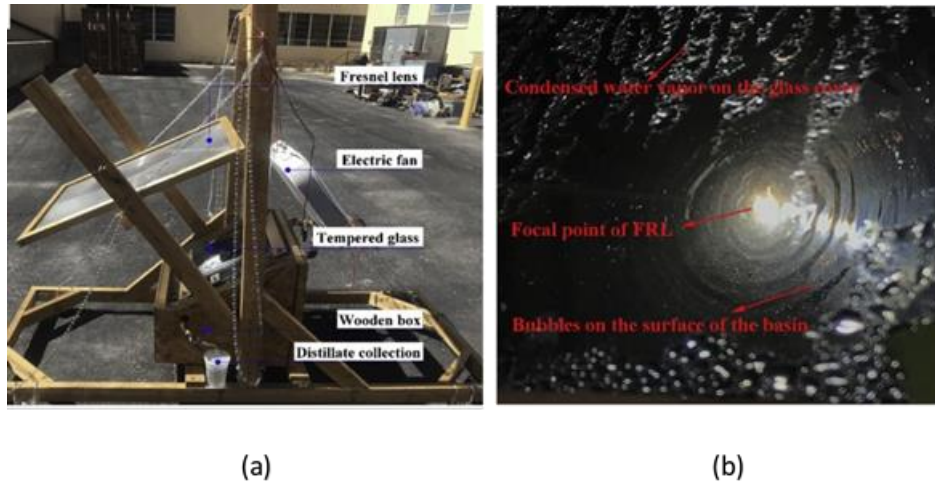


Figure 1.8 a) Single slope solar still with Fresnel lens b) Formation of nucleation site at focal point, Mu et al. (2019).

1.6 BOILING HEAT TRANSFER

Boiling heat transfer (BHT) is a complex process of heat transfer through phase change. It initiates with the creation of vapor bubbles at specific locations on the heated surface, which are referred to as nucleation sites. These sites are typically associated with surface imperfections like roughness or micro structures. When a liquid comes into contact with the heated surface, its temperature rises and exceeds the saturation point of the liquid, leading to the formation of bubbles at the nucleation sites. These bubbles then grow and detach from the heated surface, carrying away a significant amount of latent heat. This heat transfer occurs at a finite temperature difference between the heated surface (T_s) and the saturation temperature of the liquid (T_{sat}), known as wall superheat ($T_s - T_{sat}$). An increase in wall superheat raises the density of active nucleation sites (NSD), which in turn accelerates bubble formation, growth, and departure, thereby increasing the heat transferred to the liquid. The enhancement of heat transfer persists until it reaches the critical point - Critical heat flux (CHF) - which signifies the conclusion of the nucleate BHT process. At this stage, a vapor blanket forms between the surface and the liquid bulk, causing a sudden rise in the temperature of the heat source. The effectiveness of pool boiling relies on the amount of heat transferred from the surface before reaching the CHF, which is quantified as the ratio of heat flux to wall

superheat, known as the heat transfer coefficient (HTC). The HTC can be influenced by the conditions of the heater surface, which can impact various aspects of bubble dynamics such as nucleation, growth, bubble waiting time (t_g), bubble growth time (t_w), bubble departure diameter (D_d), bubble departure frequency (f) and active NSD.

The conditions of the heater surface can be adjusted by integrating micro/nano-scale structures or by altering the wettability of a sessile droplet on the heater surface. Micro/nano structures increase the available surface area, enhancing BHT by providing more active nucleation sites. However, this additional surface area also makes the heater surface more susceptible to corrosion and inorganic scaling. Alternatively, altering the surface wettability through changes in hierarchical roughness can influence factors such as bubble incipience temperatures and liquid replenishment to the nucleation sites. However, the deposition of inorganic minerals on the heater surface during desalination alters the hierarchical roughness, causing the surface to lose its wettability properties.

In a recent study, Holguin et al. (2017) engineered a novel surface called Binary Surface (BiS) by infusing a low-conductive liquid lubricant into a high-conductive metal substrate. The BiS topography is characterized by solid, high-conductive islands surrounded by low-conductive lubricant puddles. This unique feature of the BiS causes in-plane temperature variations during boiling and induces separate pathways for the incoming rewetting liquid and outgoing vapor bubbles. This mechanism enhances HTC and delays CHF simultaneously. Although the lubricant puddles on the BiS partially cover the surface area available for heat exchange, the results indicate that these surfaces can significantly enhance BHT. This suggests that creating efficient liquid-vapor pathways holds great potential for improving BHT, making the BiS suitable for applications where enhanced heat transfer is desired without increasing the surface area, such as in desalination.

1.7 INORGANIC SCALING

Brackish water contains dissolved mineral salts such as carbonates and sulfates of calcium and magnesium at saturation levels (Jiang et al. 2017). When pure water is recovered from brackish feeds, the salt concentration increases, leading to the supersaturation of these salts and a higher likelihood of inorganic scaling or fouling on the substrate in contact.

Scaling is a multi-stage phenomenon as depicted in Fig 1.9 (a). It begins with the supersaturation of sparingly soluble salts. Once supersaturation is achieved, oppositely charged ionic species collide, forming ion pairs that act as nucleation sites for inorganic scaling, known as salt nucleation sites (SNS). SNS can form in two ways:

1. Heterogeneous SNS: Forms at liquid-solid interfaces or on suspended solid particles in the solution.
2. Homogeneous SNS: Forms in the bulk of the liquid and later deposits on the surface through convection.

Scale formation results from both SNS mechanisms. The dominance of one mechanism over the other depends on factors such as local supersaturation, temperature and pH of the solution, concentration polarization, and the presence of other foulants like organic or colloidal matter (Matin et al. 2019). As SNS stabilize, they grow into crystals by accumulating more ion pairs. Crystal growth into a visible scale is influenced by solution stability and surface conditions (Amjad and Demadis 2015). The degree of supersaturation drives crystal growth (Fig 1.9 (b)). At lower supersaturation levels, sub-microscopic crystals of mineral salts dissolve more easily, reducing local supersaturation and limiting crystal growth. As salt concentration increases, the solution becomes unstable, inducing spontaneous crystallization and accelerating precipitation (Gates and Caraway 1967). Surface conditions, such as microscopic crevices and cracks, are ideal for SNS and crystal growth (Griffith 1921).

As the solution becomes unstable, crystal kinetics and the diffusion of fouling agents at the solid-liquid interface accelerate, leading to the adhesion of these agents to the

substrate. The DLVO (Derjaguine-Landau-Verwey-Overbeek) theory explains this adhesion through a balance of attractive van der Waals forces and repulsive electrostatic charges between the fouling agents and the substrate (Derjaguin 1954; Verwey 1947). Minimizing the surface area in contact between precipitates and the substrate can reduce adhesion (Visser 1995).

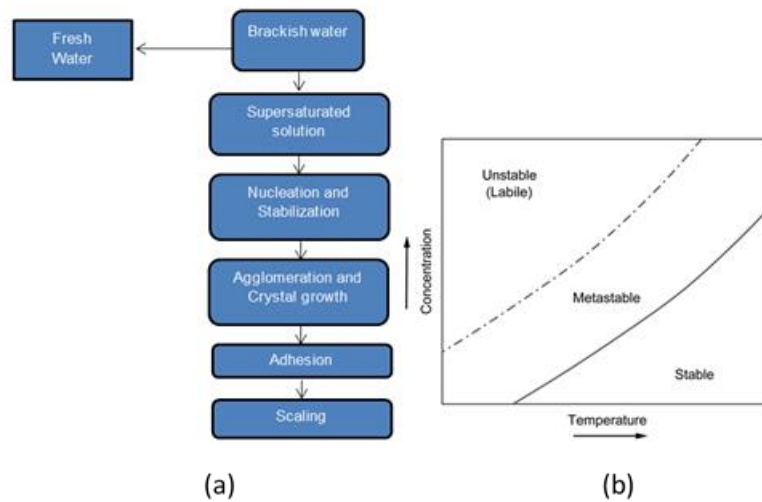
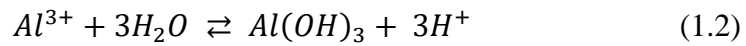


Figure 1.9 Various stages of water-formed scale deposition (b) Stability of the solution (Amjad and Demadis 2015).

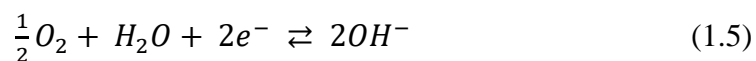
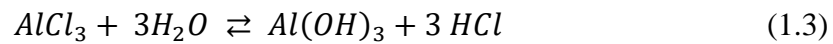
Precipitation of inorganic foulants is unavoidable at high degrees of supersaturation. Desalination plants use pre-treatment of brackish feeds and the addition of threshold agents to reduce scaling tendencies, but these methods only delay precipitation. Once solutes begin to precipitate, surface conditions influence the interactive forces between deposited foulants and the substrate, leading to adhesion. Hence the recent studies on mitigating inorganic scaling focus on reducing the available SNS and minimizing the interactive forces between the substrate and foulants.

1.8 CORROSION

Chloride ions (Cl⁻) are among the major constituents of brackish water. Aluminum substrates possess a corrosion resistive oxide film, but prolonged exposure to a chloride-rich environment causes this film to erode, leading to the formation of aluminum chloride complexes and pitting corrosion (Xhanari and Finšgar 2019). The anodic reaction is as follows.



The anodic dissolution takes place as per equation 1.1, and forms pits on the substrate. Out of all generated Al^{3+} ions, few diffuse outside pitting and forms aluminum hydroxide layer on the edges of pitting as per equation 1.2, which hinders the outward dispersion of Al^{3+} ions. However, over the period of time, excessive concentrations of positive Al^{3+} ions enhances the acidic nature at the anode. Hence, the external Cl⁻ ions enter the pits to maintain the charge balance by formation of the aluminum chloride. Accordingly, the following reactions occur at cathode.



Hence, any strategies that slow down corrosion reactions and surface modifications that minimize contact between the corrosive medium and the substrate can mitigate corrosion.

1.9 SCOPE OF THE PRESENT WORK

The present work focuses on developing a surface that is easy to implement and enhances boiling heat transfer while reducing corrosion and inorganic scaling. During the desalination of brackish feeds in a solar still integrated with concentrated solar power, boiling, corrosion, and inorganic scaling occur simultaneously. However, these factors are evaluated separately on the developed surface, as each factor may influence the others. This method helps assess the effectiveness of the developed surface for each

factor. Standard pool boiling tests are conducted using deionized water, while simulated brackish water is used for inorganic scaling and corrosion tests.

1.10 ORGANIZATION OF THE THESIS

Chapter 1: Introduction – This chapter provides a brief discussion on the global water crisis, limitations of conventional desalination methods, need for the desalination methods integrated with alternative energy resources and the associated challenges.

Chapter 2: Literature review – This chapter presents a literature review on research related to strategies for enhancing boiling heat transfer and studies on the visualization of bubble dynamics. Additionally, it covers studies on the mitigation of inorganic scaling and corrosion. At the end of this chapter, the scope and objectives of the present work are defined.

Chapter 3: Enhancement of boiling heat transfer – The chapter outlines the surface preparation, characterization, and demonstration of the BHT test section, along with the experimental procedure, data reduction, uncertainty analysis, and validation. Additionally, it discusses the setup and procedure for high-speed visualization and the estimation of bubble dynamics parameters. Further, this chapter details the experimental outcomes of BHT such as CHF and HTC on modified and normal test surfaces. Bubble dynamics on regular and modified surfaces and the corresponding effect on BHT enhancement.

Chapter 4: Mitigation of inorganic scaling and corrosion – This chapter covers the test setup and procedure for inorganic scaling and electrochemical corrosion tests, as well as the estimation of corrosion rate from immersion corrosion tests. Further, this chapter evaluates the effectiveness of BiS in alleviating inorganic scaling and corrosion in a simulated brackish water environment. It also details the qualitative analysis of fouled and corroded surfaces by studying the surface roughness profiles and FESEM micrographs.

Chapter 5: Conclusions and future scope – This chapter covers the conclusions and future research recommendations of the present work.

CHAPTER 2

LITERATURE REVIEW

A comprehensive analysis of the existing literature was undertaken to investigate the influence of surface conditions on enhancing the heat transfer during boiling and the associated bubble dynamics. Furthermore, the review encompassed an investigation into the origin and preventive measures for inorganic fouling and corrosion in a brackish water environment. In order to ensure a coherent and lucid presentation, the literature review has been structured into distinct sections.

2.1 STUDIES ON ENHANCEMENT OF POOL BOILING HEAT TRANSFER THROUGH SURFACE MODIFICATIONS

Experimental studies have been carried out by using various types of surfaces since last two decades. The details of pool boiling study on different types of surfaces are discussed below and summarized in Table 2.1.

Walunj and Sathyabhama (2018) conducted a study on improving BHT using open micro-channels. The study focused on comparing the performance of rectangular, parabolic, and stepped micro-channels on a copper test piece, while also analysing the impact of channel shape and geometrical parameters on BHT. The findings of the study revealed that all micro-channel geometries contributed to an improvement in the heat transfer rate. Notably, the transformation of the rectangular channel into parabolic and stepped micro-channels resulted in a significant enhancement. Among the various micro-channel geometries tested, the stepped micro-channel demonstrated the highest heat transfer performance. This superior performance can be attributed to the enhanced liquid supply facilitated by the stepped design.

Saffari et al. (2020) examined the impact of inclined meso channels on BHT. The meso channel structures were fabricated on a copper surface using the wire electrode discharge machining (WEDM) technique. A notable improvement in the HTC was noted when transitioning the surface design from a flat plate to a vertical meso channel surface and subsequently to an inclined meso channel surface. The study revealed that reducing the channel inclination and increasing the channel depth resulted in an

expansion of the surface area, leading to the enhanced HTC. Additionally, it was observed that inclined channels effectively trapped vapor and aided in the nucleation process of the subsequent bubble, thereby increasing the frequency of bubble departure.

Jiang et al. (2021) examined how cylindrical array structures impact the BHT performance using deionized water as the working fluid. The findings revealed a noteworthy enhancement in HTC for all cylindrical pillar arrays in comparison to a smooth surface. This improvement was attributed to the decrease in bubble incipience temperature. Additionally, the study discovered that reducing the spacing between the pillars further enhanced the BHT performance by facilitating the departure of bubbles and promoting the rapid replenishment of liquid to the dry area.

Jaswal et al. (2023) conducted an experimental analysis on rectangular and trapezoidal finned surfaces to investigate the impact of fin spacing and fin height on the BHT performance. The results revealed that increasing the height of the fins had a positive effect, as it provided a larger surface area for bubble nucleation and convective heat transfer. On the other hand, increasing the fin spacing had a detrimental effect on the BHT due to the formation of smaller discrete bubbles and a reduced amount of heat carried away by a single bubble. Additionally, the study concluded that the HTC is directly proportional to the available area for heat exchange. This is because the additional surface area increases the active NSD on the test surface, thereby enhancing BHT.

Godinez et al. (2019) conducted a study on the influence of aluminum microporous coatings on BHT using saturated distilled water under atmospheric pressure conditions. The report suggests that surfaces with coatings displayed higher values of HTC and CHF in comparison to uncoated surfaces. The optimal coating thickness for different mean particle diameters were determined. The increase in HTC was linked to the decrease in bubble incipience temperature on the coated surfaces. Additionally, the study revealed that active NSD on the coated surface increased with the thickness of the coating, but decreased after reaching an optimal level. These findings align with those of studies on copper microporous coatings (Jun et al. 2016). However, it was noted that the CHF of aluminum microporous coatings did not show significant

improvement compared to copper microporous coatings, this could be due to reaching the highest possible value as a result of the hydrodynamic limit.

Yu et al. (2023) conducted a study on the improvement of BHT efficiency through the incorporation of orthogonal microchannel structures with T-shaped heads. The findings indicated that the use of orthogonal channels led to a significant enhancement in HTC and CHF. Specifically, at lower heat flux levels, the elongation of the channels resulted in increased surface area, thereby promoting convective heat transfer. On the other hand, at higher heat flux levels, the T-shaped micro channels facilitated liquid replenishment. Nevertheless, it was observed that beyond a certain channel length, the growth of bubbles could lead to channel blockage, consequently hindering the replenishment of liquid.

Chen et al. (2020) performed a study on the BHT properties of interconnected micro channels with re-entrant cavities (IMRCs) and compared them with smooth copper plates. The IMRCs were created using the orthogonal ploughing-extrusion (P/E) technique followed by WEDM on copper substrates. The IMRCs exhibit a large surface area as a result of the fabrication process through orthogonal P/E method, which preserves the residual metal that is converted into micro-fins instead of cutting chips. As a result, heat dissipation can occur quickly due to the increased heat transfer surface area. Moreover, the interconnected pores and re-entrant cavities can boost the nucleation site density, thereby improving nucleate boiling and enhancing heat transfer efficiency.

Zhang et al. (2022) investigated the BHT characteristics of radial micro-pillar surfaces under various liquid sub-cooling temperatures using FC-72 as the working fluid. The findings indicated that these surfaces could effectively enhance the HTC and CHF. Micro-pillar surfaces offer a greater number of nucleation sites with varying sizes compared to smooth surfaces, enabling them to initiate boiling at lower heat flux levels. This facilitates timely heat dissipation and helps maintain a relatively stable wall temperature. On the other hand, unlike smooth surfaces with nearly zero wicking velocity, micro-pillar surfaces exhibit strong capillary wicking. The robust capillary force between the micro-pillars aids in liquid replenishment for evaporation, resulting in reduced wall superheat at high heat flux levels and achieving higher CHF values.

Jo et al. (2011) conducted a study on the influence of surface wettability on BHT. Wettability refers to the ability of a liquid droplet to spread and create a contact angle (CA) with a solid surface. The wettability of a surface plays a crucial role in determining the heat transfer efficiency of a boiling surface. Hydrophilic surfaces are characterized by a strong attraction to water, resulting in a CA of less than 90° , which causes water to spread out. Superhydrophilic surfaces exhibit an even stronger affinity for water, allowing it to spread out almost completely, leading to a CA close to 0° . The research findings indicate that hydrophilic and superhydrophilic surfaces facilitate the rewetting of potential dry spots beneath the growing vapor bubble, thereby delaying the onset of CHF. Conversely, hydrophobic surfaces repel water, leading to the formation of droplets with a high CA, typically exceeding 90° . Superhydrophobic surfaces demonstrate extreme water repellence, causing water droplets to bead up and roll off easily, with a CA exceeding 150° . It was observed that hydrophobic surfaces initiate boiling at lower wall superheat temperatures and exhibit a higher active NSD, making them suitable for boiling at lower heat fluxes. However, even at moderate heat fluxes, these surfaces tend to prematurely transition to the inefficient film boiling regime, resulting in elevated surface temperatures. Superhydrophobic surfaces, despite having lower bubble incipience temperatures, quickly transition to film boiling immediately after nucleation, making them unsuitable for boiling applications.

Allred et al. (2018) presented a new perspective on superhydrophobic surfaces in boiling applications. Typically, superhydrophobic surfaces are in a Cassie-Baxter state (with a roll-off angle $< 10^\circ$), characterized by the presence of trapped air in surface irregularities or roughness, which facilitates the creation of an insulating vapor layer, leading to a notable reduction in heat transfer efficiency. The research conducted in this study illustrated that when boiling occurs on superhydrophobic surfaces, transitioning from a Cassie-Baxter state to a Wenzel state (with no roll-off angle), where the surface texture is infiltrated with liquid, results in a considerable decrease in surface superheat, along with sustained nucleate boiling. This phenomenon is attributed to the presence of a pinned three-phase contact line during vapor bubble growth, which hinders the formation of a vapor film on the surface and consequently delays the CHF. Furthermore, Može et al. (2022) conducted a similar study and observed that pool

boiling on a superhydrophobic surface in the Wenzel state leads to a significant reduction in bubble departure diameter and an increase in bubble departure frequency. These effects contribute to a higher HTC.

Betz et al. (2010) investigated the impact of surfaces with mixed hydrophilic and hydrophobic areas, known as biphilic surfaces, on BHT performance. The researchers illustrated that flat surfaces that combine hydrophilic and hydrophobic patterns lead to a significant enhancement in pool boiling performance. The CHF and HTC of these improved surfaces were determined to be up to 65% and 100% higher, respectively, when compared to a surface that is solely hydrophilic. Various networks that incorporate both hydrophilic and hydrophobic regions were analysed, with notable increases in CHF typically observed for hydrophilic networks containing hydrophobic islands as opposed to hydrophobic networks containing hydrophilic islands. Hydrophilic networks with hydrophobic islands effectively prevented the formation of a vapor layer that acts as an insulator, promoted nucleation, enhanced HTC, and raised the CHF by preventing dry out. In their subsequent research (Betz et al. 2013), the authors further explored the biphilic concept by introducing superbiphilic surfaces that juxtapose superhydrophobic and superhydrophilic areas. It was noted that HTC measured on superbiphilic surfaces were up to three times higher than those on biphilic surfaces. The enhanced heat transfer on superbiphilic surfaces was attributed to the diverse range of transport phenomena induced on such surfaces, including the movement of wetting lines and capillary effects.

Choi et al. (2016) reported the fabrication of an innovative bi-functional boiling surface that can control bubble nucleation, growth, and departure dynamics. The process of creating a bi-functional surface involves the printing of hydrophobic polymer dot arrays, followed by the deposition of hydrophilic ZnO nanostructures using micro reactor-assisted nanomaterial deposition (MAND) technique. The contrast in wettability between the hydrophobic polymer dot arrays and the aqueous ZnO solution enables the fabrication of bi-functional surfaces with distinct wettability regions. Various configurations of bi-functional surfaces were produced by altering the sizes and pitch values of the polymer dots. The craters in the polymer dots act as vapor traps to initiate nucleation, while the ZnO nanostructures enhance capillary action and

replenish dry hydrophobic spots at higher heat fluxes. The unique design of this bifunctional surface ensures that the vapor-generation site is positioned lower than the hydrophilic structures, enhancing wicking compared to configurations with a hydrophobic site at the same level as the wicking structures. This configuration promotes an increase in the volume of replenished fluid, leading to improved boundary layer mixing and more vigorous bubble motion, resulting in quicker bubble departure. Consequently, boiling experiments demonstrated a significant enhancement in BHT, with up to three times the heat flux at the same wall superheat for the tested bifunctional surfaces compared to a plain surface. Additionally, the authors observed that as the bubble size increases with the dot size, bubble nucleation is delayed and necessitates higher heat flux. This phenomenon can be attributed to the larger hydrophobic areas creating a larger liquid-gas interface, thus requiring a higher superheat to initiate nucleation.

Lim and Bang (2020) investigated the BHT on biphilic surfaces, focusing on relationship between the size and pitch of hydrophobic spots. Pool boiling experiments were conducted with deionized water at atmospheric pressure, using different biphilic surfaces by varying the pitch of hydrophobic spots keeping the spot diameter constant. The results showed that the enhancements in CHF and HTC, which are indicators of boiling performance, varied for each biphilic surface. This suggests that the influence of the hydrophobic pattern on boiling phenomena depends on the pattern geometry. Among the biphilic surfaces investigated, the surface with a higher number of hydrophobic spots, resulting from a reduced spacing, exhibited superior heat transfer performance, exhibiting a 14.5% increase in CHF and a 34.1% increase in HTC compared to those on a bare substrate. The enhancement in BHT was attributed to the presence of additional active nucleation sites created by the smaller spacing between hydrophobic spots.

Motezakker et al. (2019) performed a parametric investigation to determine the optimal ratio between the hydrophobic and hydrophilic regions on a biphilic surface. The aim was to maximize the HTC and CHF. Various biphilic surfaces were examined by altering the size of circular hydrophobic spots while maintaining a constant pitch, and pool boiling experiments were carried out at atmospheric pressure using deionized

water. High-speed visualization of the boiling process revealed that the hydrophobic spots promoted nucleation, while the hydrophilic areas surrounding them facilitated the replenishment of liquid to dry spots, thus delaying the onset of CHF. The experimental findings revealed that both HTC and CHF were improved as the area ratio increased up to 38.46%. However, biphilic surfaces with an area ratio exceeding 38.46% exhibited a decline in CHF and HTC enhancement. This decline was attributed to the interaction between adjacent bubbles, which leads to the formation of a vapor blanket at lower wall superheat temperatures.

Može et al. (2020) investigated the optimal surface pattern for enhanced BHT using aluminum superbiphilic surfaces. To create these surfaces, a combination of chemical vapor deposition of fluorinated silane and nanosecond laser texturing was employed, resulting in the formation of superbiphilic surfaces with regions of both low and high wettability. The primary objective of the research was to maximize the CHF and HTC on these superbiphilic surfaces by optimizing the triangular lattice pattern of superhydrophobic circular spots, which varied in diameter and pitch values. The pool BHT performance of the superbiphilic surfaces was evaluated using saturated water at atmospheric pressure. The experimental findings revealed that in order to achieve optimal enhancement, the pitch value of the superhydrophobic spots should be approximately matched with the bubble departure diameter. This optimal pitch value would facilitate a high density of potentially active nucleation sites while still allowing for the growth of the thermal boundary layer, thereby facilitating the activation of neighbouring spots. Interestingly, the size of the superhydrophobic spots was found to have minimal impact on the boiling performance when the optimal spot pitch was employed.

Pontes et al. (2020) examined the impact of biphilic pattern geometry on BHT performance. The researchers utilized synchronized high-speed video and time-resolved thermography to analyse various biphilic surfaces. By systematically altering geometric parameters such as the size and position of superhydrophobic regions, the study found that smaller superhydrophobic regions resulted in more frequent bubble formation and detachment. The evaporated mass, a measure of latent heat removal from the heated surface, was observed to increase as the size of hydrophobic regions

decreased. Additionally, the synchronized high-speed video and thermal images demonstrated that biphilic patterns promoting moderate coalescence between detaching bubbles induced a convective flow of liquid between superhydrophobic areas. This flow led to a visible decrease in surface temperature and a higher evaporated mass flux, indicating a larger heat flux removed by latent heat for biphilic patterns with a moderate distance between superhydrophobic regions. However, the researchers raised concerns regarding the durability of superhydrophobic spots and their effectiveness with highly wetting liquids like FC 72 and PF 5060.

Rahman et al. (2015), introduced the novel concept of bi-conductive surfaces to overcome the challenges associated with traditional strategies for enhancing BHT. These bi-conductive surfaces are created by embedding an array of non-conductive lines into a highly conductive metal substrate, resulting in spatial variations in surface temperature during boiling. The researchers analysed various bi-conductive surfaces by adjusting the pitch between consecutive epoxy regions. All of these surfaces demonstrated an increase in heat transfer rate and a delay in the boiling crisis by manipulating bubble dynamics during boiling. Interestingly, when the pitch value approached the departure diameter of the bubble, a resonance-like effect was observed, leading to significant improvements in both HTC and CHF. In subsequent studies (Rahman and McCarthy 2017), the authors further modified the bi-conductive surfaces by incorporating nanostructured coatings and patterns of Polytetrafluoroethylene (PTFE) on the optimized bi-conductive surface. This modified surface was referred to as a bi-conductive biphilic surface. These bi-conductive biphilic surfaces exhibited their impact on all stages of the ebullition cycle. The presence of PTFE patterns reduced the wall temperature required for bubble formation, while the nanostructured coatings facilitated lateral wickability across the heating surface during boiling, resulting in delayed dry-out and increased CHF. Additionally, the bi-conductive nature of the surface altered the spatial distribution of temperature and created separate pathways for incoming liquid and outgoing bubbles. Consequently, the bi-conductive biphilic surface, which combines various enhancement techniques, demonstrated remarkable increases in CHF and HTC, exceeding a factor of 2.5X and 10X, respectively, compared to bare copper surfaces.

Najafpour et al. (2020) carried out BHT experiments on nanoporous surfaces that were embedded with low-conductive epoxy resin in circular cavities. The diameter of the cavities was kept constant at 2 mm, while the spacing between consecutive epoxy disks varied from 2.5 mm to 5 mm. With a decrease in the spacing between consecutive epoxy disks, there was an increase in the number of epoxy disks on the surface, leading to improvements in HTC and CHF. However, once the spacing between consecutive epoxy disks decreased beyond a certain threshold, resulting in more than 51% of the surface area being covered by epoxy disks, a significant drop in CHF was observed. The enhancements in HTC and CHF of modified surfaces were attributed to the presence of a superhydrophilic nanoporous oxide layer, which facilitated the rewetting and lateral spreading of the liquid. Furthermore, the epoxy disks played a vital role in augmenting the heat transfer by maintaining a wet surface and preventing bubble coalescence during boiling. Additionally, the presence of these epoxy disks induced a two-dimensional micro flow towards dry regions, owing to the combined effects of nanoporous surface absorption. This phenomenon notably delayed the formation of a vapor blanket, thereby further enhancing overall heat transfer efficiency.

Jaikumar et al. (2018) introduced the concept of Nucleating Region with Feeder Channel (NRFC) to enhance BHT. The NRFC design included bubble nucleating regions spaced apart to prevent lateral bubble coalescence and promote convective liquid jets in the areas between adjacent nucleating regions. Feeder channels were integrated into the non-nucleating regions to guide liquid flow towards the nucleating regions. The study investigated the relationship between the length of the feeder channel and the diameter of the departing bubble to optimize heat transfer. Results showed a significant increase in HTC and CHF, when the feeder channel length matched the bubble departure diameter. However, deviations from this optimal length led to a decrease in performance. The feeder channel played a dual role by ensuring continuous water supply to the nucleating regions and inducing a jet impingement effect that enhanced HTC during bubble departure. A too short feeder channel length hindered heat transfer due to bubble interference, while an excessively long length reduced the impingement effect. Therefore, the study recommended using the shortest feasible

feeder channel length slightly larger than the bubble departure diameter to avoid bubble disruption and maximize heat transfer efficiency.

Elkholy and Kempers (2020) conducted a series of experiments on copper surfaces to investigate the effects of 3D-printed porous polymer fixtures on pool boiling. These fixtures were specifically designed to divide the copper surface into smaller units, allowing for better control of bubble dynamics during the boiling process. The fixtures were created using fused filament fabrication (FFF) technique, with variations in unit cell size and height. The 3D printing process resulted in the formation of internal voids and pores within the fixture walls, which facilitated capillary action and helped replenish the liquid to nucleation sites. Interestingly, the researchers found that smaller unit cells led to a reduction in bubble departure diameter and an increase in bubble departure frequency, ultimately improving the HTC at moderate heat flux levels. However, at high heat fluxes, the presence of the small unit cell fixtures became detrimental to heat transfer efficiency. This was attributed to the fact that a relatively large portion of the boiling area was covered with a low-conductivity fixture material, limiting the overall heat transfer capability. Conversely, increasing the height of the fixtures was found to have a negative impact on HTC at both low and high heat fluxes when compared to fixtures with the smallest height. Taller fixtures led to longer bubble escape times, causing friction losses that dissipated stored energy. Moreover, at high heat flux levels, taller fixtures helped counteract the convection currents induced by bubble departure, thereby reducing heat transfer efficiency. Based on these findings, the authors emphasized the importance of optimizing the design parameters of 3D-printed fixtures to achieve optimal heat transfer performance in pool boiling applications.

Holguin et al. (2017) developed an easy to make, durable, cost-effective, and scalable binary surface (BiS) for BHT enhancement. The BiS was produced on a copper substrate through a three-step bulk micro-manufacturing process. These surfaces were composed of numerous micro-/nano-cavities filled with a non-boiling liquid, forming puddles around solid islands. The researchers postulated that the presence of this immiscible non-boiling liquid puddles would separate the solid islands on the binary surface, thus preventing lateral bubble coalescence, promoting early bubble

detachment, and facilitating surface rewetting. Pool boiling tests were conducted on the BiS using PF-5060, a dielectric liquid, as the boiling liquid and water as the non-boiling liquid. The experimental results demonstrated that the BiS was able to increase the CHF and HTC by 2.2 and 7.5 times, respectively, compared to those values on a plain copper surface. Furthermore, the maximum heat flux achieved on the BiS, which was 35.06 W/cm², surpassed any previous enhancements reported in the literature for the pool boiling of PF-5060 on enhanced surfaces up until that point.

Table2. 1 Summary of literature on boiling heat transfer enhancement

Authors	Type of surface	Remarks
Walunj and Sathyabhama (2018)	Open Micro channels	Geometry of micro-channels that contribute to the enhanced liquid supply improves the BHT
Saffari et al. (2020)	inclined meso channels	The trapped vapor under the inclined meso channels enhances the nucleation process contributing to improved BHT
Jiang et al. (2021)	cylindrical pillar array	Optimized distance between consecutive cylindrical pillars result in rewetting of the dry spots and early bubble departure
Jaswal et al. (2023)	rectangular and trapezoidal fins	The additional surface area provided by the fins increased the active NSD and there by BHT
Godinez et al. (2019)	Microporous coatings	Microporous coatings enhance the active NSD and reduce the bubble incipience temperature
Yu et al. (2023)	orthogonal microchannels with T-shaped heads	The additional surface area provided by the T shaped heads increase active NSD
Chen et al. (2020)	Interconnected micro channels with re-entrant cavities	Interconnected re-entrant cavities boost the active NSD and induces early departure of bubbles.

Zhang et al. (2022)	Radial micro pillars	Micro-pillar surfaces exhibit strong capillary wicking which aids in liquid replenishment to dry spots
Jo et al. (2011)	Hydrophilic and Hydrophobic surfaces	Hydrophilic nature of the surface improves liquid rewettability and enhances CHF whereas hydrophobic nature of the surface aids in early bubble incipience and improves HTC at low heat flux levels.
Allred et al. (2018)	Superhydrophobic surfaces in Wenzel state	Superhydrophobic surfaces in Wenzel state induces contact line pinning that results in lower bubble departure diameters and higher departure frequencies.
Betz et al. (2010)	Biphilic surface	The hydrophobic spots on a hydrophilic surface enhances HTC and CHF simultaneously by lowering the incipience temperature and offering liquid replenishment at high heat flux levels.
Choi et al. (2016)	Bi-functional surface	The polymer dots on bi-functional surface act as vapor traps to initiate nucleation, while the ZnO nanostructures replenish dry hydrophobic spots resulting in enhancement of CHF and HTC.
Lim and Bang (2020)	Biphilic surface	Smaller spacing between hydrophobic spots induce more active NSD and there by enhanced HTC.
Motezakker et al. (2019)	Biphilic surface	Both HTC and CHF increases simultaneously as the hydrophobic area on the biphilic surface increases
Može et al. (2020)	Superbiphilic surface	The size of the superhydrophobic spots have minimal impact on the boiling performance when the optimal spot pitch was employed.

Pontes et al. (2020)	Biphilic surface	BHT increased as the size of hydrophobic regions decreased.
Rahman and McCarthy (2017)	Bi-conductive biphilic surface	This surfaces influenced all stages of the ebullition cycle. PTFE patterns lowered the bubble incipience temperature, while nanostructured coatings enhanced wickability, and bi-conductive nature of the surface alter temperature distribution for efficient liquid and bubble pathways
Najafpour et al. (2020)	Bi-conductive superhydrophilic surface	As the spacing between consecutive epoxy disks decreases beyond a certain threshold, the coverage area of the epoxy disks exceeds 51%, leading to a significant drop in CHF
Jaikumar et al. (2018)	Surface with nucleating regions surrounded by feeder channels	The feeder channels on the surface play has two functions one is to provide continuous water supply to the nucleating regions and the second is to induce a jet impingement effect that enhance HTC during bubble departure
Elkholy and Kempers (2020)	Surface with 3D-printed porous polymer fixtures	The 3D fixtures divide the heater surface into smaller units, allowing for better control of bubble dynamics during the boiling process resulting in enhanced HTC and CHF.
Holguin et al. (2017)	Binary surface	The presence of immiscible non-boiling liquid puddles separate the solid islands on the binary surface, aiding in preventing lateral bubble coalescence, promoting early bubble detachment, and facilitating surface rewetting.

2.2 STUDIES ON BUBBLE DYNAMICS

Several studies have been carried out to investigate the bubble dynamics and mechanisms responsible for boiling enhancement. The details of such studies are discussed below and summarized in Table 2.2.

Mchale and Garimella (2010) carried out an investigation into pool boiling bubble dynamics on both polished and roughened aluminum surfaces. Through the use of high-speed visualization, authors were able to measure the D_d , f , active NSD, and bubble terminal velocity. The findings revealed that surface roughness and wall superheat have a significant impact on all of these parameters. Upon comparing the obtained results with existing model correlations in the literature, it was noted that, with the exception of heat flux prediction, all other parameters showed good agreement for both polished and rough surfaces. As a result, it was recommended that new bubble nucleation correlations be developed to incorporate the crucial aspects of surface topography, enabling mechanistic modelling to be applied across a wide range of boiling surfaces.

Moita et al. (2015) investigated the bubble interactive mechanisms during pool boiling on various surface topographies, including cavities, micro pillars, and fins. The study revealed that the lack of precise control over bubble dynamics can result in a significant reduction in the HTC, thereby negating the advantages gained from increasing the surface area.

Goel et al. (2017) conducted a study aimed at generating subcooled nucleate pool boiling data under a wide range of conditions not previously documented in existing literature. Using high-speed videography, the authors examined the characteristics of bubble dynamics, specifically focusing on D_d and f . The authors varied parameters such as heater surface roughness, geometry, and inclination, as well as sub-cooling and superheating temperatures. The results indicated that the D_d increased with wall superheat, heater size, and inclination angle, while liquid sub-cooling and surface roughness had a dampening effect on the D_d . Additionally, the departure frequency was found to increase with wall superheat and inclination angle, but decrease with an increase in heater size. The f also increased with the degree of sub-cooling, except when

very close to saturation, and remained unaffected by surface roughness beyond a certain superheat value.

Kumar et al. (2023) investigated the mode of interaction between adjacent vapor bubbles growing on a hydrophilic surface under sub-cooled nucleate boiling conditions. High-speed videography revealed that unlike the symmetric growth of the microlayer underneath the isolated bubbles, microlayers underneath mutually interacting vapor bubbles are asymmetric and tend to deplete relatively faster, impacting wall heat transfer rates. Further, the lift-off time, movement and depletion of the microlayer beneath the first bubble depends on the second bubble, irrespective of the spacing between the interacting bubbles. In addition to bubble spacing, factors such as heat flux and degree of sub-cooling strongly impact the bubble interaction. Precisely, the bubble size increases with heat flux but decreases with the degree of sub-cooling.

Chen et al. (2018) conducted a comprehensive analysis of bubble dynamics on silicon substrates that were locally heated, both with and without cavities, using synchronized high-speed infrared thermography and high-speed video. This setup enabled efficient measurement of wall temperatures and recording of bubble dynamics. The non-uniform temperature distribution induced by localized heating caused bubbles to slide from the nucleation site to the heater boundary. This sliding phenomenon provides a deeper understanding of microlayer evaporation beneath the bubble, heat conduction to the bubble and energy accumulation within the bubble. Visualization results revealed that microlayer evaporation and energy accumulation occurred more rapidly on surfaces with cavities than without, attributed to the reduced energy barrier for nucleation on surfaces with cavities.

Pontes et al. (2020b) conducted a study on the dynamics of a single bubble nucleation from generation to detachment on biphilic surfaces with the goal of developing an optimum biphilic pattern to enhance BHT at lower wall superheat. The High-speed visualization allowed identify various stages of bubble growth on all the biphilic surfaces examined, irrespective of the dimensions of the hydrophilic areas. It was observed that the D_d is affected by the size of the hydrophobic regions, due to the surface tension forces acting at the interfaces between the hydrophilic and hydrophobic

regions. Further, larger temperature gradients at the hydrophilic/hydrophobic boundaries induce higher evaporated mass fluxes.

Hong et al. (2024) conducted numerical analysis of bubble dynamics on both plain and honeycomb-structured porous surfaces. Their findings revealed that, in comparison to plain surfaces, the dry patch beneath a growing bubble on a honeycomb-structured porous surface is confined within the pore. This confinement restricts the three-phase contact line, leading to decreased D_d and increased f .

Wang et al. (2023) conducted research on the dynamic behaviour of bubbles during pool boiling under sub-atmospheric pressure conditions ranging from 30 to 120 kPa. Their findings indicate that as the boiling pressure decreases within the sub-atmospheric range, D_d increases while the f decreases. The decrease in pressure results in a smaller density difference between the liquid and vapor phases, leading to reduced buoyancy that enables bubbles to grow to a larger size before detaching. Additionally, the decrease in pressure suppresses the presence of active NSD, thereby lowering the frequency of bubble detachment.

Cai et al. (2023) examined the bubble dynamics of pool boiling on surfaces with different wettabilities, including normal, superhydrophilic, and superhydrophobic surfaces oriented vertically in a pool of liquid. The findings revealed that on neutral and superhydrophilic surfaces, the bubbles incept, grow, detach from the nucleation sites, and ascend into the liquid pool. However, on superhydrophobic surfaces, the bubbles grow and tend to adhere to the surface, sliding instead of detaching and rising. Additionally, it was observed that the size and frequency of bubble detachment on superhydrophilic surfaces are smaller and greater, respectively, when compared to normal surfaces. Consequently, superhydrophilic surfaces demonstrate superior heat transfer capabilities in vertical configurations.

Chang and Ferng (2019) conducted an experimental investigation with the aim of validating the CFD two-phase and BHT models by determining the boiling curve and bubble dynamic characteristics of saturated pool boiling. The accuracy of BHT models in thermal industries depends heavily on correlating the bubble dynamic parameters appropriately. The measured bubble dynamics in this study include the D_d, f , and active

NSD. Analysis of the experimental data revealed that bubble coalescence and active NSD increased with an increase in wall superheat, while the departure frequency decreased with an increase in D_d . To establish the relationship between the obtained bubble dynamics and wall superheat, a least-square regression method was employed. By incorporating the regressed bubble dynamic equations into the CFD wall heat-flux partitioning model, a predicted boiling curve was generated, which exhibited a reasonable agreement with the experimental boiling curve obtained in this study.

Extensive research has been conducted in the literature on the dynamics of bubble departure in pool boiling, exploring a wide range of variables such as pressure variations, different levels of sub-cooling up to the saturated temperature, changes in the orientation of the heater surface from horizontal to vertical, and the use of both normal and enhanced surfaces. By investigating the dynamics of bubble departure from the heater surface under different conditions, a deeper understanding of the mechanisms involved in improving heat transfer from the surface can be achieved. Moreover, establishing correlations between the bubble dynamic parameters on enhanced surfaces with wall superheat and heat flux aids in the optimization of boiling heat transfer models by incorporating additional parameters specific to enhanced surfaces.

Table2. 2 Summary of literature on bubble dynamics

Authors	Aim of the study	Remarks
Mchale and Garimella (2010)	bubble dynamics study on polished and roughened aluminum surfaces	Surface roughness and wall superheat have a significant impact on bubble dynamics
Moita et al. (2015)	Study of bubble interactive mechanisms during boiling	Lack of precise control over bubble dynamics can result in a significant reduction in the HTC
Goel et al. (2017)	Study of bubble dynamics at sub-cooled temperatures	Bubble departure frequency decreases with wall superheat whereas departure diameter and active NSD increases with wall superheat
Kumar et al. (2023)	mode of interaction between adjacent vapor bubbles on a hydrophilic surface	The bubble spacing, heat flux and degree of sub-cooling strongly impact the bubble interaction.

Chen et al. (2018)	Bubble dynamics on locally heated silicon substrates with and without cavities	The reduced energy barrier on surface with cavities enable microlayer evaporation and energy accumulation more rapidly to enhance HTC
Pontes et al. (2020b)	study on the dynamics of a single bubble nucleation from generation to detachment on biphilic surfaces	Size of the hydrophobic regions effect the bubble departure diameter due to the surface tension forces at the interface between hydrophilic and hydrophobic regions.
Hong et al. (2024)	Bubble dynamics on honeycomb-structured porous surfaces	The dry patch beneath the bubble on a honeycomb-structured porous surface is confined, reducing departure diameter and increasing departure frequency by inducing three-phase contact line pinning.
Wang et al. (2023)	Bubble dynamics during pool boiling under sub-atmospheric pressure conditions	As the pressure reduces the departure diameter increases and frequency reduces. Further the low pressures also suppress the active NSD.
Cai et al. (2023)	bubble dynamics on surfaces with different wettabilities	On neutral and superhydrophilic surfaces, bubbles grow and detach, while on superhydrophobic surfaces, bubbles grow but tend to adhere to the surface.

2.3 STUDIES ON MITIGATION OF INORGANIC FOULING

Inorganic fouling refers to the accumulation solid inorganic compounds such as carbonates and sulfates of calcium and magnesium on heat-exchanging surfaces, which poses a significant challenge in thermal desalination systems such. Desalination systems aim to extract fresh water from brackish feeds, which leads to the accumulation of inorganic compounds that can become supersaturated and subsequently precipitate or deposit onto surfaces. Consequently, precipitants adhere to the surface, resulting in

a decrease in heat exchange efficiency. Various strategies have been studied in the literature to mitigate inorganic scaling. This section provides a brief overview of notable research efforts focused on mitigation of inorganic fouling and summarized in Table 2.3.

Ayoub et al. (2019) investigated various pre-treatment methods for brackish feeds prior to their entry into desalination systems. The research findings indicate that the selection of a suitable pre-treatment approach depends on the quality of the original brackish water source. The primary objective of pre-treatment is to effectively remove a significant portion of the scaling/fouling substances present in the raw brackish feeds. Initially, these feeds undergo filtration to eliminate suspended solids and chlorination for disinfection. Subsequently, depending on the quality of the raw brackish feeds, conventional pre-treatment techniques involving the use of different chemicals at varying pH and temperature, as well as advanced membrane-based strategies like ion-exchange water softening, as proposed by Venkatesan and Wankat (2011), are employed to eliminate fouling and scaling materials from the raw brackish feeds.

Shen et al. (2012) synthesized a threshold agent by combining hydrolyzed polymaleic anhydride (HPMA), 1-hydroxyethane-1,1-diphosphonic acid (HEDP), and polyacrylic acid (PAA) in a mass ratio (dry weight) of 10:80:10. The aim was to tackle calcium carbonate scaling in desalination plants. The researchers found that the synthesized threshold agent formed complexes with free Ca^{2+} ions, reducing the degree of supersaturation. Consequently, this reduction slowed down calcium carbonate precipitation. Moreover, the threshold agent adsorbed onto the active sites of calcium carbonate nuclei on the substrate, disrupting the growth of calcium carbonate crystals.

Al-Mutairi et al. (2009) conducted a study on the impact of antiscalants, including hexametaphosphate (SHMP), Belgard EV2030, and ethylene-diamine-tetra acetic acid (EDTA), on the formation of calcium sulfate deposits on heat exchange surfaces within desalination facilities. The prevention of scaling is accomplished through the absorption of antiscalants at the crystal growth sites of sub-microscopic crystals that form in the supersaturated solution. This process disrupts crystal growth and modifies the morphology of the crystals. Additionally, the researchers noted that the

effectiveness of antiscalants diminishes as the concentration of calcium sulfate in the feed water increases.

Popov et al. (2022) investigated calcium carbonate scaling during desalination using two novel fluorescent-tagged scale inhibitors: 1,8-naphthalimide-tagged poly acrylate (PAA-F1) and 1-hydroxy-7-(6-methoxy-1,3-dioxo-1H-benzo[de]isoquinolin-2(3H)-yl) heptane-1,1-diylbis (phosphonic acid) (HEDP-F). Although, both fluorescent-tagged antiscalants reduced calcite crystal size compared to the blank experiments, HEDP-F was slightly more effective against calcite scaling, while PAA-F1 showed greater influence on calcite morphology. The enhanced calcium carbonate scaling inhibition of fluorescent-tagged antiscalants was attributed to the interplay between background calcium concentration and solubility of sparingly soluble calcium salts.

Cheong et al. (2013) examined how the nature of the substrate influences the formation, growth, and adhesion of calcium carbonate scaling. The researchers found that coated metal substrates exhibited lower adhesion to calcium carbonate scaling compared to bare metal substrates. Additionally, the study revealed that the adhesion capabilities of textured polymers decreased as the surface energy increased, unlike coated metal substrates.

Izadi et al. (2010) conducted an experimental investigation to examine the impact of surface roughness on fouling behaviour. The findings indicated that the density of the foulant layer deposited on rough surfaces was greater than that on smooth surfaces over time. Upon microscopic analysis of the fouled surfaces, it was discovered that the fouled layer on the rough surface displayed a mixture of aragonite and calcite polymorphs, whereas the smooth surface exhibited only dendrite porous aragonite crystals, resulting in a less dense foulant layer.

Chevalier (2014) highlighted the importance of wettability and surface structure in influencing the rate and mechanism of surface-induced inorganic fouling. The study observed a general decrease in crystal density as surface wettability increased on substrates that did not promote a specific crystal orientation. Conversely, an increase in crystal density was observed with increasing surface wettability on substrates that promoted highly selective crystal orientation.

Tzachristas et al. (2022) examined the fouling behaviour of calcium carbonate on packed beds with hydrophobic and hydrophilic wetting characteristics. The researchers observed a distinct delay in crystal growth and the presence of less stable polymorphs on the hydrophobic packed beds. Conversely, on the hydrophilic beds, only the most stable polymorph, namely calcite, was deposited. This was attributed to the chemical affinity of the working fluid with the hydrophilic surface, which facilitated its transport throughout the entire cross section of the bed and ultimately led to the formation of stable calcite.

Subramanyam et al. (2014) examined the efficacy of slippery liquid infused porous surfaces (SLIPS) in reducing gypsum scaling. SLIPS are obtained by infiltrating liquid lubricant into the micro textured substrate. The researchers found that the presence of the liquid lubricant induced an activation barrier that hindered the deposition of salt. Consequently, the rate at which salt accumulated on the lubricant-infused surface was lower compared to the bare substrate. Additionally, the study revealed a correlation between the surface tension of the impregnated liquid lubricant and the heightening of the activation barrier.

Charpentier et al. (2015) conducted a study to assess the durability of a lubricant-infused surface by examining the contact angle hysteresis after 12 hours and 24 hours of exposure to a simulated seawater environment. The increase in contact angle hysteresis indicates the gradual replacement of the infused lubricant by the simulated seawater near the surface. The research findings revealed that the contact angle hysteresis on the substrate infused with Fluorinert FC-70 exhibited an increase in contact angle hysteresis with longer immersion time. Conversely, in the case of the substrate infused with BMIm (1-Butyl-3-methylimidazolium bisimide), the contact angle hysteresis remained unchanged. This was attributed to the relatively lower surface tension of BMIm liquid (34 mN/m in contrast to 18 mN/m for Fluorinert FC-70), which contributes to enhanced stability and consequently, a decrease in contact angle hysteresis.

Masoudi et al. (2017) conducted a study to evaluate the effectiveness of inorganic fouling mitigation on plain surfaces compared to surfaces infused with liquid lubricant in an artificial seawater environment. The study findings indicated that, unlike plain

surfaces, liquid-infused surfaces create both a liquid-liquid interface and a solid-liquid interface when submerged in artificial seawater. This smooth, defect-free liquid-liquid interface reduces the interactive forces between deposited foulants and the substrate, thereby decreasing the strength of scale adhesion.

Mousavi and Pitchumani (2022) conducted dynamic scaling tests to analyze calcium sulfate scaling patterns on bare surfaces, as well as on hydrophilic, hydrophobic, and liquid-infused surfaces. A general trend of decrease in the rate of mass gained due to scale buildup was observed on bare, hydrophilic, and hydrophobic surfaces as the Reynolds number increased. This reduction is attributed to the hindrance of stable scale buildup caused by higher shear forces at elevated Reynolds numbers. In contrast, on liquid-infused surfaces, an increase in scaling mass rate was observed with increase in Reynolds number, attributed to the exposing of underlying surface for fouling by partial displacement of infused liquid. Despite of this, liquid-infused surfaces demonstrate a better scaling mitigation abilities (60%-90%), when compared to bare surface in all testing conditions.

Table2. 3 Summary of literature on inorganic scaling mitigation strategies

Authors	Scope of the work	Remarks
Ayoub et al. (2019)	pre-treatment approaches	Selection of a suitable pre-treatment approach depends on the quality of the brackish water source.
Shen et al. (2012)	Synthesis of threshold agents to reduce calcium carbonate precipitation	Threshold agent adsorb onto the active sites of calcium carbonate nuclei to disrupt the growth of calcium carbonate crystals.
Al-Mutairi et al. (2009)	Impact of antiscalants on prevention of scaling	The prevention of scaling is accomplished by the absorption of antiscalants at the crystal growth sites of sub-microscopic crystals
Popov et al. (2022)	Mitigation of calcium carbonate scaling	Fluorescent-tagged antiscalants reduced calcite crystal size compared to the blank experiments

Cheong et al. (2013)	Influence of the substrate nature on scale formation	Coated metal substrates exhibited lower calcium carbonate scaling compared to bare metal substrates
Izadi et al. (2010)	Impact of surface roughness on fouling	Density of the foulant layer deposited on rough surfaces was greater than that on smooth surfaces
Chevalier (2014)	Effect of wettability on surface-induced inorganic fouling	An increase in crystal density was observed with increasing surface wettability
Tzachristas et al. (2022)	Calcium carbonate Fouling behaviour on packed beds with hydrophobic and hydrophilic nature.	A distinct delay in crystal growth and the presence of less stable polymorphs were found on the hydrophobic packed beds.
Subramanyam et al. (2014)	Efficacy of SLIPS in reducing gypsum scaling	Presence of the liquid lubricant on SLIPS induce an activation barrier that hindered the deposition of salt
Charpentier et al. (2015)	Durability of SLIPS	Lower the surface tension of infused lubricant increase the stability of SLIPS
Masoudi et al. (2017)	Antifouling effectiveness of liquid infused surfaces in artificial sea water environment.	Smooth and defect-free liquid-liquid interface on liquid-infused surface reduce the interactive forces between deposited foulants and the substrate.
Mousavi and Pitchumani (2022)	Calcium sulfate scaling patterns on hydrophilic, hydrophobic, and liquid-infused surfaces.	Decrease in the rate of mass gained due to scale buildup was observed on hydrophilic and hydrophobic surfaces as the Reynolds number increased.

2.4 STUDIES ON CORROSION INHIBITION

The strategies implemented for corrosion inhibition are briefly discussed below and summarized in table 2.4.

Trdan et al. (2011) conducted a study to explore the impact of laser pulse energy on the effectiveness of laser shock processing (LSP) as a surface enhancement technique for improving corrosion resistance. LSP involves immersing substrates in deionized water and directing high-power, short-pulse lasers onto the metal substrates through the transparent water. This process leads to the vaporization of a thin surface layer and the formation of plasma. The rapidly expanding plasma becomes trapped between the surface of the sample and the transparent water, acting as a confining layer. This confinement creates high pressure, which generates shock waves that induce plastic deformation and compressive residual stresses in the sample, ultimately enhancing its corrosion resistance. The experimental findings revealed that as the density of laser pulses increased, the intensity of corrosion attack decreased. This suggests that higher laser pulse density contributes to improved corrosion resistance. Furthermore, Shakier et al. (2016) demonstrated that the thickness of the confining layer, represented by the deionized water, also influences corrosion resistance. Specifically, the corrosion rate decreases as the confinement layer thickness increases up to 4 mm. However, beyond this threshold, the corrosion rate begins to rise. This increase was attributed to the thicker layer absorbing more laser energy, thereby reducing the energy available to the sample and compromising its corrosion resistance.

Rokkala et al. (2021) employed friction stir processing as a means to tailor the surface properties of Mg-1Zn-2Dy (wt.%) alloy, aiming to mitigate corrosion in temporary implant applications. This processing technique brought significant changes in the microstructural characteristics of the original as-cast alloy. The coarse α -Mg grains were completely replaced by extremely fine grains, while the secondary phases underwent fragmentation into fine particles that were uniformly dispersed. Consequently, the low angle grain boundaries observed in the as-cast alloy were transformed into high angle grain boundaries. Notably, electro-chemical corrosion tests conducted on the friction stir processed as-cast alloy demonstrated reduced corrosion rates, which was attributed to the development of an adhesive passive layer facilitated by the presence of high angle grain boundaries.

Xhanari and Finšgar (2019) reviewed the use of organic corrosion inhibitors for protecting aluminum and its alloys in alkaline and chloride-containing environments. They reported that the effectiveness of these inhibitors increases with higher inhibitor concentrations but decreases with rising temperatures. The corrosion mitigation by organic inhibitors was attributed to the presence of electron-donating groups in their chemical structure. These groups form insoluble complexes with metal cations, which then adsorb onto the aluminum surface, creating a barrier between the metal and corrosive environment.

Ansari et al. (2018) provided a comprehensive review of volatile corrosion inhibitors (VCIs) as effective inhibitors for both ferrous and non-ferrous metals and alloys. These VCIs offer corrosion protection through three mechanisms: anodic protection, cathodic protection, and a mixed type of protection. Anodic corrosion inhibition occurs when VCIs form a protective film, known as a passivation layer, on metal surfaces through adsorption. The high volatility of VCIs enables them to easily vaporize and condense on metallic surfaces, including hard-to-reach areas such as crevices, pores, and cracks, thereby providing comprehensive protection. On the other hand, cathodic corrosion inhibition involves the neutralization of corrosive agents present in the surrounding environment, such as H_2O , SO_2 , H_2S , and CO_2 . This neutralization process leads to a sudden increase in surface impedance, as cathodic corrosion inhibition reduces the diffusion rate of chemical species responsible for corrosion. Lastly, the mixed type of protection combines both anodic and cathodic protection by using VCIs.

Yuan et al. (2020) fabricated a super-hydrophobic aluminum surface using femtosecond laser ablation and subsequent heat treatment. This method resulted in the creation of a micro-textured surface capable of entrapping air within its microstructures. Consequently, the actual contact area between a sessile water droplet and the solid surface was minimized, leading to a significant improvement in hydrophobicity. The contact angle of a sessile water droplet on the textured surface was measured to be as high as 160° , with a roll-off angle of less than 5° , indicating that the surface was in the Cassie state. The authors noted that these super-hydrophobic surfaces exhibited excellent resistance to corrosion when submerged in an aqueous solution, attributed to the air pockets within the microstructures acting as a protective barrier between the

solid surface and the corrosive environment. Further, Wang et al. (2012) found that the super-hydrophobic surfaces in the Cassie state transitioned to the Wenzel state as the immersion depth in the corrosive medium increased, owing to the rising pressure. In the Wenzel state, the sessile water droplet infiltrates the microstructures. Despite maintaining high contact angles, surfaces in the Wenzel state lack roll-off angles, causing the droplet to adhere to the surface. The authors reported that while super-hydrophobic surfaces in the Wenzel state offer better corrosion protection than plain surfaces, those in the Cassie state provide superior corrosion protection to the underlying metal. Therefore, it was concluded that employing super-hydrophobic surfaces as a corrosion protection strategy in aqueous solutions is effective in systems with lower water pressure.

Cai et al. (2022) examined SLIPS as a potential alternative to the superhydrophobic surfaces to address the issues of poor durability in corrosion protection. Unlike superhydrophobic surfaces, the air entrapped in the micro porous structures was replaced by a liquid lubricant that is immiscible with the corrosive medium. The protective barrier created by the immiscible liquid lubricant provides prolonged protection to the metal underneath from corrosion attack. Tuo et al. (2017) and Yu et al. (2021) conducted experiments to compare the corrosion mitigation capabilities of SLIPS and superhydrophobic surfaces. They observed that similar to the superhydrophobic surfaces SLIPS exhibit very high contact angles and low roll-off angles. However, the presence of lubricant traces on the surface of the SLIPS induces super slippery property due to which the sliding velocity of the sessile droplet on the SLIPS is as high as 0.48 mm/sec. These characteristics of SLIPS make them more durable and effective in corrosion protection.

Zhu et al. (2023) fabricated SLIPS on 1060 pure aluminum by anodizing the aluminum samples in an H_2SO_4 electrolyte solution to form an aluminum anodic oxidation (AAO) layer with a capillary-like porous structure. Subsequently, the porous structure was filled with dimethyl silane lubricant oil. Examination of the corrosion patterns on the bare surfaces and SLIPS after exposure to salt spray corrosion and long-term immersion corrosion indicated that the bare substrates displayed lumpy corrosion products all over the surface, while the SLIPS exhibited minimal corrosion with few corrosion products

present, attributed to the synergistic effects of the AAO layer and the infused lubricant. Additionally, it was noted that the capillary action of the lubricant within the porous structure could replenish any defects on the surface, thereby maximizing the corrosion resistance capabilities of the SLIPS.

Table2. 4 Summary of literature on corrosion mitigation strategies

Authors	Scope of the work	Remarks
Trdan et al. (2011)	Effectiveness of LSP as a surface enhancement technique for improving corrosion resistance	As the density of laser pulses increased, the intensity of corrosion attack decreased
Rokkala et al. (2021)	Friction stir processing as a means to tailor the surface to mitigate corrosion in temporary implant applications.	LSP processing technique brought changes in the microstructural characteristics of the original as-cast alloy that aids in corrosion resistance.
Xhanari and Finšgar (2019)	Effectiveness of organic corrosion inhibitors for protecting aluminum in alkaline and chloride environments.	Effectiveness of inhibitors increases with higher inhibitor concentrations but decreases with rising temperatures.
Ansari et al. (2018)	volatile corrosion inhibitors (VCIs) for both ferrous and non-ferrous metals and alloys.	VCIs offer anodic protection, cathodic protection, and a mixed type of protection.
Yuan et al. (2020)	Super-hydrophobic aluminum surfaces for corrosion protection.	The air pockets within the microstructures of superhydrophobic surface act as a protective barrier between the solid surface and the corrosive environment.
Cai et al. (2022)	Effectiveness of SLIPS in corrosion protection	The immiscible liquid lubricant on SLIPS provide prolonged protection to the metal underneath from corrosion attack.
Zhu et al. (2023)	Effectiveness of liquid infused surface combined with AAO layer in corrosion mitigation	The synergistic effects of the AAO layer and the infused lubricant enhanced the corrosion protection.

2.5 CRITICAL LITERATURE REVIEW AND OBJECTIVES OF PRESENT WORK

Based on the literature, BiS can enhance BHT by promoting separate pathways for incoming rewetting liquid and outgoing vapor bubbles. In contrast, SLIPS are known for their effectiveness in reducing corrosion and inorganic scaling. The SLIPS create a protective lubricant layer that separates the corrosive medium from the metal substrate and minimizes the interaction between deposited foulants and the metal.

It is noteworthy that, like BiS, SLIPS are created by infusing a liquid into the micro/nano textures of the substrate. However, unlike BiS, SLIPS do not control the oversaturation of the infused liquid, resulting in a passive lubricant layer that significantly hinders heat exchange efficiency. Consequently, while SLIPS effectively mitigate corrosion and inorganic fouling, their application in the desalination industry is limited due to concerns about heat exchange efficiency (Zhao et al. 2018).

In contrast, BiS can enhance BHT while theoretically slowing down corrosive reactions and reducing precipitant adhesion due to the reduced effective surface area. However, there are no studies evaluating the corrosion and inorganic scaling mitigation capabilities of BiS.

Therefore, this study aims to develop a BiS on Al 6061 alloy to assess its effectiveness in mitigating corrosion and inorganic scaling in a simulated brackish water environment. Boiling tests at atmospheric pressure with deionized water, coupled with high-speed visualization, will be conducted on the BiS to understand the bubble departure dynamics behind the enhancement of BHT. The objectives of this research are as follows:

- To experimentally investigate the BHT performance of BiS in contrast to reference plain surface and a surface with high wetting properties.
- To study the bubble dynamics (D_d , f , and active NSD) on BiS to perceive the physical mechanism responsible for enhanced nucleate BHT.

- To investigate inorganic scale formation and its effect on condensate collection on a BiS when heated with simulated brackish water, comparing it to a reference plain surface and a highly wetting surface.
- To investigate the corrosion resistance provided by BiS compared to a reference plain surface and a highly wetting surface at various temperatures when exposed to simulated brackish water.

CHAPTER 3

ENHANCEMENT OF BOILING HEAT TRANSFER

3.1 TEST SURFACE PREPARATION AND CHARACTERIZATION

3.1.1 SURFACE PREPARATION

Figure 3.1 illustrates the flow sequence for fabricating BiS from a bare solid substrate. BiS surfaces were fabricated from commercial aluminum (Al 6061) alloy substrates using a three-step bulk micro-manufacturing approach developed by Cvijovic and Kota (2018). As received aluminum substrates possess a passive oxidation layer. Therefore, the substrates underwent an initial treatment involving sanding with silicon carbide sheets of varying grits, ranging from 80 to 1200. After the pre-treatment, the samples exhibited an average roughness of $0.44 \mu\text{m}$ (Ra). Subsequently, the substrates were subjected to sonication in acetone and deionized water. The resulting surface was a plain aluminum workpiece, referred to as the Plain Surface (PS), which was served as the reference sample.

Micro-grooves were made on the PS substrates in perpendicular directions using sandpaper with a grain size of $250 \mu\text{m}$. The substrates were sonicated again with acetone and deionized water to remove any free aluminum particles trapped in the micro-grooves. The substrates were then subjected to thermo-catalytic etching by immersing them in a chemical mixture of 70% nitric acid (HNO_3), methanol (CH_3OH), and deionized water in a 4:1:1 proportion at $100 \text{ }^\circ\text{C}$ for 90 minutes. After etching, the substrates were thoroughly cleaned with deionized water and dried at $100 \text{ }^\circ\text{C}$ for 10 minutes, resulting in an Ultra-Omniphilic Surface (UOS). The UOS consists of numerous micro and nano cavities along with the micro-grooves, forming a capillary network that enables extreme wetting and spreading of multiple liquids.

To create the BiS, liquid lubricant droplets were placed on the UOS, infiltrating the capillary network until saturation. Excess lubricant was wiped away with a paper towel

to reveal the solid islands, resulting in a BiS with lubricant pools surrounding the solid islands. The BiS underwent testing at various angles to verify that the lubricant was securely held by the capillary network of the UOS.

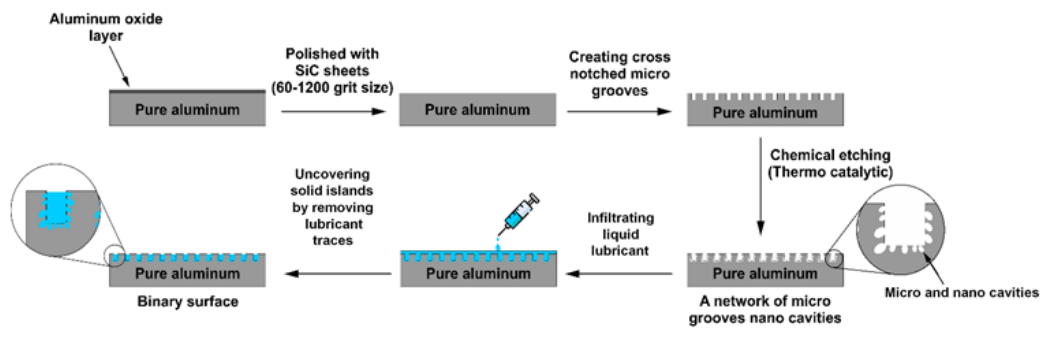


Figure 3.1 Flow sequence of the BiS fabrication.

Table 3.1 Thermo-physical properties of cutting board (mineral) oil at $T = 40\text{ }^{\circ}\text{C}$.

Property	Value
Boiling point ($^{\circ}\text{C}$)	260
Flash point ($^{\circ}\text{C}$)	150
Density (kg/m^3)	838.2
Viscosity ($\text{Pa}\cdot\text{s}$)	0.017
Thermal conductivity ($\text{W}/\text{m}\cdot\text{K}$)	0.145
Specific heat ($\text{kJ}/\text{kg}\cdot\text{K}$)	2.38
Solubility in water	Insoluble

It is important to note that the thermo-physical properties of the liquid lubricant are crucial for maintaining in-plane temperature variations on the BiS substrate. In this work, cutting board mineral oil was used as the liquid lubricant. The thermo-physical properties of the cutting board mineral oil are shown in Table 3.1. The cutting board mineral oil has a higher boiling point and lower thermal conductivity than that of

deionized water and saline water, which helps maintain in-plane temperature variations during BHT. Additionally, its lower viscosity facilitates easy infiltration into micro/nano cavities, and its moderate surface tension aids in maintaining a negative spreading coefficient. Although the density of the cutting board oil is lower than that of deionized water and saline water, the capillary force induced by the micro-nano network firmly holds the oil in place.

3.1.2 BIS CHARACTERIZATION

Since the BiS topography consists of two distinct phases—solid islands surrounded by liquid puddles—a confocal laser scanning microscope from Leica TCS SP II was used to analyse its features. First, a short-wavelength UV laser light was projected onto the liquid lubricant and the BiS substrates separately, and their fluorescence was measured and compared, as shown in Figure 3.2. The recorded fluorescence was entirely attributable to the liquid lubricant, making it difficult to detect the solid phase on the BiS.

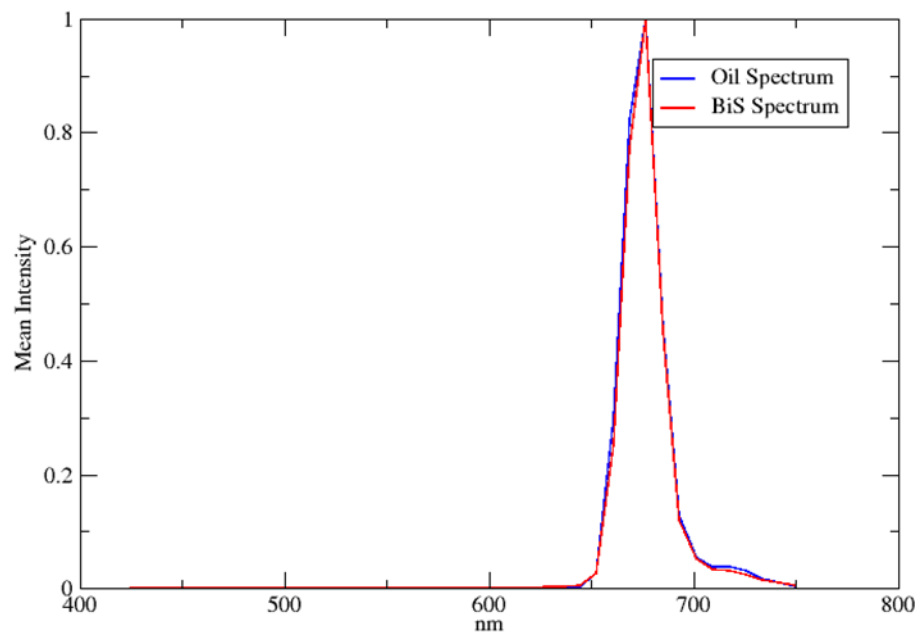


Figure 3.2 Fluorescent spectrum of oil and BiS.

Next, the refraction of the liquid lubricant and the BiS were measured separately. No refraction was observed from the oil, indicating that the refraction detected from the BiS could be attributed solely to the aluminum. Therefore, the image obtained by overlapping the refractive and fluorescence images of the BiS represents its actual state, as shown in Fig 3.3. In this composite image, the solid phase is represented by refraction (green) and the liquid phase by fluorescence (red).

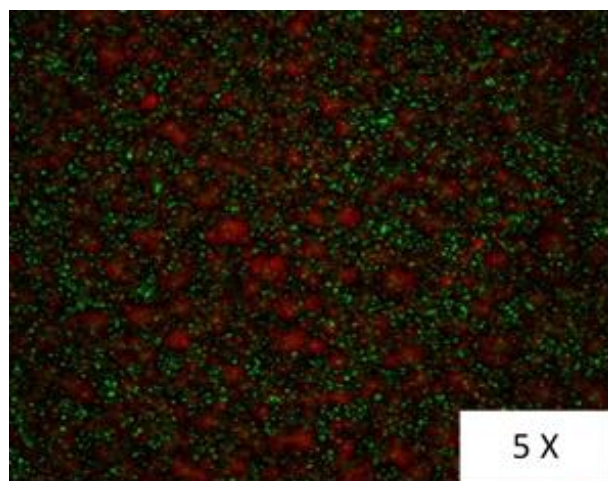


Figure 3.3 Overlay of BiS reflection and fluorescence spectrums.

Figure 3.4 (a) shows the topography of the BiS viewed through an optical microscope, with solid islands and liquid puddles labelled. Prior to the experiments, the contact angles of water droplets on the BiS were measured at various locations. The average contact angle observed on the BiS is 55° , as shown in Fig 3.4 (b). This indicates that the BiS does not exhibit any extreme patterns of wettability.

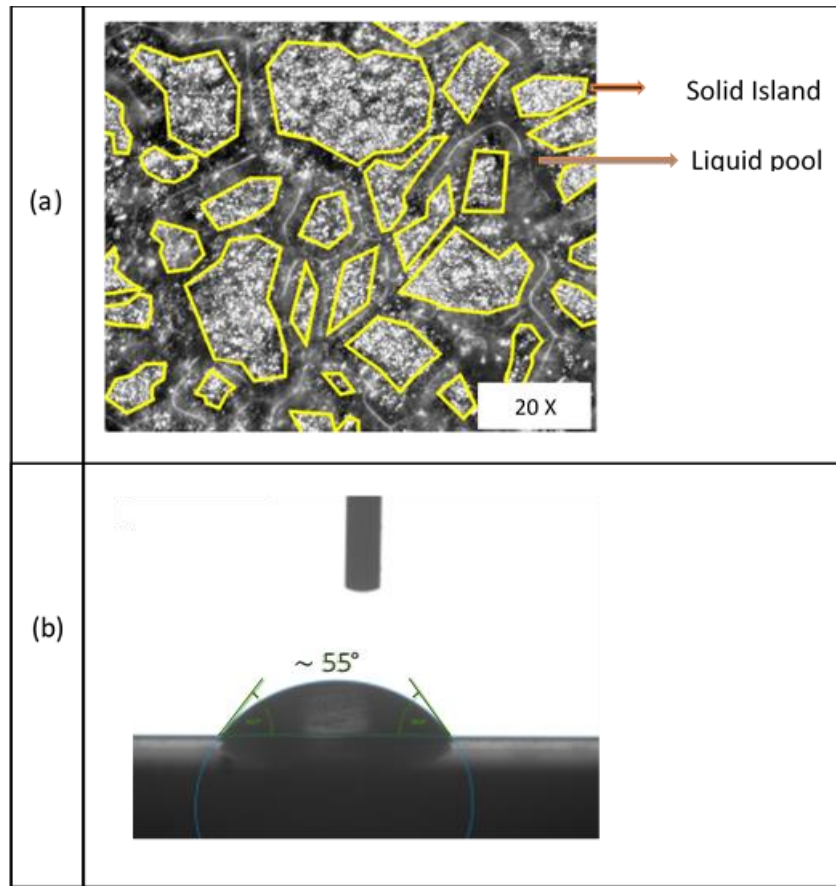


Figure 3.4 (a) BiS topography captured by optical microscope (b) Average contact angle on the BiS.

3.2 EXPERIMENTAL TEST SETUP AND PROCEDURE

3.2.1 BOILING TEST SETUP

The test setup as shown in Fig 3.5 was designed to conduct the boiling experiments on a horizontal test surface at atmospheric pressure and various instruments used in the experimentation are listed in Table 3.2. The test setup primarily consists of a rectangular boiling chamber made of stainless steel. The $250 \times 200 \times 400 \text{ mm}^3$ chamber holds the working fluid throughout the experiment at saturation temperature. One side of the

chamber has the provision to insert an auxiliary heater (of 500 W capacity) and temperature sensors into the liquid and the vapor zones. All the other three sides of the chamber consisted of transparent glass pieces to illuminate and capture the boiling phenomenon with high- speed image visualization. The top flange of the test chamber was fitted with a condenser and a pressure sensor. The bottom flange of the test section has a provision for test surface assembly and a drain valve. All sides of the chamber were covered with heat resistant material to minimize any possible heat loss from the chamber.

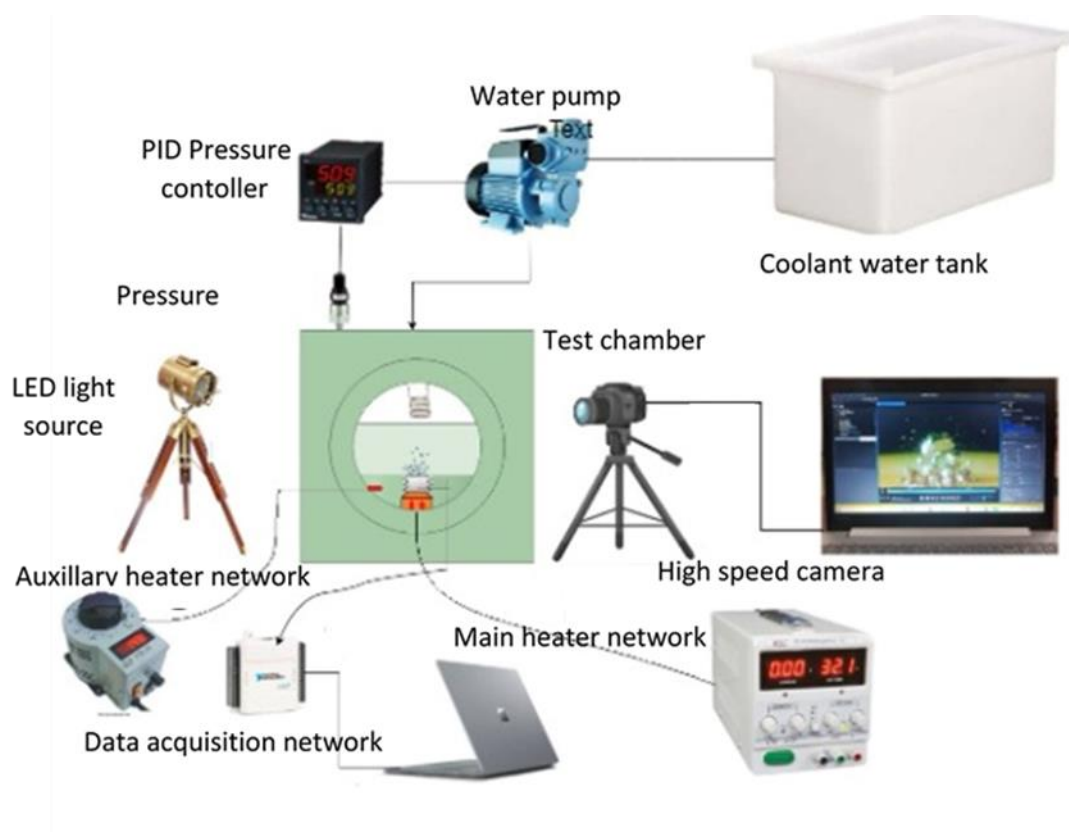


Figure 3.5 Boiling heat transfer experimental test setip.

The schematic of the test section assembly is shown in Fig 3.6. Four cartridge heaters of 6 mm diameter and 200 W capacity were press fitted into a copper heater block, which serves as the main heater. A circular Al 6061 workpiece of 20 mm diameter and 20 mm height was fastened to the main heater. The top surface of the workpiece is the

test surface and in contact with the working fluid. Three k-type thermocouples of 1 mm probe diameter were inserted into the workpiece at a distance of 2 mm, 6 mm, and 10 mm respectively from the test surface in the vertical direction. The workpiece along with heater block was fastened into a customized Teflon insulation block and any gap between the heater block and the Teflon block was filled with the glass wool insulation. The glass wool and Teflon block cover ensure axial (vertical) flow of heat from the heater rod to the test surface. The entire assembly was inserted into the boiling chamber from the bottom flange. A gasket maker and Teflon tape were used between the test surface assembly and the boiling chamber to make the assembly leak-proof.

Table 3.2 Instruments used in boiling heat transfer equipment

Instrument	Specifications
K-type thermocouple	Range: - 20 °C to 260 °C Probe diameter: 1 mm
Cartridge heaters (Main heater block)	Diameter: 6 mm Length: 50 mm Capacity: 200 W
Cartridge heater (Auxiliary)	Diameter: 16 mm Length: 150 mm Capacity: 500 W
Pressure transducer	Range: 1 bar to 27 bar Operating temperature: Up to 228 °C
Data acquisition system	Model: NI cDaq-9178 Number of channels: 16 Temperature accuracy: 0.01 °C

A control unit interfaced with boiling chamber monitors the pressure and temperature inside the chamber. The control unit houses the display units of the pressure sensor and temperature sensors that are inserted in liquid and vapor. Main and auxiliary heaters were also operated from the control unit with the help of variable voltage auto-transformer. A proportional integral derivative (PID) controller integrated with water

pump controls the pressure inside the boiling chamber by circulating water/coolant between the coolant storage tank and the condenser. The cold junction of k-type thermocouples from the workpiece was connected to the NI cDaq-9178 data acquisition system. A LabVIEW graphical programming environment was used to control the rate of obtaining temperature data from the data acquisition system. In the present work, the LabVIEW program collects the thermocouple data for every 500 ms and reports the average temperature recorded on each thermocouple for every 20 s. Graphs depicting the instantaneous variation of temperature with time and average temperature window at 40 W heat input are provided in appendix A.

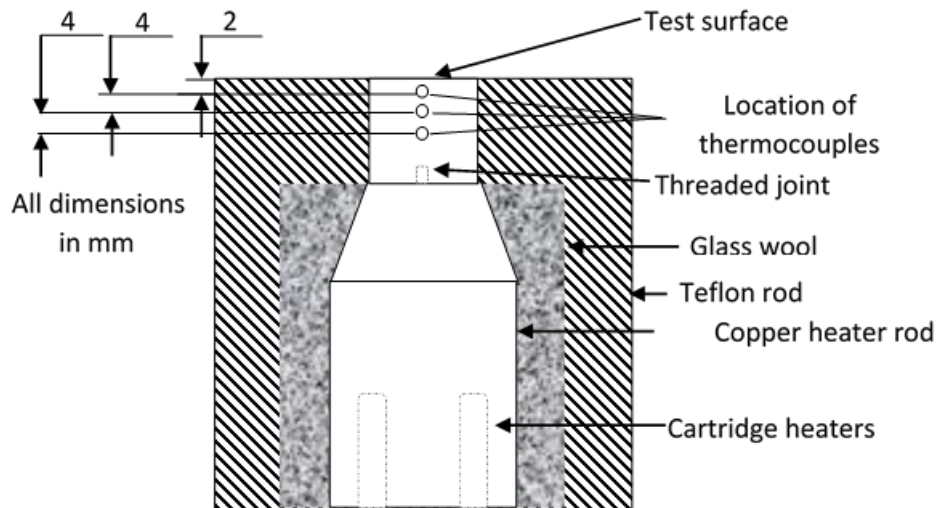


Figure 3.6 Test section.

3.2.2 EXPERIMENTAL PROCEDURE

A standard procedure was followed to conduct the experiments on all the surfaces to maintain consistency. As mentioned earlier, the test surface assembly was first inserted into the boiling chamber. The chamber was then filled with a measured quantity of deionized water, leaving a gap for vapor formation and condensation near the top flange. It was ensured that there were no leakages from the bottom flange. The auxiliary heater was turned on to heat the deionized water to the saturation temperature. The water was allowed to rigorously boil for one hour to remove the non-condensable gases.

Before initializing the actual tests, the light source was turned on along with the high-speed camera for adjusting the focus and aperture.

The main heater was turned on and the heat input was increased in steps until the CHF was reached. A sudden jump ($>20\text{--}30\text{ }^\circ\text{C}$) in the thermocouple readings for a small step increase in the heat flux was considered as the CHF condition on the test surface. The boiling phenomenon was recorded with the high-speed camera at each heat input after the test surface temperature (T_s) reaches the steady state. The T_s was assumed to reach a steady state when the difference between the average temperatures reported on each thermocouple is less than 0.1 K consecutively over a period of time. When the pressure in the boiling chamber increases above the set pressure, PID triggers the pump to circulate coolant in the condenser until the pressure in the chamber reaches the set pressure value. The power input was then turned down, and the heat flux achieved at the previous steady state was reported as the CHF.

3.2.3 DATA REDUCTION

The experiments involved measuring the pool boiling performance parameters such as heat flux and HTC.

The heat flux from the test surface is assumed to be uniform and can be estimated by the Fourier law of heat conduction. As explained earlier, the test piece and heater rod are surrounded by a Teflon shield. The Teflon masking resists the heat loss in the radial direction. In addition, copper will enable for a rapid spreading of heat in the axial direction. Hence, the heat flow within the test piece is unidirectional (axial), and a 1-D Fourier law of heat conduction, as shown in equation 3.1, can be adapted to measure the heat flux from the test surface.

$$q'' = -k_{Al} \frac{dT}{dx} \quad (3.1)$$

Here, $\frac{dT}{dx}$ is the temperature gradient along the height of the test piece. To measure the $\frac{dT}{dx}$ value, temperature recordings of three k-type temperature probes, which were

embedded in the test piece at different places (as shown in the Fig 3.6), are substituted in Taylor's backward series approximation, as shown in equation 3.2.

$$\frac{dT}{dx} = \frac{3T_1 - 4T_2 + T_3}{2\Delta x} \quad (3.2)$$

Where Δx is the distance between consecutive thermocouples.

The surface temperature of the test piece is estimated by the following equation 3.3.

$$T_s = T_1 - q'' \left(\frac{x_1}{k_{Al}} \right) \quad (3.3)$$

Where, x_1 is the distance between the test surface and first thermocouple from the test surface.

The HTC of boiling heat transfer between the test surface and working fluid is calculated by using equation 3.4.

$$h = \frac{q''}{T_s - T_{sat}} \quad (3.4)$$

3.2.4 UNCERTAINTY IN MEASUREMENTS

In the present experimental setup, three calibrated thermocouples were embedded into the aluminum work piece at various locations. The precision error in thermocouple location, accuracy errors in thermocouple readings, thermal conductivity of Al 6061, and deviation in the repeatability tests cause an inevitable experimental uncertainty. To estimate the experimental uncertainty in measuring pool boiling performance parameters such as heat flux, HTC, and surface temperature, the propagation of error method is used similar to Walunj and Sathyabhama (2018).

The deviation of the distance between the thermocouples due to manufacturing error is approximately 0.01 mm. The accuracy of each k- type thermocouple is experimentally verified by measuring the freezing and boiling points of water, and a match was found with the data provided by the manufacturer (± 0.1 °C). The standard deviation of the

thermal conductivity of Al 6061 is 2% in the operating temperature range (Radebaugh and Bradley 2018). For all the temperature measurements, a 95% confidence level was used. The standard deviation in the measurement of heat flux, surface temperature and heat transfer coefficient are estimated from the repeatability tests.

To measure the uncertainty in the heat flux, equation 3.5 was used and then dividing these uncertainty values with heat flux values calculated using equation 3.1, the percentage uncertainty in heat flux is obtained. In this work, a maximum uncertainty of 9.9% was observed.

$$U_{q''} = \sqrt{\left[\left(\frac{q''}{k_{Al}} U_{k_{Al}} \right)^2 + \left(\frac{3k_{Al}}{2\Delta x} U_{T_1} \right)^2 + \left(\frac{4k_{Al}}{2\Delta x} U_{T_2} \right)^2 + \left(\frac{k_{Al}}{2\Delta x} U_{T_3} \right)^2 + \left(\frac{q''}{2\Delta x} U_{\Delta x} \right)^2 + (\sigma_q)^2 \right]} \quad (3.5)$$

The uncertainty in measuring surface temperature was calculated using equation 3.6 and a maximum error of 0.25 °C was found at the highest heat flux.

$$U_{T_s} = \sqrt{\left[(U_{T_1})^2 + \left(\frac{x_1}{k_{Al}} U_{q''} \right)^2 + \left(\frac{q''}{k_{Al}} U_{\Delta x} \right)^2 + \left(\frac{q'' x_1}{k_{Al}^2} U_{k_{Al}} \right)^2 + (\sigma_{T_s})^2 \right]} \quad (3.6)$$

The uncertainty in calculating HTC was obtained using equation 3.7 and a maximum error of 10.25% was estimated at heat fluxes below 250 kW/m² and a maximum of 5% error for larger heat fluxes.

$$U_{HTC} = \sqrt{\left[\left(\frac{U_{q''}}{(T_s - T_{sat})} \right)^2 + \left(\frac{q''}{(T_s - T_{sat})^2} U_{T_s} \right)^2 + \left(\frac{q''}{(T_s - T_{sat})^2} U_{T_{sat}} \right)^2 + (\sigma_{HTC})^2 \right]} \quad (3.7)$$

As it is known that uncertainties could vary depending on the experimental conditions, measurement approaches, the instruments used, statistical confidence level, and the sample size, it is cautiously noted the heat flux and HTC uncertainties could have minor

deviations. However, it was found that these deviations will not impact the findings from a comparison perspective of the BHT performance of the three test surfaces.

3.2.5 REPEATABILITY AND VALIDATION OF THE TEST SETUP

Three test runs were conducted on the plain aluminium test substrate as depicted in Fig 3.7 to examine the reproducibility of the experimental results and the boiling curves showed good repeatability of the experimental data.

To validate the obtained test results, they were compared with the correlation (equation 3.8) proposed by Rohsenow (1952) as shown in Fig 3.8.

$$q'' = \mu_l h_{lv} \left[\frac{g(\rho_l - \rho_v)}{\sigma} \right]^{\frac{1}{2}} \left[\frac{C_{pl}(T_s - T_{sat})}{C_{sf} h_{fg} Pr_l^n} \right]^3 \quad (3.8)$$

Here, n is an experimental constant equal to 1 for pure water, and C_{sf} is the surface-fluid factor. The value of C_{sf} for bare aluminium-pure water combination is 0.0165, experimentally obtained by Righetti et al. (2020). It is seen from the figure that the correlation results agree well with the trend of experimental results and the mean absolute error between the experimental and the predicted values calculated from equation 3.9 is found to be 19.5%. The deviation or error between the experimental the predicted results were attributed to the difference in the surface characteristics, geometry, and the size of the boiling surface.

$$MAE = \frac{1}{i} \sum \frac{|q''_{pred} - q''_{exp}|}{q''_{exp}} \times 100 \quad (3.9)$$

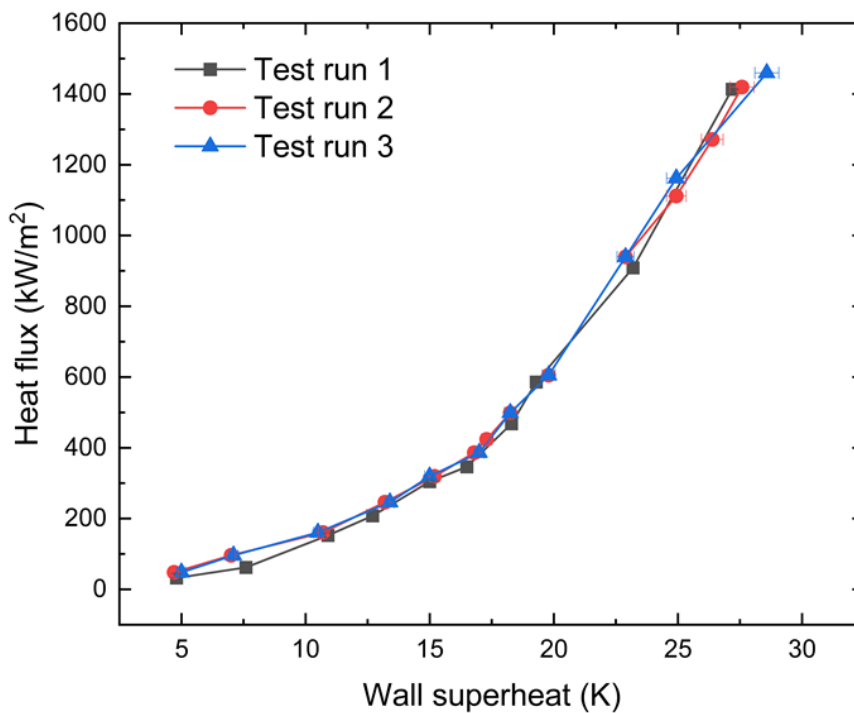


Figure 3.7 Repeatability of test setup

The present experimental results are compared with the experimental data obtained by Righetti et al. (2020) (green triangles), Godinez et al. (2019) (blue triangles) and Može et al. (2021) (purple triangles). It can be seen from the figure that the boiling curves drawn for the present experimental data and previous experimental works follow an identical trend. The maximum heat flux observed in Righetti et al. (2020) was lower compared with CHF values found in other works including the present work as the authors in Righetti et al. (2020) did not continue the experiments until CHF.

The CHF observed in this study is higher than the estimation made by Zuber (1959) (1200 kW/m^2) using the equation 3.10. A similar observation was made in the

experimental works of Godinez et al. (2019) and Može et al. (2021). The reason for the higher CHF values was attributed to the growth of a Boehmite (aluminum oxide hydroxide) layer on the aluminum test surface.

$$q'' = C \cdot h_{lv} \cdot \rho_v \left[\frac{\sigma \cdot g (\rho_l - \rho_v)}{\rho_v^2} \right]^{\frac{1}{4}} \quad (3.10)$$

Here, C is a dimensionless constant, typically taken as 0.131 for a horizontal surface.

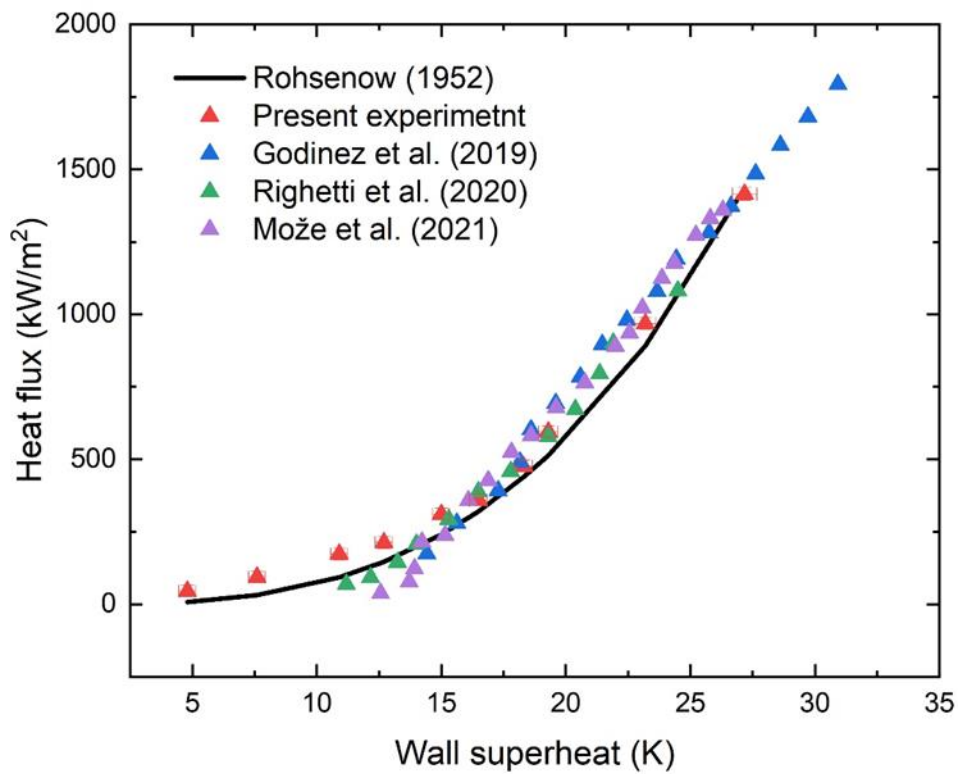


Figure 3.8 Validation of test setup.

3.3 HIGH-SPEED VISUALIZATION

3.3.1 PROCEDURE AND EQUIPMENT FOR HIGH-SPEED VISUALIZATION

High-speed visualization of the boiling phenomenon allows for the detailed observation of dynamic processes, such as bubble nucleation, growth, departure, and coalescence, in real-time. This enables a better understanding of the underlying mechanisms of BHT, including the interactions between bubbles and the heat transfer surface. In this experiment, a high-speed camera (AOS Promon 501) equipped with a NIKON 50 mm f/1.4D lens was used to capture the boiling phenomenon at an aspect ratio of 384×250 pixels and a frame rate of 1000 fps. The AOS imaging studio v 4.4 software interfaced the high-speed camera with a computer, allowing adjustments to the frame rate, aspect ratio, exposure, and shutter speed. Videos were recorded at all heat inputs until the CHF was reached. Only a few videos were processed to measure bubble characteristics up to the heat flux level that identifies the discrete bubble regions. At higher heat flux levels, the crowding of bubbles and their rigorous coalescence made visualization extremely difficult and unreliable.

3.3.2 ESTIMATION OF BUBBLE DEPARTURE DIAMETER

Bubble grows with the increase in heat input and departs from the surface when the bubble buoyancy force dominates the force that tends to pin the bubble to the surface. The spherical shape of the bubble slightly turns to elliptical profile at its bottom as shown in Fig 3.9. Thus measurement of bubble departure diameter requires certain assumption to obtain the equivalent bubble diameter. As suggested by Siegel and Keshock (1964), bubble departure diameter is estimated as the arithmetic mean of x and y , which were estimated by MATLAB image processing.

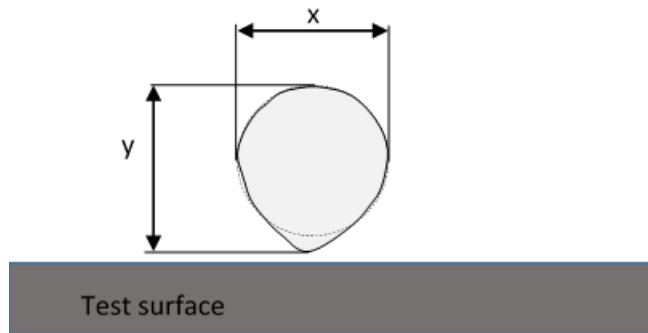


Figure 3.9 Measurement of bubble departure diameter.

The captured videos were manually observed frame by frame after being converted into individual frames using the MATLAB video labeller tool. Frames containing departed bubbles were identified and processed using MATLAB image processing to draw a manual bounding box around each departed bubble. The bounding box measures the horizontal ('x') and vertical ('y') axis lengths of the departed bubble in pixels

A reference object of known dimensions was also captured with the same camera position, frame rate, and settings. To retrieve the horizontal and vertical dimensions in terms of pixels for the reference object, a bounding box was drawn for the reference object as explained above. Figure 3.10 (a) and (b) shows the reference object and a departing bubble enclosed in the bounding box. Since the actual dimensions of the reference object are available, equation 3.11 is used to convert the dimensions of 'x' and 'y' from pixels to mm.

$$\begin{aligned}
 &x \text{ or } y \text{ in mm} \\
 &= \frac{\text{Size of the departed bubble (pixels)} \cdot \text{Size of reference object (mm)}}{\text{Size of the reference object (pixels)}}
 \end{aligned}
 \tag{3.11}$$

The time-dependent behavior in the shape of the departing bubble and inconsistency in identifying the edges of the departing bubble may lead to uncertainty in the bubble departure diameter measurement. To minimize the error in estimating bubble departure

diameter, at least three repeated measurements were taken for the same bubble. A maximum error of 15% was observed in the entire set of measurements.

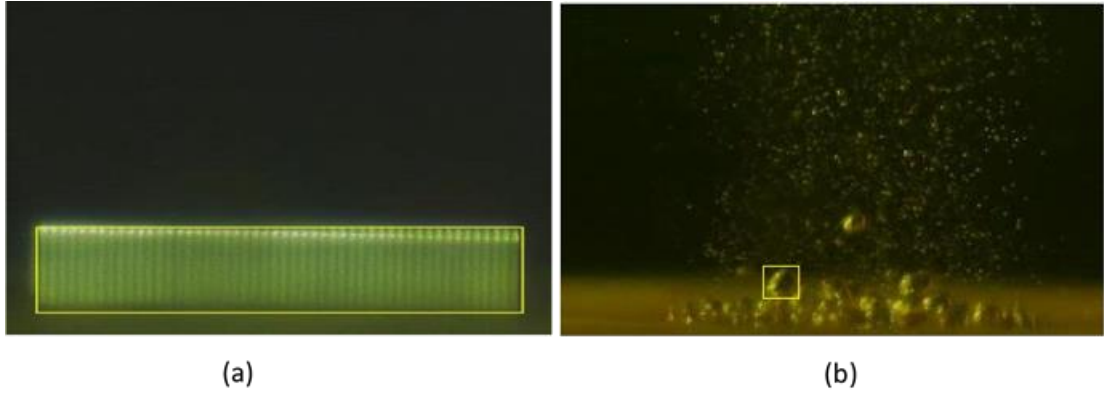


Figure 3.10 Bounding box inserted on a) reference object and b) departing bubble.

3.3.3 ESTIMATION OF BUBBLE DEPARTURE FREQUENCY

The number of bubbles departing from a bubble nucleation site over a period of time represents the bubble departure frequency. In the bubble ebullition cycle, t_g represents the bubble growth period and t_w represents the waiting period between two consecutive bubbles from a bubble nucleation site. The growth and the waiting periods of the ebullition cycle are manually counted from the recorded videos using MATLAB video labeler. Then f of one bubble nucleation site is obtained from equation 3.12.

$$f = \frac{1}{t_w + t_g} \quad (3.12)$$

The equation mentioned above gives the bubble departure frequency from a single nucleation site. Therefore, an average of bubble departure frequencies from 3 to 5 bubble nucleation sites was reported as the average bubble departure frequency. The difference between the departure frequencies of various bubble nucleation sites was within the range bound of $\pm 10\%$, based on measurements taken from several sets of bubble nucleation sites. An increase in the heat flux leads to lateral bubble coalescence

and makes the measurement of bubble departure frequency unpredictable. The bubble departure frequency measurements considered in this work are from isolated bubble nucleation sites.

3.3.4 ESTIMATION OF NUCLEATION SITE DENSITY

Active NSD was estimated by counting the number of bubble nucleation sites divided by the test surface area. The high-speed video files were analyzed frame by frame for this purpose. The number of sites counted on any instantaneous frame is less than their cumulative number. This is because, any bubble nucleation site which is active at least once over several ebullition cycles is considered active. Therefore, to approximate the number of active sites in the present work, the procedure suggested by Mchale and Garimella (2010). Gerardi et al. (2010) reported the uncertainty in the active NSD as the difference in the number of sites obtained by counting the active sites for several times in the same frame. In the present work, the uncertainty is observed as $\pm 2\%$ at low heat flux levels. The uncertainty increases with the heat flux as the field of view is frequently obstructed by the bubble crowd. The maximum uncertainty of $\pm 10\%$ is observed in the present work.

3.4 RESULTS AND DISCUSSION

3.4.1 BOILING CURVES

Figure 3.11 illustrates the heat flux dissipated from the PS in relation to the wall superheat, with regression lines drawn for both the natural convection and nucleate boiling regimes. The corresponding regression line equations are presented in equations 3.13 and 3.14. The curve shows a steep increase in the slope within the nucleate boiling regime, indicating large amount of heat dissipation at a finite temperature difference.

$$\propto (T_s - T_{sat})^{1.58} \text{ for natural convection regime} \quad (3.13)$$

$$\propto (T_s - T_{sat})^{2.65} \text{ for nucleate boiling regime} \quad (3.14)$$

Gaertner (1965) proposed that nucleate boiling regime consists of three phases: the discrete or isolated bubble phase, the transition phase, and the vapor mushroom phase. Snapshots of each phase are shown in Fig 3.11. In the discrete bubble phase, bubbles depart in the shape of spheres. As the heat flux increases, the departure frequency from the nucleation sites increases, and the bubbles appear to form a vapor column. Further increases in heat flux cause the bubbles to merge and depart in the shape of a mushroom. The transition phase is where both discrete and mushroom-shaped bubbles coexist.

Figure 3.12 shows that the heat flux dissipated at a given wall superheat increases from PS to BiS. The incipient temperatures for bubble nucleation of all the three surfaces are given in Table 3.3. The incipient temperature required on BiS is lower than on the other two surfaces. The presence of liquid lubricant puddles creates in-plane temperature variations on the BiS, which reduces the wall superheat required for the onset of nucleation (e.g., Rahman et al. 2015). The nucleation on the UOS surface is delayed due to its highly wetting (omniphilic) nature.

Table 3.3 Bubble incipient temperature.

Test surface	Incipient temperature, °C
PS	~ 11
UOS	~ 12
BiS	~ 7

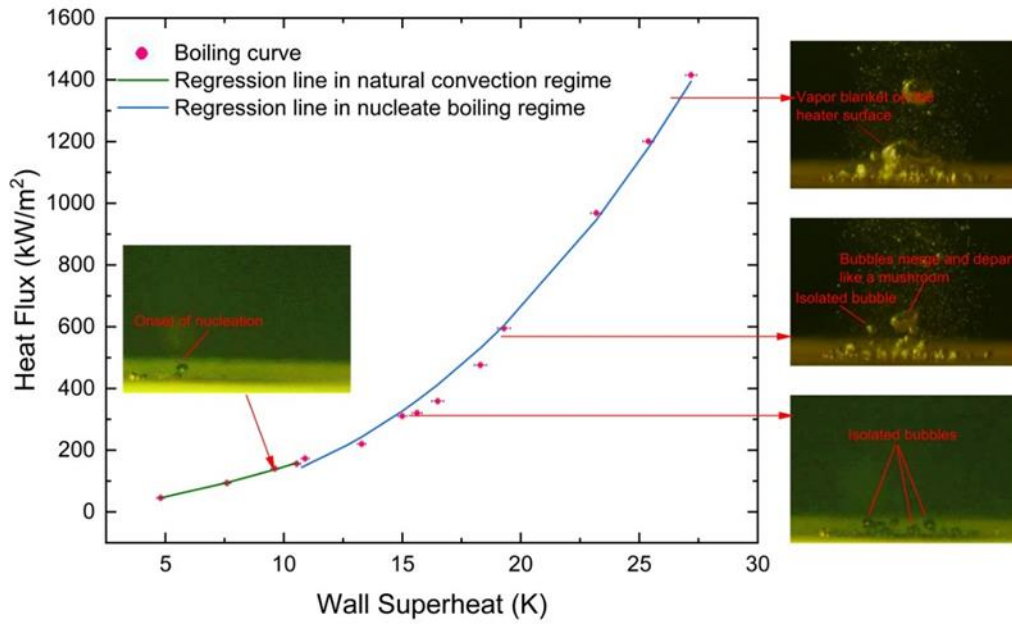


Figure 3.11 Boiling curve of PS showing regression lines in natural convection and nucleate boiling heat transfer.

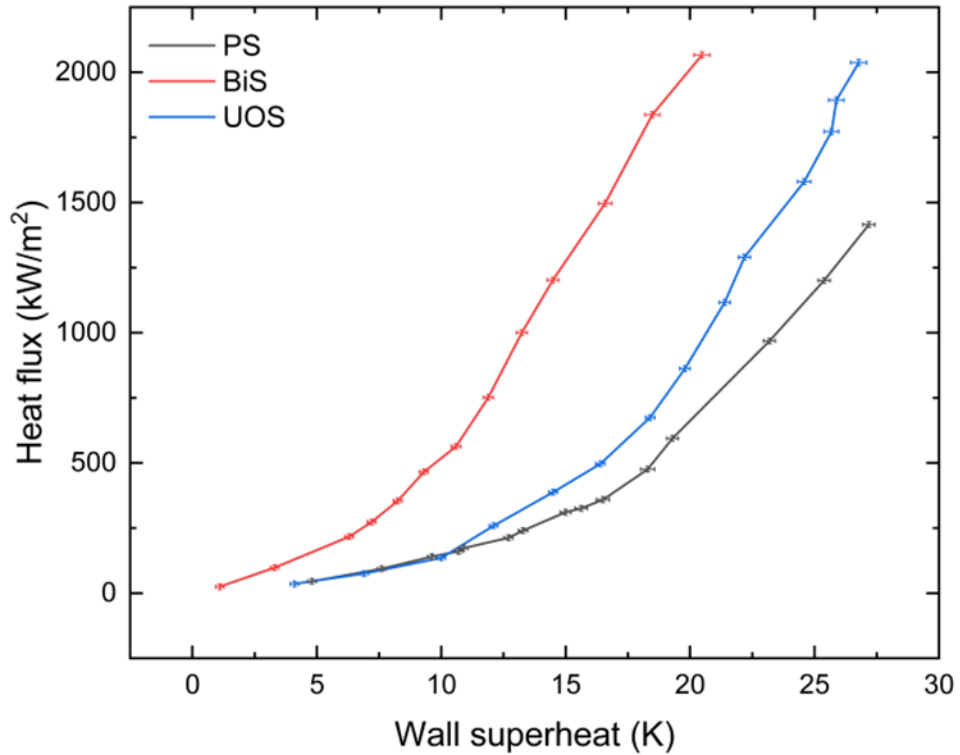


Figure 3.12 Heat flux as a function of wall superheat.

As mentioned earlier, unlike SLIPS, the excess lubricant on BiS is wiped off after infusing the micro/nano cavities. This prevents the formation of a smooth oil layer that would act as a thermal barrier and cause homogeneous boiling (where vapor nuclei form in the bulk of the liquid). For homogeneous boiling, the wall superheat required to initiate and sustain boiling would need to be tens of degrees higher than the saturation temperature of water. However, as shown in Table 3.3, the bubble incipience temperature on the BiS is approximately 7 °C, confirming that bubble nucleation occurs on the solid islands of the BiS (heterogeneous boiling) rather than in the bulk of the liquid. Figure 3.12 also indicates that the heat flux dissipated from the BiS at around 7 °C is 273.5 kW/m², increasing to 2066 kW/m² (about 40% higher than on the PS) at a wall superheat of around 20 °C. Such a steep increase in heat flux dissipation with only a few degrees of wall superheat increase is possible only with heterogeneous boiling.

Furthermore, it is important to note that the capillary force induced by the micro/nano cavity network on the BiS effectively holds the liquid lubricant in the sub-surface cavities of the BiS during nucleate boiling. Otherwise, the boiling curves for BiS and UOS would almost coincide in Fig 3.12. Additionally, the CHF values for BiS and UOS are nearly the same despite the smaller boiling area on the BiS (i.e., only the solid islands). This suggests that the increase in surface area has not contributed to the CHF enhancement on the BiS (compared to the PS), unlike the UOS or other enhanced boiling surfaces such as micro channels, micro/nano-pillars, and sintered particles.

Figure 3.13 shows the variation of HTC with the heat flux on all the tested surfaces. The HTC of the BiS is $\sim 100\%$ and $\sim 35\%$ higher than on the PS and UOS, respectively. The augmented convective currents induced by the in-plane temperature differences created by the lubricant puddles enhance the HTC of BiS in the natural convection region. The nucleate boiling region on the BiS begins earlier than on the other surfaces due to low incipient temperatures. The lubricant puddles on the BiS avoid lateral bubble merger and provide separate passageways to the departing bubbles and the incoming liquid, which extends the isolated bubble phase in nucleate boiling regime. Hence the HTC in the nucleate boiling regime of BiS is higher than on the other two surfaces.

Holguin et al. (2017) reported the findings of pool boiling experiments on BiS fabricated on a copper substrate at atmospheric pressure under saturated conditions using the dielectric liquid PF-5060. It was observed that, compared to a plain copper surface, BiS could simultaneously enhance the heat flux limit by approximately 2.2 times and the maximum HTC by about 7.5 times. Although the CHF (2066 kW/m^2) and maximum HTC ($101 \text{ kW/m}^2\cdot\text{K}$) values obtained in the present study (using water as the boiling liquid) are higher than those reported by Holguin et al. (2017) with PF-5060, the percentage enhancement in HTC and CHF in their experiments (7.5 times and 2.2 times, respectively) is much higher than in the present work (2 times and 1.47 times). The differences in the thermos-physical properties of PF-5060 and water could explain these relatively lower enhancements (Cvijovic et al. 2022).

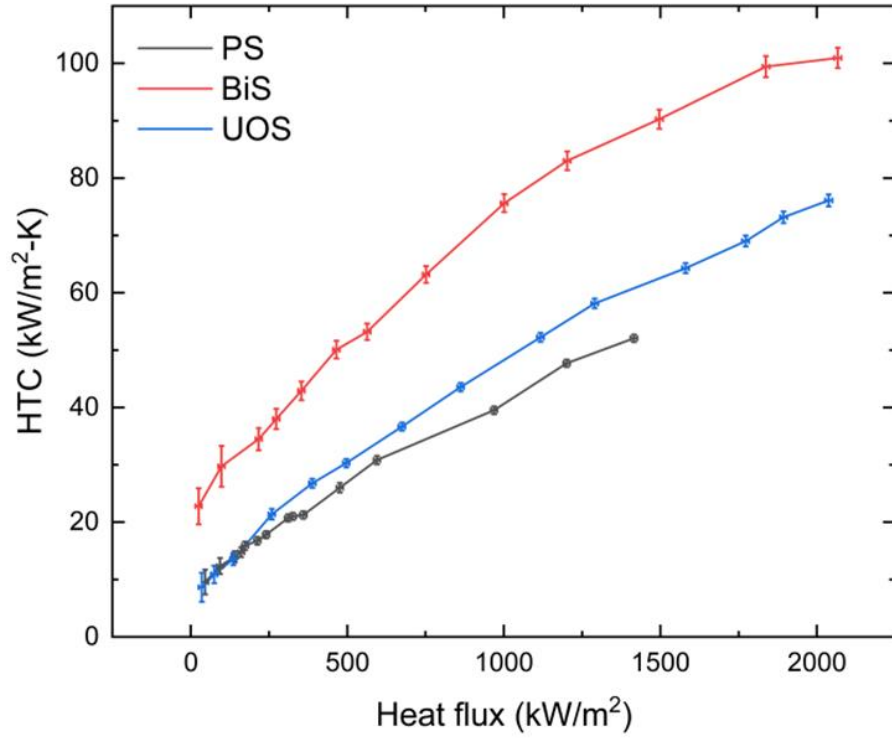


Figure 3.13 HTC as a function of heat flux.

The non-dimensional Jakob number (Ja) is the ratio of sensible heat to the latent heat absorbed during the phase change process. Figure 3.14 represents the variation of heat flux with respect to Jakob number for all the surfaces. It can be seen from the curves that the Jakob number increases rapidly at lower heat flux and slowly at higher heat fluxes, which indicates the domination of latent heat at higher heat fluxes.

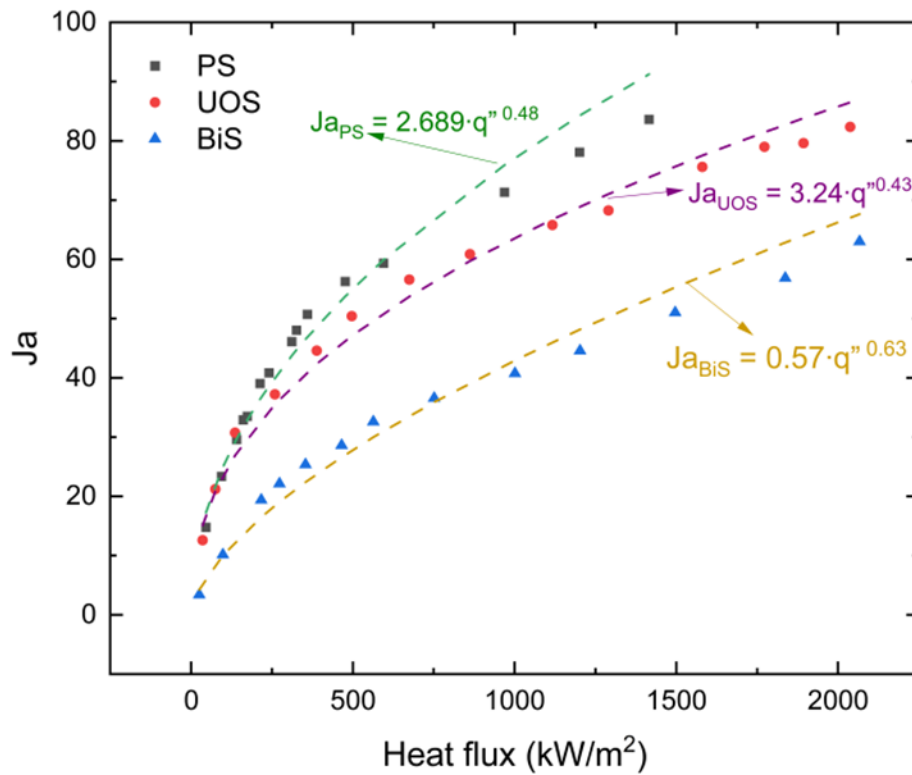


Figure 3.14 Jakob number as a function of heat flux

The power law fit that shows the dependence between heat flux and the Jakob number for all the surfaces is shown as dashed lines. Since the precise relationship between the Jakob number and other nucleation quantities is not available in the literature, these power law fits may be useful in interpreting other figures that follow Jakob number as an independent variable. From the power law fits, it is observed that the coefficient of q'' decreases and its power increases for the BiS compared to the PS and the UOS. The lower Jakob number on the BiS can be considered as a result of the cumulative effect of the coefficient and the power that in turn would be related to the active NSD and efficient vapor bubble dynamics.

3.4.2 HIGH-SPEED VISUALIZATION

The inception, growth, departure, and other characteristics of the bubble were recorded by high-speed camera. The visualization images revealed that the size of the departing bubble on the PS is larger compared to that on the copper surfaces from the literature (Chang and Ferng 2019; Thiagarajan et al. 2015). This size difference is attributed to the difference in the thermo-physical properties of the substrate as observed by Aktinol and Dhir (2012) where the effect of substrate properties on the bubble dynamics were studied.

3.4.2.1 Bubble Departure Diameter

Several correlations were developed in the past to predict the bubble departure diameter. The commonly adopted correlations are given in Table 3.4. Balancing the buoyancy force with the surface tension force at atmospheric pressure, Friz (1935) developed a correlation to predict the bubble departure diameter. Kocamustafaogullari and Ishii (1983) modified the Friz (1935) correlation to predict the bubble departure diameter at any pressure. Cole (1967) developed a correlation by summarizing the existing results. Tolubinsky and Kostanchuk (1970) developed a correlation to predict bubble departure diameter in subcooled boiling. Figure 3.15 shows the comparison of experimental bubble departure diameter values with the predicted values using the correlations. It can be observed from the graph that the experimental bubble departure diameter values of the bare aluminum surface (PS) is close to the predicted values obtained by Fritz (1935) and Kocamustafaogullari and Ishii (1983) correlations with a mean absolute error of 9.34% and 8.5%, respectively.

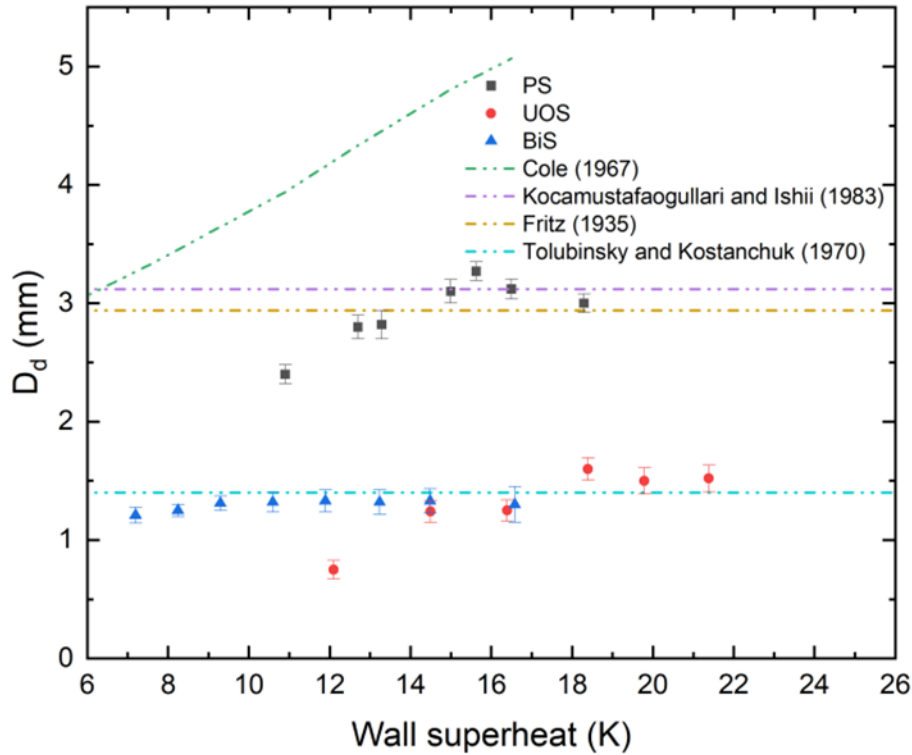


Figure 3.15 Comparison of measured bubble departure diameter with correlations.

Figure 3.16 shows the comparison of the bubble departure diameter of PS, UOS, and BiS with the experimental values measured by Chang and Ferng (2019), Mchale and Garimella (2010), and Thiagarajan et al. (2015) as a function of Jakob number. From the definition of Jakob number, increasing Jakob number implies relatively low vapor generation which requires the bubble to grow to a larger size before it can depart (i.e., large bubble departure diameter values for increasing Jakob number in the figure for regular or PS). As shown in the figure, the bubble departure diameter values of the PS are higher than the literature data. The difference in the substrate material, contact angle, and topographical features could be the reason for this variation. Unlike PS and UOS, the bubble departure diameter on the BiS is found to be weakly dependent on the Jakob number. The average diameter of the departing bubble from the BiS is also smaller than PS and UOS, it varies between 1.21 mm and 1.33 mm for a heat flux range

of 275-1000 kW/m². The departing diameter on the BiS is approximately 56% lower than on the PS at ~ 500 kW/m². The incoming rewetting liquid force and the presence of the liquid lubricant with a different surface tension value than the boiling liquid may have caused the early departure and could be the reason for the smaller departure diameter on the BiS. The surface tension force pins the bubble and allows it to grow larger on the PS. The schematic of bubble behaviour at different time lines on BiS and PS is depicted in Fig.3.17. The bubbles on the PS grow larger and tend to merge whereas the bubbles on the BiS tend to depart early at lower diameters due to the presence of the lubricant puddles.

Table 3.4 Correlations for the prediction of bubble departure diameter.

Authors	Correlation
Fritz (1935)	$D_d = 0.0208\theta \left[\frac{\sigma}{g(\rho_l - \rho_v)} \right]^{\frac{1}{2}}$
Cole (1967)	$D_d = 0.04 Ja \left[\frac{2\sigma}{g(\rho_l - \rho_v)} \right]^{\frac{1}{2}}$
Kocamustafaogullari and Ishii (1983)	$D_d = 0.0012(\rho^*)^{0.9} 0.0208\theta \left[\frac{\sigma}{g(\rho_l - \rho_v)} \right]^{\frac{1}{2}}$
Tolubinsky and Kostanchuk (1970)	$D_d = \min \left(D_{ref} \exp \left(-\frac{T_{sat} - T_l}{\Delta T_{ref}} \right), D_{max} \right)$ $D_{ref} = 0.64 \text{ mm}$ $\Delta T_{ref} = 45 \text{ K}$ $D_{max} = 1.4 \text{ mm}$

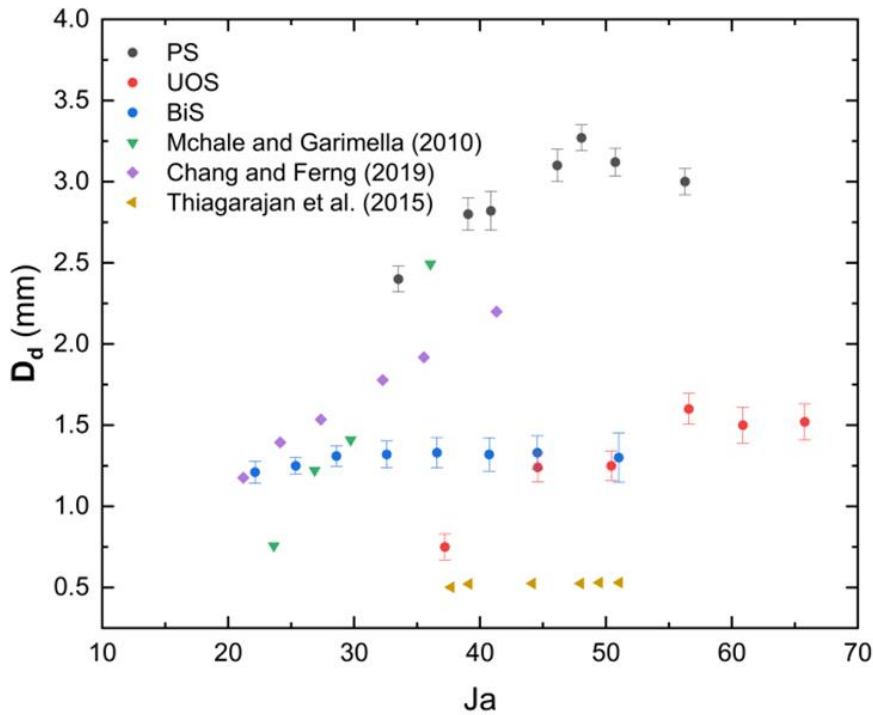


Figure 3.16 Comparison of measured bubble departure diameter with literature.

3.4.2.2 Bubble Departure Frequency

The average departure frequency on PS, UOS and BiS with respect to Jakob number are shown in Fig 3.18. The linear fit for each surface is also given in the figure. From the definition of Jakob number, increasing Jakob number implies increasing wall superheat which reduces the t_w and t_g thereby increasing bubble departure frequency. The linear fits show that the slope of the BiS is steeper than the other surfaces. It can also be observed from the curve that the bubble departure frequency on all the surfaces increases with the Jakob number, similar to literature (Chang and Ferng 2019; McHale and Garimella 2010; Thiagarajan et al. 2015). The presence of liquid lubricant puddles will result in large in-plane temperature differences on the BiS which keeps the nucleation sites (solid islands) hotter than the liquid puddles. Therefore, the bubble growth and waiting times on the BiS are lower than the other surfaces. Accordingly,

higher departure frequencies were observed on the BiS. The bubble growth rate on the PS is a result of the balance of the surface tension force and the liquid-vapor pressure difference. On the UOS, the cause of a significant delay in the waiting time between consecutive bubbles can be attributed to its poor nucleation characteristics. Therefore, the departure frequencies of PS and UOS are lower than the BiS.

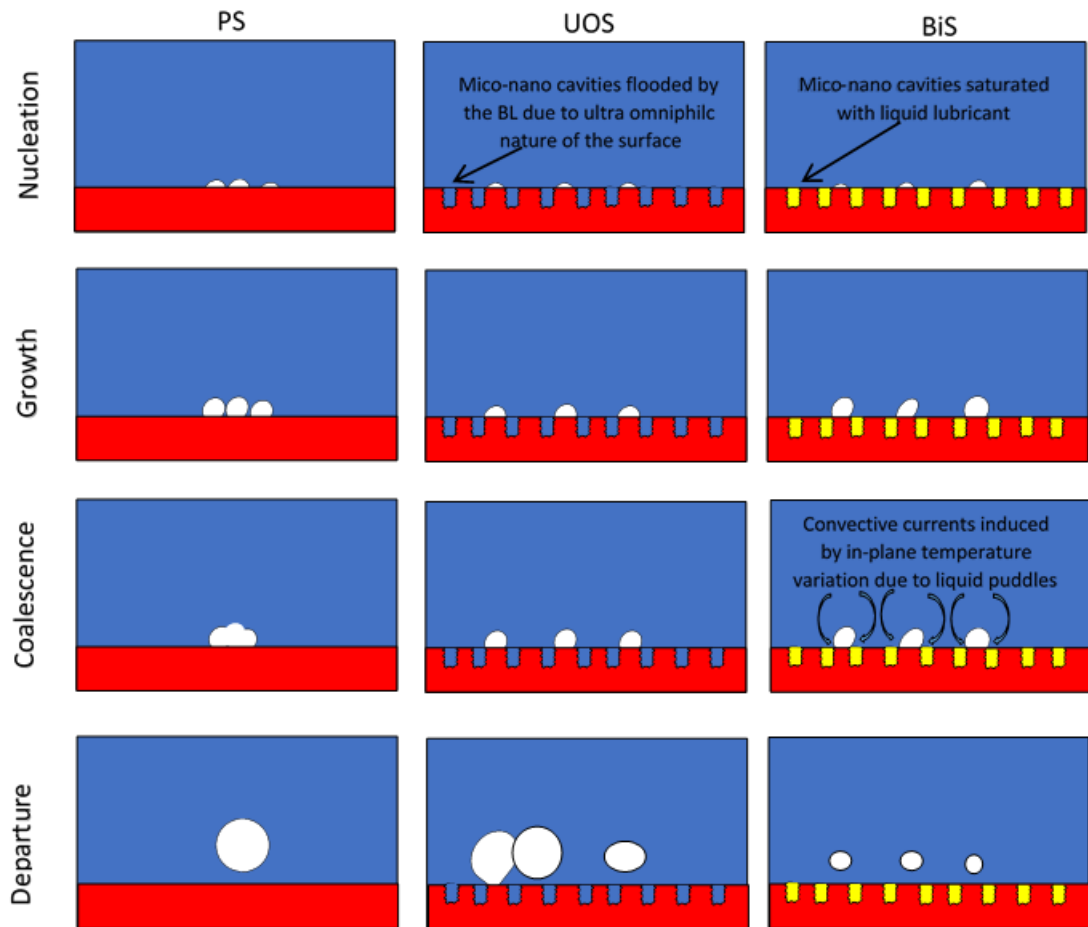


Figure 3.17 Schematic of the observed bubble behavior on PS, UOS and BiS at various ebullition stages.

The product of bubble frequency and departure diameter (fD_d) is calculated and compared with the well-known correlations of Jakob and Fritz (1931), Peebles and Garber (1953), and Zuber (1963) in Fig 3.19. All the correlations are indicated in Table 3.5. Jakob and Fritz (1931) correlated the fD_d from the experimental data, whereas

Zuber (1963) and Peebles and Garber (1953) developed the correlation by making assumptions to the theoretical arguments.

Table 3.5 Correlations for the prediction of $f \cdot D_d$.

Authors	Correlation
Jakob and Fritz (1931)	$f \cdot D_d = 0.078$
Peebles and Garber (1953)	$f \cdot D_d = 1.18 \left[\frac{t_g}{(t_g + t_w)} \right] \left[\frac{\sigma g (\rho_l - \rho_v)}{\rho_v^2} \right]^{\frac{1}{4}}$
Zuber (1963)	$f \cdot D_d = \left(\frac{1.18}{2} \right) \left[\frac{\sigma g (\rho_l - \rho_v)}{\rho_v^2} \right]^{\frac{1}{4}}$

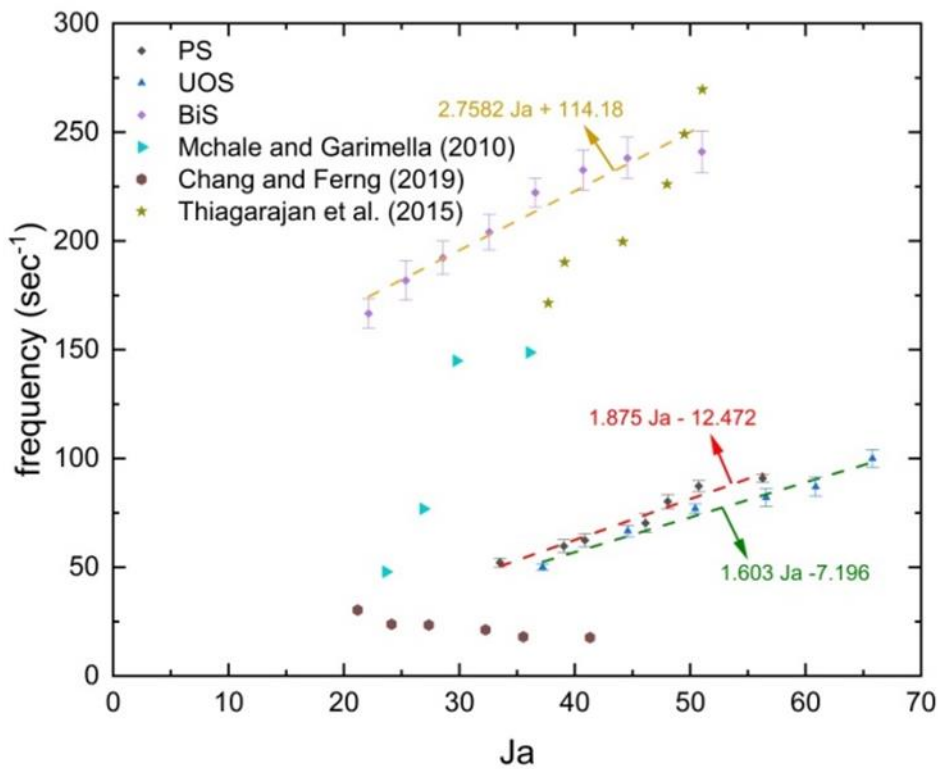


Figure 3.18 Variation of measured bubble departure frequency of PS, UoS, and BiS with Jakob number and comparison with other experimental works.

From the Fig 3.19 it can be observed that experimental $f \cdot D_d$ values do not match with any correlation. However, $f \cdot D_d$ of all the surfaces follows the trend of Peebles and Garber (1953). The figure also shows that $f \cdot D_d$ values of BiS are higher than the other two surfaces. Though the departure diameters on BiS are smaller than those on the PS, its higher frequency rates resulted in the maximum $f \cdot D_d$ on BiS. Therefore, BiS surfaces are more effective in BHT.

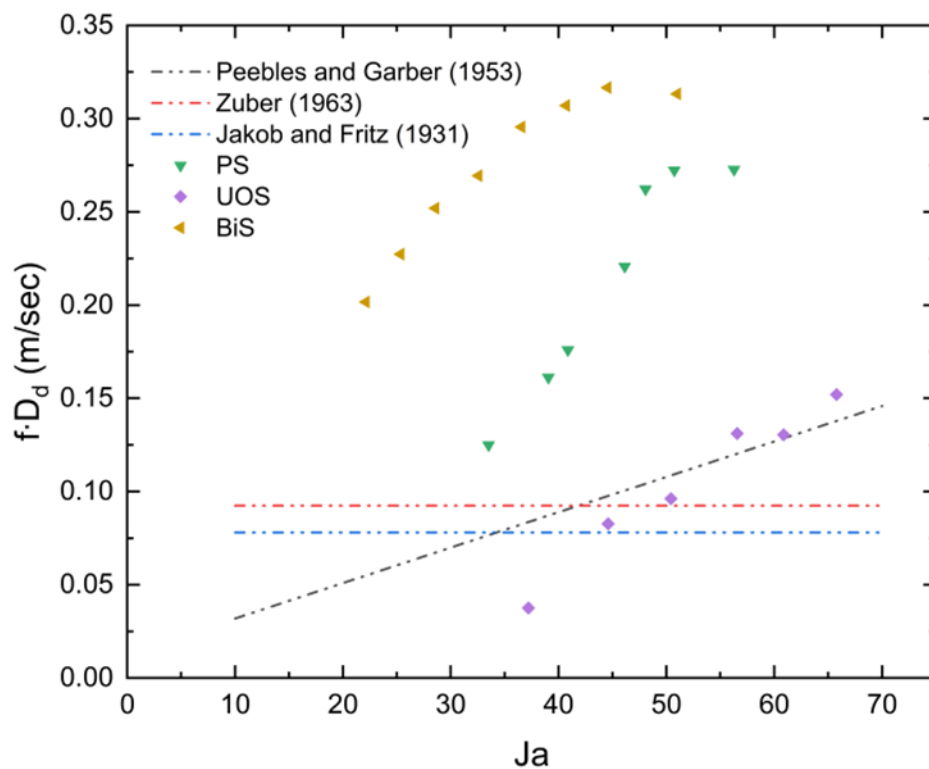


Figure 3.19 Comparison of the $f \cdot D_d$ of PS, UoS and BiS with those predicted from the correlations at different Jakob numbers.

3.4.2.3 Nucleation Site Density

The NSD is measured by analyzing the recorded videos. The NSD of PS, UoS, and BiS are plotted against the Jakob number in Fig 3.20 and compared with the predicted values of NSD by empirical correlations (indicated in Table 3.6). The figure indicates

that the experimental NSD values in general are much lower than the predicted values of Lemmert and Chawla (1977). The NSD values of PS are closer to the correlation of Kocamustafaogullari and Ishii (1983), which was obtained by correlating the experimental data through a parametric study.

Table 3.6 Correlations for the prediction of NSD.

Authors	Correlation
Lemmert and Chawla (1977)	$NSD = (C^z(T_s - T_{sat}))^z$, $C = 210$, $z = 1.804$
Kocamustafaogullari and Ishii (1983)	$NSD = \frac{f(\rho^*)}{D_d^2} \left[\frac{4\sigma T_{sat}}{\rho_g(T_s - T_{sat})h_{fg}D_d} \right]^{-4.4}$; $f(\rho^*) = 2.157 \times 10^{-7} \rho^{*-3.2} (1 + 0.049\rho^*)^{4.13}$

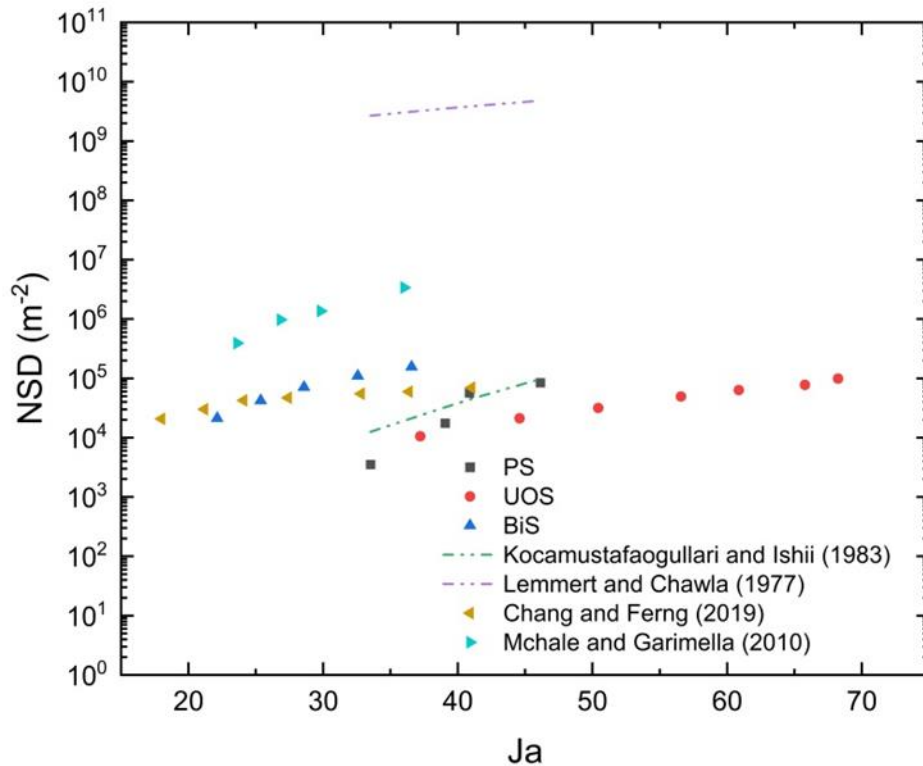


Figure 3.20 Variation of the active NSD of PS,UOS, and BiS with Jakob number and comparison with predicted results and literature data.

Figure 3.20 also compares the present experimental data with the experiments reported in the literature (Chang and Ferng 2019; McHale and Garimella 2010). It can be observed that the measured NSD on PS follows a similar trend and order of magnitude with those predicted by Kocamustafaogullari and Ishii (1983). BiS is observed to have more active NSD, and it has approximately 30% higher NSD at $\sim 500 \text{ kW/m}^2$ compared to the UOS, which has the lowest active NSD among all surfaces. The well-distributed lubricant puddles allow the solid islands to maintain the superheat required to sustain the active NSD on the BiS.

The snap shots of boiling phenomenon on PS, UOS, and BiS at different heat fluxes are provided in Fig 3.21. On the PS, topographical features capable of activating the nucleation sites are relatively absent and the surface tension forces are predominant. Hence, the bubbles on the PS grow larger and they cover the entire surface with relatively few active nucleation sites. As the heat flux increases, the bubble pins to the surface and grows and eventually merges with the adjacent bubble. This extensive horizontal coalescence leads to the inefficient rewetting and early occurrence of CHF.

The UOS have a strong affinity for liquid rewetting. Therefore, higher wall superheats are required for bubble incipience. It can be seen from the snap shots that the active NSD of the UOS is lower than the other two surfaces at any given heat flux. Smaller departure diameters, higher waiting periods, and lower departure frequencies were observed. The efficient rewetting of the dry spots at higher heat fluxes will delay the CHF. In general, convective heat flux is postulated to be the dominant mechanism on the UOS compared to the other surfaces. This argument is also supported by the $f \cdot Da$ values of the UOS as shown in Fig 3.19.

The snapshots of the boiling phenomenon on BiS, as given in Fig.3.21, show that the active NSD on BiS are higher than on the other surfaces. The liquid lubricant puddles on the BiS provide for easy and separate parallel pathways for liquid rewetting and vapor bubble removal in addition to denying the lateral bubble merger by preventing the growth of bubbles. These phenomena collectively extend the discrete bubble regime on the BiS. The solid islands on the BiS remain hotter than the adjacent liquid puddles. Thus, nucleation on the solid islands results in faster growth rates and negligible waiting periods, resulting in a significant bubble departure frequency. Consequently, the HTC

measured on the BiS is higher than on the PS and the UOS and the CHF is as good as on the UOS and higher than on the PS.

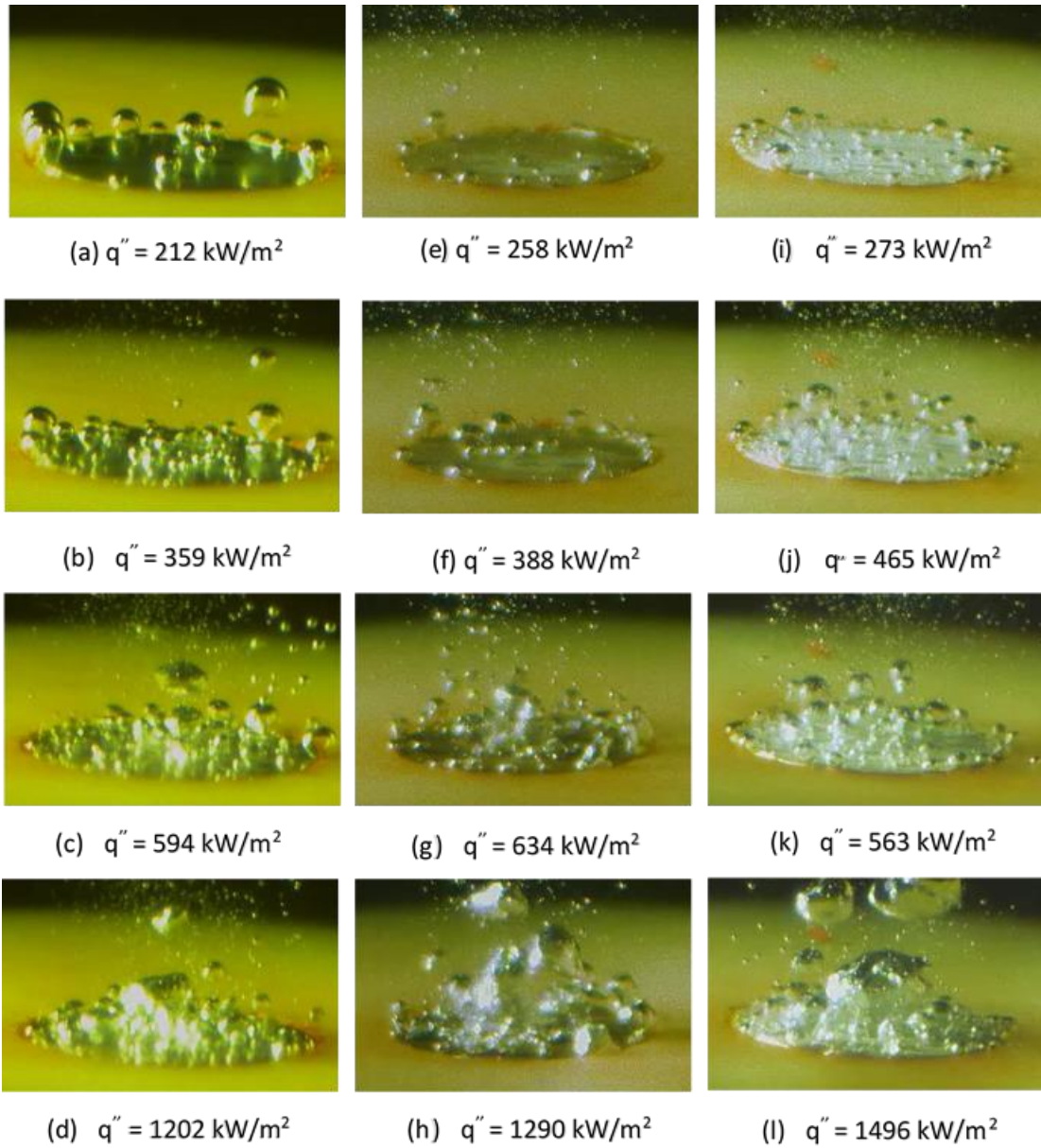


Figure 3.21 Snap shots of boiling phenomenon at different heat fluxes (a-d) PS (e-h) UoS (i-l) BiS.

CHAPTER 4

MITIGATION OF INORGANIC SCALING AND CORROSION

4.1 SIMULATED BRACKISH WATER

Brackish water is defined as water with salinity levels falling between freshwater and seawater, or water containing chlorine (Cl⁻) concentrations exceeding 400 mg/L. The Total Dissolved Salts (TDS) in brackish water typically range from 1000 mg/L to 15000 mg/L. Sources of brackish water include areas where river water mixes with seawater, such as estuaries, mangroves, and brackish lakes. The TDS of brackish water tends to rise during high tidal periods and decrease during the rainy season. In addition to electrolytes and dissolved minerals, natural brackish water sources also contain suspended particulates, organic matter, and biological substances. Consequently, desalinating brackish water can lead to bio-fouling, organic fouling, particulate fouling, and inorganic fouling occurring simultaneously. To avoid other types of fouling agents and maintain a consistent salinity level in all experiments, a simulated brackish water was utilized in the current study. While sodium chloride (NaCl) is the primary component, other salts are also present in brackish water. To replicate actual brackish water conditions, 9000 mg of aquarium salt was added to 700 ml of tap water and then adjusted to a total volume of 1000 ml. The TDS and ion composition of the simulated brackish water are detailed in Table 4.1. Previous studies on scaling mitigation have simulated feed waters as either carbonate-rich or sulfate-rich to investigate carbonate fouling (alkaline) or sulfate fouling (non-alkaline) mechanisms. However, real brackish water contains both carbonates and sulfates. Therefore, simulating actual brackish water is a more practical approach for scaling mitigation research. For consistency, corrosion mitigation experiments were also conducted using simulated brackish water with the same composition.

Table 4. 1 The concentrations of cations and anions in the simulated brackish water.

Constituent	Concentration (mg/L)
Ca^{2+}	767
Mg^{2+}	581
Na^+	1252
HCO_3^-	409
SO_4^{2-}	1359
Cl^-	5060
K^+	38
<i>Others</i>	344
<i>TDS</i>	9810

4.2 INORGANIC SCALING

4.2.1 TEST SECTION AND EXPERIMENTAL PROCEDURE

A laboratory-scale test setup, as shown in Fig 4.1 was used to conduct experiments and investigate the impact of inorganic fouling on the test surface. The setup consisted of a flexible silicon heating sheet positioned between two metal plates and connected to a DC power supply. A circular workpiece with a diameter of 3.5 inches was attached to the metal-heater assembly. To monitor the temperature of the substrate, a k-type thermocouple probe was inserted into a 1 mm diameter and 2 cm deep hole drilled in the radial periphery of the workpiece. The thermocouple probe was coated with thermal paste to ensure proper thermal contact. The outer periphery of the workpiece was covered with a centrally holed circular gasket, and a borosilicate glass tube was placed on top of it. Another gasket of similar size was placed on the upper end of the glass tube. The glass tube was filled with a measured amount of brackish water (200 ml), and a glass funnel was placed upside down on the gasket. A plywood sheet with a central hole was then placed on the funnel, and the entire assembly was secured tightly with bolts and nuts. A condensate collecting flask was connected to the test setup assembly using a hose pipe.

Prior to conducting the experiment, the weight of each test surface (PS, UOS, and BiS) was measured using a digital balance with a precision of four decimal places. Once the test setup was assembled and securely fixed, the DC power source was activated. The power supplied to the heating sheet gradually increased until the temperature of the test surface reached 115 °C, which exceeds the boiling point of the working fluid under atmospheric conditions. As a result, bubble incipience occurred on the test surface due to the elevated temperature, leading to the boiling of the brackish water. Consequently, the brackish feed began to vaporize, and over time, the vapors passed through the hose pipe and condensed in a collecting flask. Simultaneously, super-saturated mineral salts precipitated on the test surface. The amount of condensate collected in the flask was recorded at 15-minute intervals. After 120 minutes, the DC power supply was reduced, and the final amount of condensate in the flask was recorded once the test setup had returned to room temperature. The remaining residue was then drained, and the fouled surface was thoroughly cleaned using a paper towel. The weight gained as a result of fouling was determined by subtracting the initial weight of the test surface from the final weight after cleaning. The reported results in this study represent the average of three experimental trials, with the standard deviation from the mean depicted as the error in the graphs. To examine the fouling characteristics of each test surface, the fouled surfaces were sliced into smaller specimens and analyzed for crystallization patterns using a field emission scanning electron microscope (FESEM) and an optical 3D profilometer.

All the monitoring and measuring devices used in the experiment, including k-type thermocouple, digital weighting balance, and condensate collecting flask, have been fully calibrated. The k-type thermocouple underwent experimental calibration by measuring the freezing and boiling points of water. The obtained readings were found to deviate within ± 0.1 °C, which aligns with the manufacturer's specified accuracy for the thermocouple. Further the accuracy of digital weighing balance and condensate collecting flask were regularly assessed by comparing the measurements obtained on them against a standard reference. Further, the digital weighing balance is maintained in a clean room environment to prevent the accumulation of dust particles that could potentially impact measurement accuracy, while the condensate collecting flasks are

regularly cleaned to ensure they are free from any residues and stored in a temperature-controlled environment.

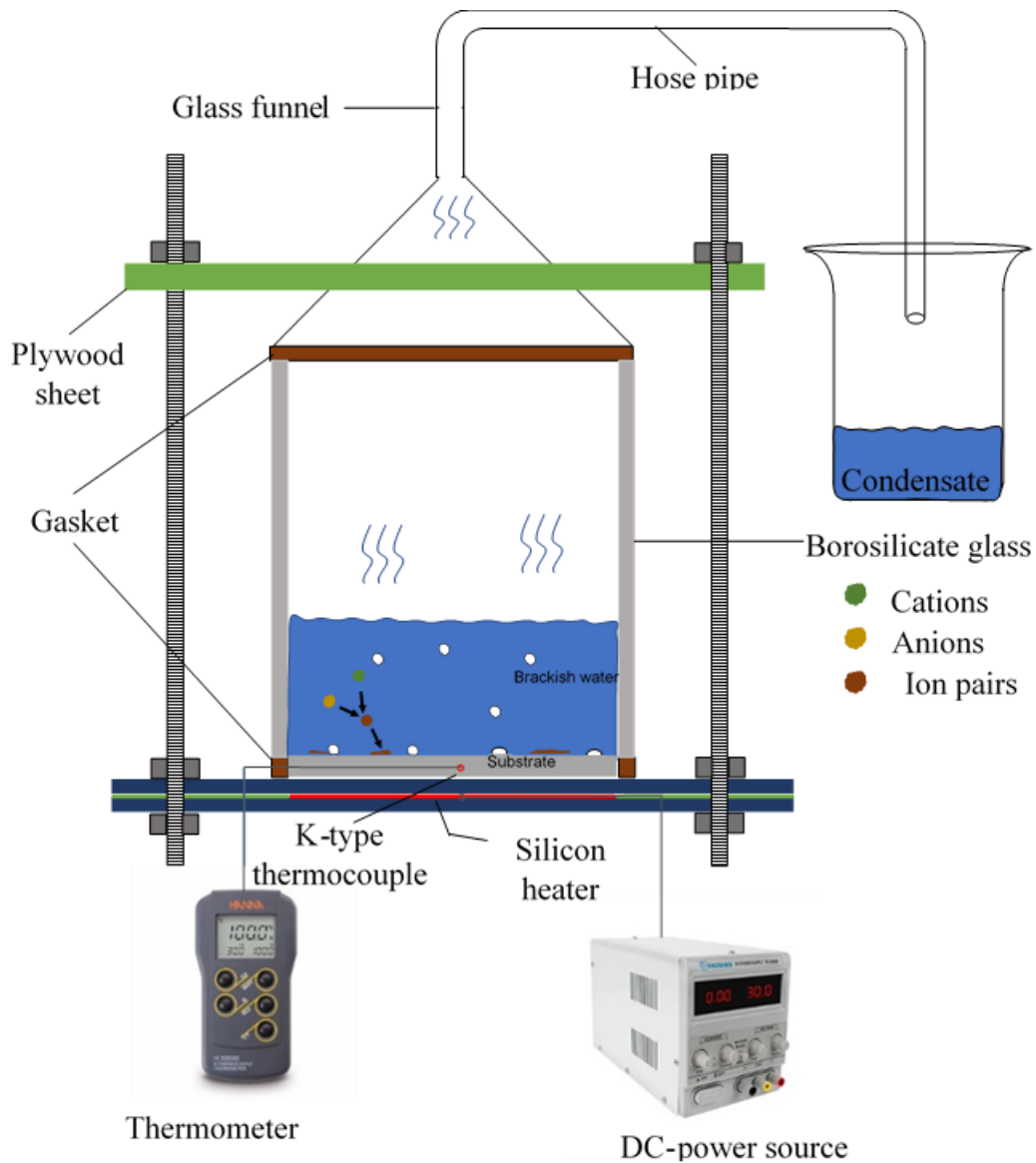


Figure 4.1 Laboratory scale setup to test the inorganic fouling effect on test surface.

4.3 CORROSION

The corrosion resistance of the PS, UOS, and BiS was analyzed in a simulated brackish water environment through electrochemical corrosion and immersion corrosion (weight loss method) tests.

4.3.1 ELECTROCHEMICAL CORROSION TEST

In the electrochemical tests both potentiodynamic polarization (PDP) and electrochemical impedance spectroscopy (EIS) were sequentially performed without changing samples on a computer controlled electrochemical work station (Gill AC, ACM instruments, UK) using a standard three electrode cell as shown in Fig 4.2. In this work, a platinum electrode and saturated calomel electrode were served as counter electrode and a reference electrode respectively, while the test sample acted as a working electrode. Simulated brackish water was used as electrolyte, and all the electrochemical experiments were conducted at room temperature. Before testing, the electrolyte was degassed by bubbling argon gas. The test sample was then immersed in the electrolyte for 1000 seconds and allowed to stabilize, while simultaneously recording the open circuit potential (OCP). A square test sample was employed, with all sides sealed using resin material, except for a 1cm² exposure area. In each test, the test sample was exposed identically.

In the PDP test, a potential of ± 250 mV (Vs OCP) was applied to the working electrode at a constant scanning speed of 5mV/sec throughout the test. The resulting currents were recorded, and the relationship between the applied potential and resultant current was plotted on a polarization curve. The corrosion potential (E_{corr}) and corrosion current density (I_{corr}) were determined from the polarization curve using the Tafel extrapolation method, and the corrosion rate was subsequently determined.

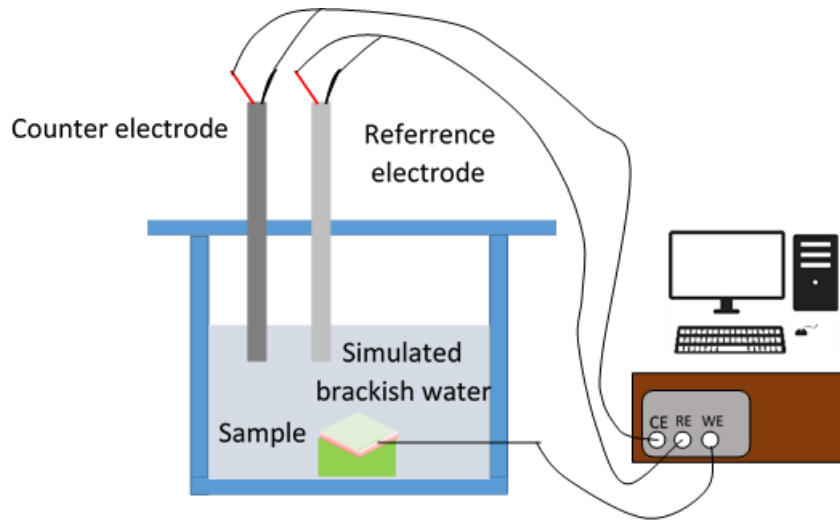


Figure 4.2 The schematic of electrochemical corrosion test rig.

For the EIS test, a small amplitude of 10 mV was applied to the working electrode across a frequency range of 100,000 Hz to 0.01 Hz at a scanning speed of 10 points per decade. Impedance components such as resistance (Z') and capacitance (Z'') were marked to create a Nyquist plot. After the electrochemical tests, the surface morphologies of the corroded test samples were observed under FESEM.

4.3.2 IMMERSION CORROSION TEST

Weight loss tests were conducted by immersing the test samples in simulated brackish water for 7 days at three different temperatures: room temperature (RT), 50 °C, and 75 °C. Before immersion, the initial weight of the samples was recorded using a digital weighing balance. After the designated time, the test samples were removed from the brackish water, cleaned in a suitable solution following ASTM G1 (G1 2003), rinsed in deionized water, dried, and reweighed. This process was repeated until no weight change was observed. The uniform corrosion rate (CR) was calculated using equation 4.1.

$$CR \text{ (mm/year)} = \frac{8.76 \cdot 10^4 \cdot W}{A \cdot t \cdot D} \quad (4.1)$$

Where, W represents the mass loss in grams, A is the surface area of the specimen exposed to corrosion in cm^2 , t is the duration of exposure in hours, and D is the specimen density in g/cm^3 . To ensure the reproducibility, all the experiments were conducted thrice and the CR values reported are the average values.

4.3 RESULTS AND DISCUSSION

4.3.1 MITIGATION OF INORGANIC SCALING

The experiments were carried out to investigate the fouling patterns on the test surfaces and to assess their ability to improve BHT to the working fluid in order to maximize condensate production. Typically, the BHT of saltwater is superior to that of plain water due to the additional nucleation sites provided by salt precipitation. However, during prolonged boiling periods, the precipitants can act as thermal resistance, diminishing boiling efficiency and raising surface temperatures (Raghupathi and Kandlikar 2017). Figure 4.3 illustrates the changes in condensate collected by each surface over time. It is evident from the figure that initially, the amount of condensate collected is similar for all test surfaces. This is because, in the early stages, the generated vapor circulates only in the upper half of the glass tube and condense on the walls of the glass tube, funnel, and hose pipe. However, when the concentration of vapor intensifies, they pass through the hose pipe and reach the condensate collecting flask. As time progresses, the slope of the BiS is steeper compared to other surfaces, indicating effective BHT to the brackish water on the BiS. As discussed earlier, this improved boiling performance can be attributed to liquid puddles on the BiS (Holguin et al. 2017), as they aid in augmented bubble activity (i.e., bubble incipience and departure) on the surface. In contrast, the omniphilic nature of the UOS substrate limits the number of active NSD but sustains bubble activity. On the other hand, bubble activity on the PS is restricted by the dominant surface tension between the working fluid and the surface, leading to decreased bubble departure rates and a surface crowded with bubbles.

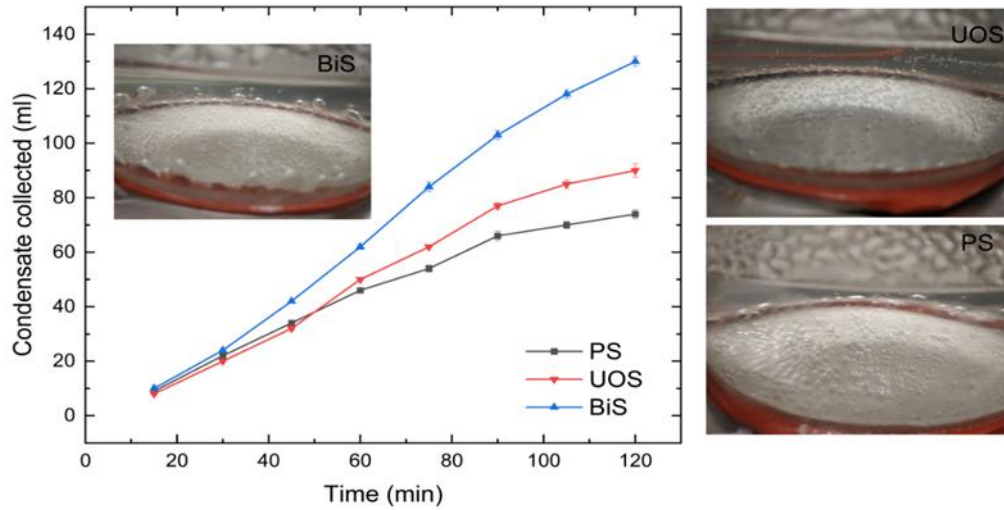


Figure 4.3 Variation of condensate collected with time on each test surface.

As a result of the continuous formation of bubbles, the extraction of pure water is enhanced, leading to higher concentration of salt in brackish water. This causes the supersaturated salt ions to be deposited onto the surface. However, the stability of these deposited salt ions is influenced by the surface conditions. The process of precipitation on PS and BiS is illustrated in Fig. 4.4. Microscopic crevices and cavities serve as potential SNS for the deposited salt ions. Once these SNS are stabilized, they further agglomerate salt ions and crystallize, and the precipitants grow in size. However, on BiS, a smooth and defect-free liquid-liquid interface limits the crystallization to the solid islands, reducing the availability of SNS and resulting in a slower crystallization rate (Bartman et al. 2011). Moreover, the adhesion of the precipitants on the BiS could be less due to the limited surface area of foulants in contact with the substrate (Visser 1995). These points are further supported by Fig 4.5, 4.6, 4.7, and 4.8.

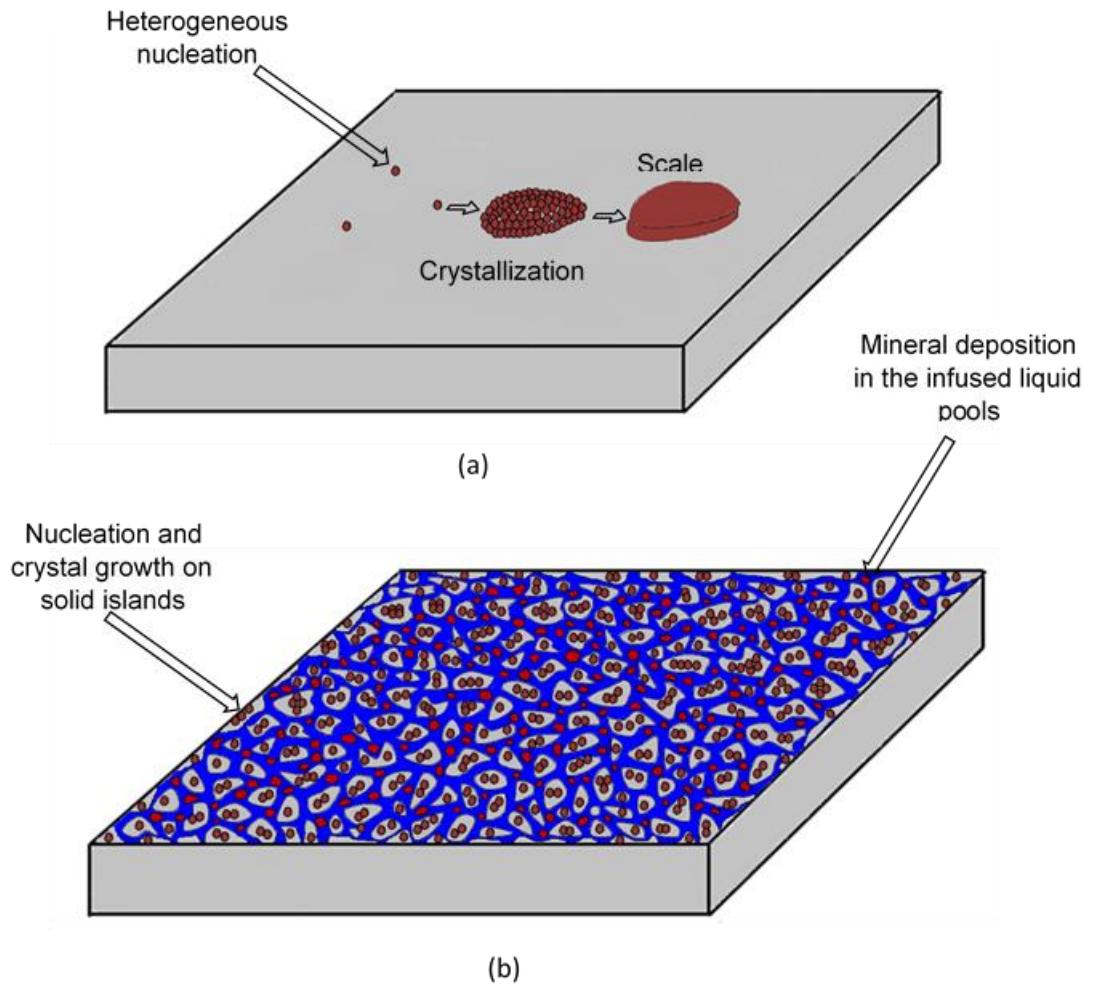


Figure 4.4 Depiction of precipitation mechanism on a) PS and b) BiS.

Figure 4.5 indicates the amount of condensate collected and the percentage of weight increase after boiling the brackish water on each substrate for two hours at a constant temperature of 115 °C. The continuous bubbling activity during the boiling process enhances the condensate, while mineral compounds that are supersaturated are deposited on the substrate. These deposited salt ions then transform into SNS at different locations on the substrate, leading to the stabilization, agglomeration, crystallization, and adhesion of the precipitates, as depicted in Fig 4.4. Based on the information presented in Fig 4.5, it can be deduced that the BiS substrate outperformed the PS and UOS substrates in terms of condensate collection, exhibiting approximately 73% and 44% higher condensate accumulation, respectively. This superior

performance can be attributed to the increased bubble activity on the BiS substrate facilitated by the presence of liquid puddles.

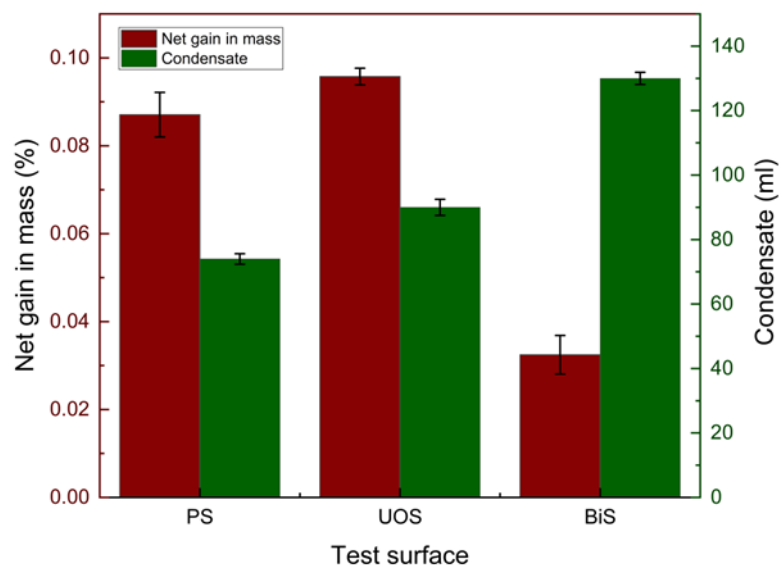


Figure 4.5 Variation of the net increase in the weight and condensate collected due to boiling of brackish water on each test surface.

Conversely, the UOS demonstrated the most significant weight gain, suggesting a stronger adhesion to mineral salts. The weight gain observed in the UOS exceeded that of the PS and BiS for various reasons. The omniphilic nature of the UOS attracts brackish water even at higher salt concentrations. Additionally, the inherent surface roughness of the UOS, stemming from micro and nanocavities, provides ideal conditions for salt ions to form SNS.

The deposited precipitates usually comprise sulfates and carbonates of calcium and magnesium, forming crystalline structures with uneven surfaces. As these deposits accumulate, they generate irregularities and raise the average surface roughness. Figure 4.6 displays the roughness profiles of fouled PS, UOS, and BiS, captured using an optical 3D profilometer. The average roughness (Ra) measured on the BiS surface after fouling is observed to be approximately 55% and 65% lower than that of the PS and UOS, respectively, indicating that the scale buildup on BiS is significantly less than on

the other two surfaces. The reduced scale buildup on BiS is attributed to its smooth and defect-free topography, which inhibits the nucleation and agglomeration of deposited precipitates. In contrast, the higher roughness observed on the fouled UOS results from potential SNS.

The fouling pattern on PS, UOS, and BiS was captured using FESEM and presented in Fig 4.7. Upon examination of PS and UOS, it is evident that the precipitates grow larger and spread across the entire surface, thereby reducing the available heat exchange area. Consequently, the lower condensation rates of PS and UOS can be attributed to the adhesion of these precipitates. In contrast, when looking at BiS, the crystallization is limited to the solid islands, and the salt ions deposited in the liquid puddles remain amorphous, do not adhere to the substrate, and do not contribute to the scale formation; as a result, the weight that BiS gains from fouling is the lowest among the three surfaces. Figure 4.8 represent the FESEM images captured after allowing the brackish water to boil on each test surface for five hours. The figure reveals that the PS and UOS substrates are filled with clusters and stacks of densely packed salts, which are absent on the BiS substrate. Hence, the crystallization of mineral depositions can be delayed on BiS, even when subjected to longer periods of exposure.

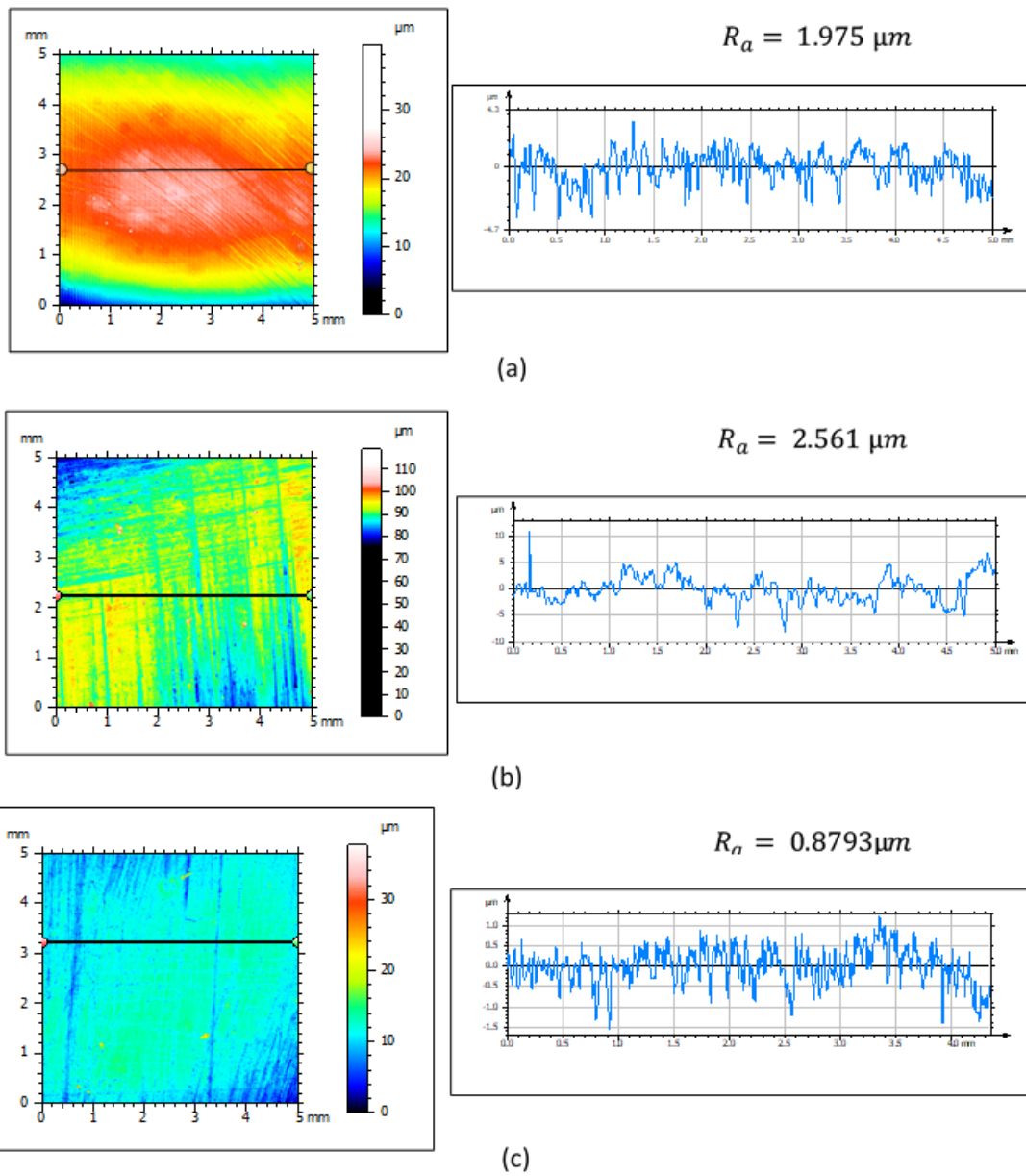
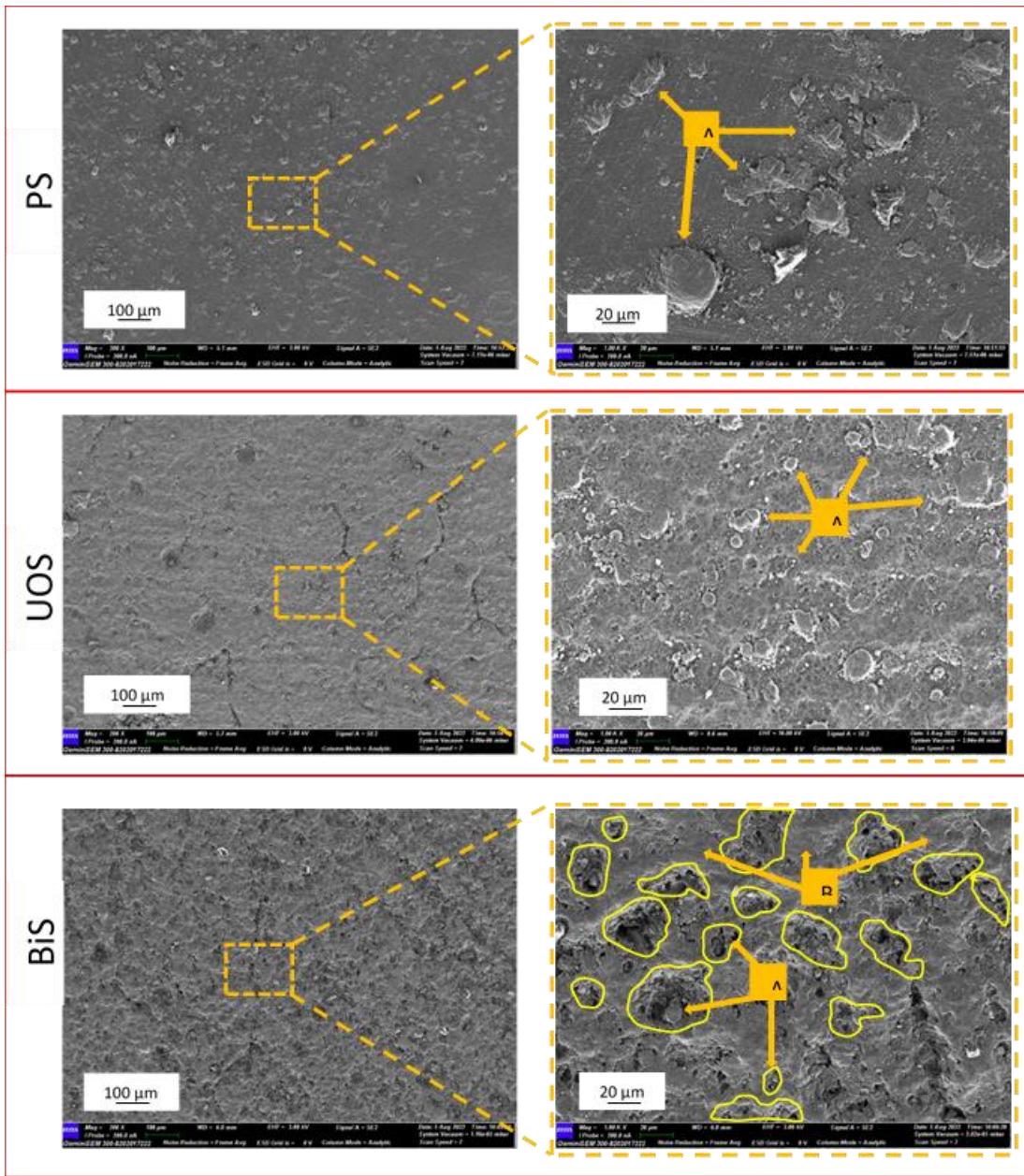


Figure 4.6 Average roughness profile of the fouled surfaces captured by 3 D Profilometer on a) PS b) UOS and c) BiS.



A: Agglomeration of salt ions into crystals B: Deposited salt ions remain

Figure 4.7 FESEM images of PS, UOS, and BiS at various magnifications captured after exposure to boiling.

In this context, the OCP of BiS (- 690 mV) is higher than the PS (- 731 mV), and UoS (- 733 mV), respectively. These values suggest that BiS is less prone to undergo electrochemical reactions, meaning less corrosion. This can be attributed to the well-distributed liquid puddle network on the surface of BiS.

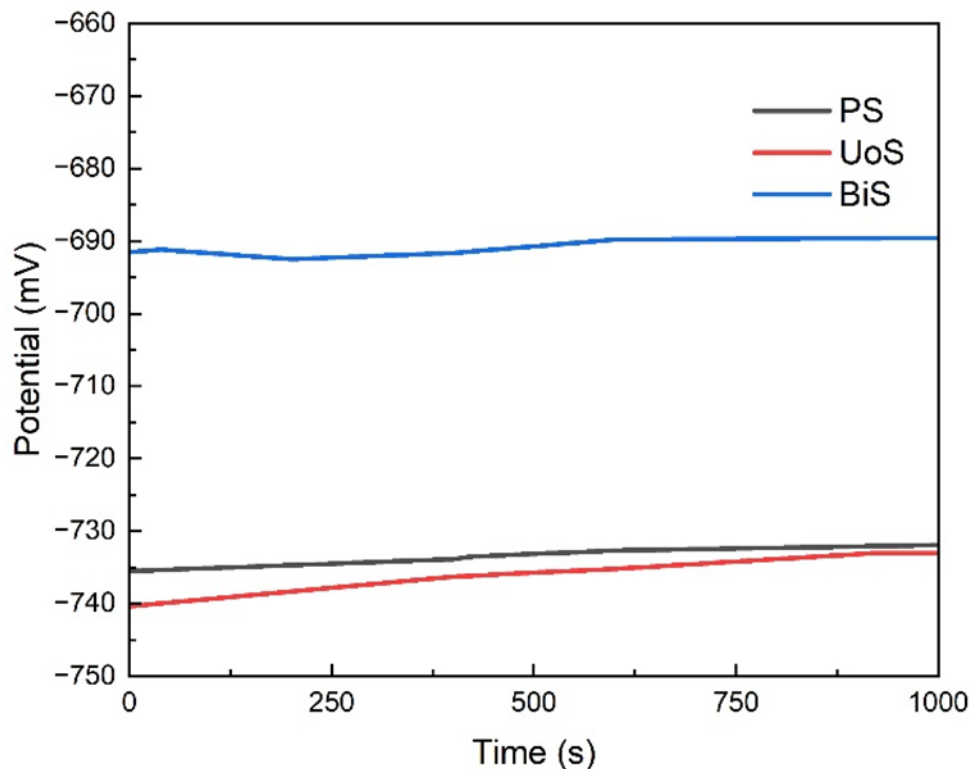


Figure 4.9 OCP curves of PS, UoS, and BiS.

The PDP curves of PS, UOS and BiS in simulated brackish water environment are shown in Fig 4.10. These curves illustrate the cathodic and anodic reactions of the specimen and provide insights of the active anodic dissolution. The corrosion current density (I_{corr}) and corrosion potential (E_{corr}) of the specimens were obtained from the PDP curves using a Tafel extrapolation method. Table 4.2 shows the E_{corr} , I_{corr} , and CR values of PS, UOS, and BiS respectively. The CR in millimetres per year (mm/yr) was calculated by equation 4.2, which is borrowed from (Charitha and Rao 2017).

$$CR \text{ (mm/year)} = \frac{3.27 \cdot M \cdot I_{corr}}{\rho \cdot z} \quad (4.2)$$

Here, M represents the atomic mass of the metal (27), ρ denotes the metal density in g/cm^3 (2.7), and z signifies the electrons transferred per atom (3). The CR values, as shown in the table 4.2, indicate that the metal degradation of BiS is relatively lower than that of the PS and UOS in a simulated brackish water environment.

Low I_{corr} and high E_{corr} values represent the higher corrosion resistance in the specimen (Rokkala et al. 2021; Tuo et al. 2017). The I_{corr} for the UoS (0.019007 mA/cm^2) was higher than that for PS (0.010792 mA/cm^2), suggesting that UOS has lower corrosion resistance compared to PS. This reduced corrosion resistance in the UOS can be attributed to its extreme wetting capabilities caused by numerous micro and nanocavities. This hydrophilic nature of the UOS enhances direct surface contact with Cl^- ions present in the brackish water, thus promoting the corrosion reaction. Compared to PS and UOS, the I_{corr} for the BiS (0.004230 mA/cm^2) was reduced by one order of magnitude. The decrease in the corrosion current density for the BiS was the result of the fact that the surface area in contact with the brackish water on BiS was substantially reduced by saturating the micro and nano cavities with liquid lubricant, thereby protecting the underlying metal from corrosion attack. As a result, BiS offers superior corrosion resistance in comparison to PS and UOS. Furthermore, E_{corr} for BiS (-641 mV) was also higher than that for PS (-737 mV), and UOS (-756 mV), reinforcing the same conclusion.

Table 4.2 Results of the PDP measurements in simulated brackish water.

Specimen	E_{corr} (mV)	I_{corr} (mA/cm^2)	CR (10^{-4} mm/yr)
PS	-736.612	0.010792	11.76
UOS	-756.401	0.019007	20.72
BiS	-641.457	0.004230	4.61

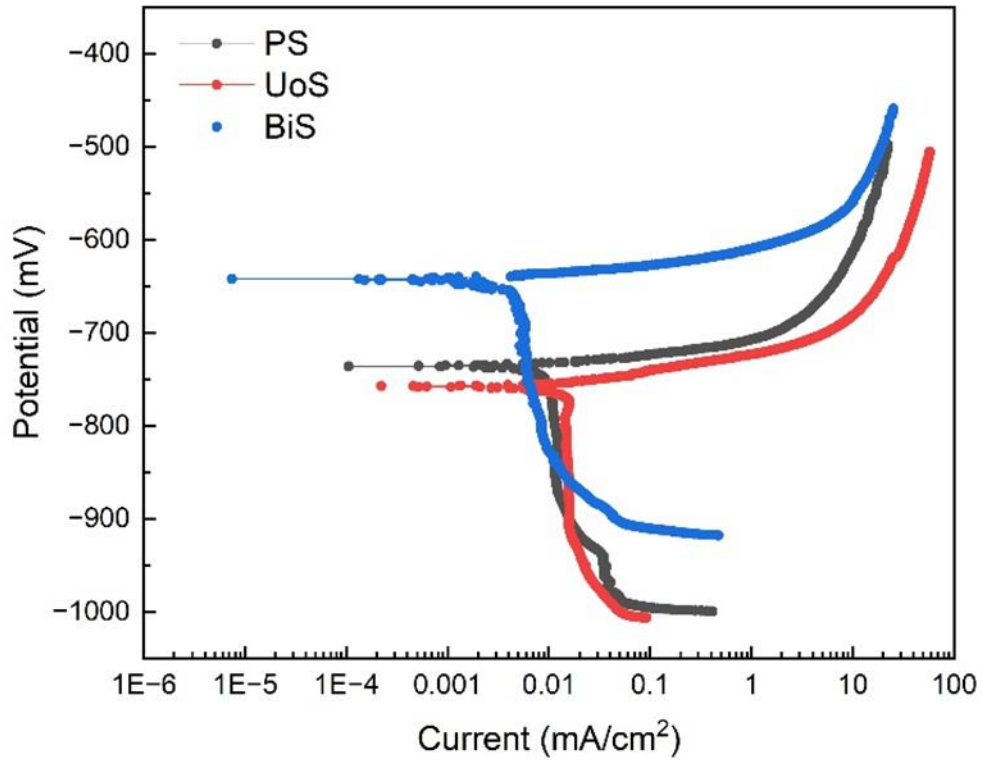


Figure 4.10 PDP curves of PS, UoS, and BiS.

To investigate the impedance behaviour of PS, UOS, and BiS in brackish water, Nyquist plots are presented in Fig 4.11. These Nyquist plots, depicting aluminum corrosion in a brackish water environment are in agreement with those reported by Rosliza et al. (2010). The figures reveal that the impedance values of the specimen form a semi-circular shape, indicating that charge transfer predominantly governs the corrosion process. The diameter of the impedance is directly proportional to corrosion resistance (Cai et al. 2022). Notably, BiS exhibits the largest semi-circular impedance diameter compared to PS and UOS, emphasising its superior corrosion resistance.

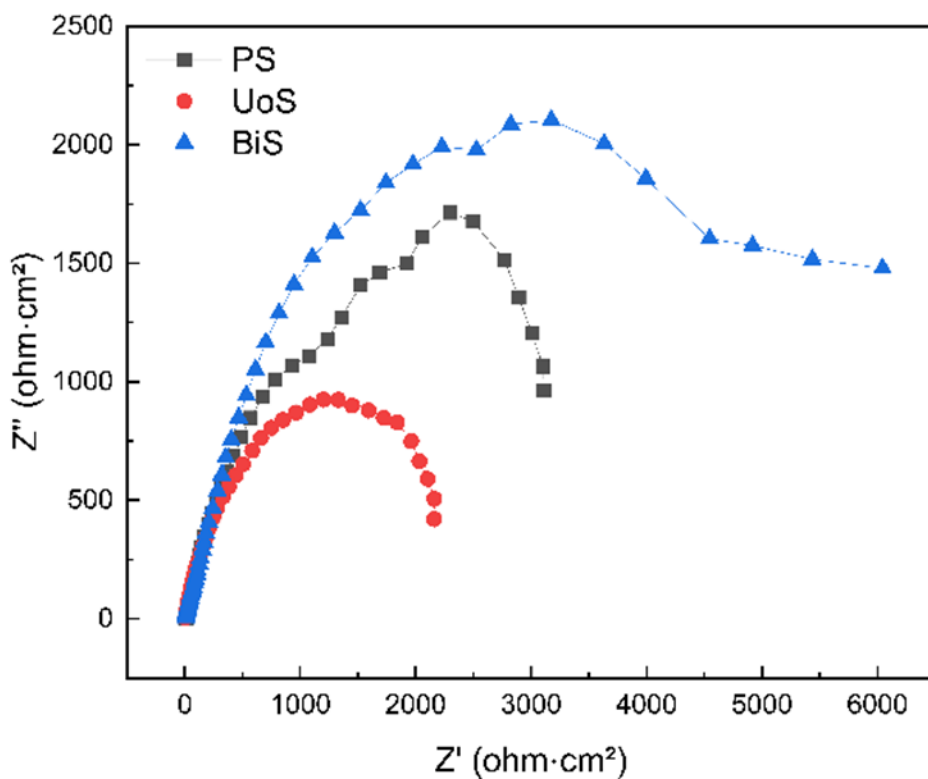


Figure 4.11 Nyquist plots of PS, UoS, and BiS.

The EIS experimental data were fitted to the equivalent Randle circuit using an EIS analyzer. The Randle circuit, depicted in Fig 4.12, is one of the simplest and most common circuit models for electrochemical impedance. The primary electrochemical parameters of the circuit include the solution resistance (R_s), connected in series with a parallel combination of charge transfer resistance (R_{ct}), and double electric layer capacitance (C_{dl}). The values of these parameters are listed in Table 4.3.

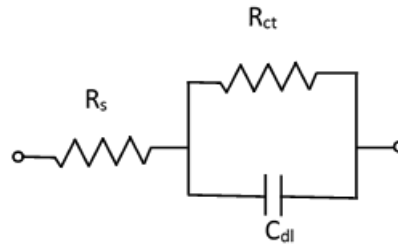


Figure 4.12 Equivalent Randle circuit.

Table 4.3 Fitting results of EIS data in simulated brackish water.

Specimen	R_s (Ohm·cm ²)	R_{ct} (Ohm·cm ²)	C_{dl} (F / cm ²)
PS	4.7393	4320.2	5.56E-05
UoS	4.0048	2397	5.96E-05
BiS	10.771	6657.5	4.69E-06

R_s represents the resistance to ion conductivity within the electrolyte solution, R_{ct} signifies the charge transfer resistance at the metal-electrolyte interface, and C_{dl} denotes the capacitance of the electrical double layer formed at the metal-electrolyte interface. Notably, Table 4.3 reveals that the R_s values are considerably lower compared to the values of R_{ct} , suggesting that R_s has a negligible effect on the corrosion rate.

In the case of BiS, there was an increase in R_{ct} value and a decrease in C_{dl} value when compared to PS and UOS, respectively. Generally, higher R_{ct} and lower C_{dl} values indicate better corrosion resistance of the specimen. The presence of lubricant puddles on the BiS effectively reduces the surface area in contact with the electrolyte, thereby increasing the charge transfer resistance and reducing the electrical double layer capacitance at the metal-electrolyte interface.

The FESEM micrographs of PS, UOS, and BiS after undergoing electrochemical corrosion testing in simulated brackish water are presented in Fig 4.13. Numerous corrosion voids or pits, ranging in size from 100 μm to 200 μm , are clearly visible on both PS and UOS. The surfaces of PS and UOS directly encounter Cl^- ions in the brackish water, initiating aggressive corrosion reactions that lead to pitting corrosion.

Further, it is also noticed that the pits on UOS are much larger and more severe, attributable to the additional surface area provided by the micro/nano cavities.

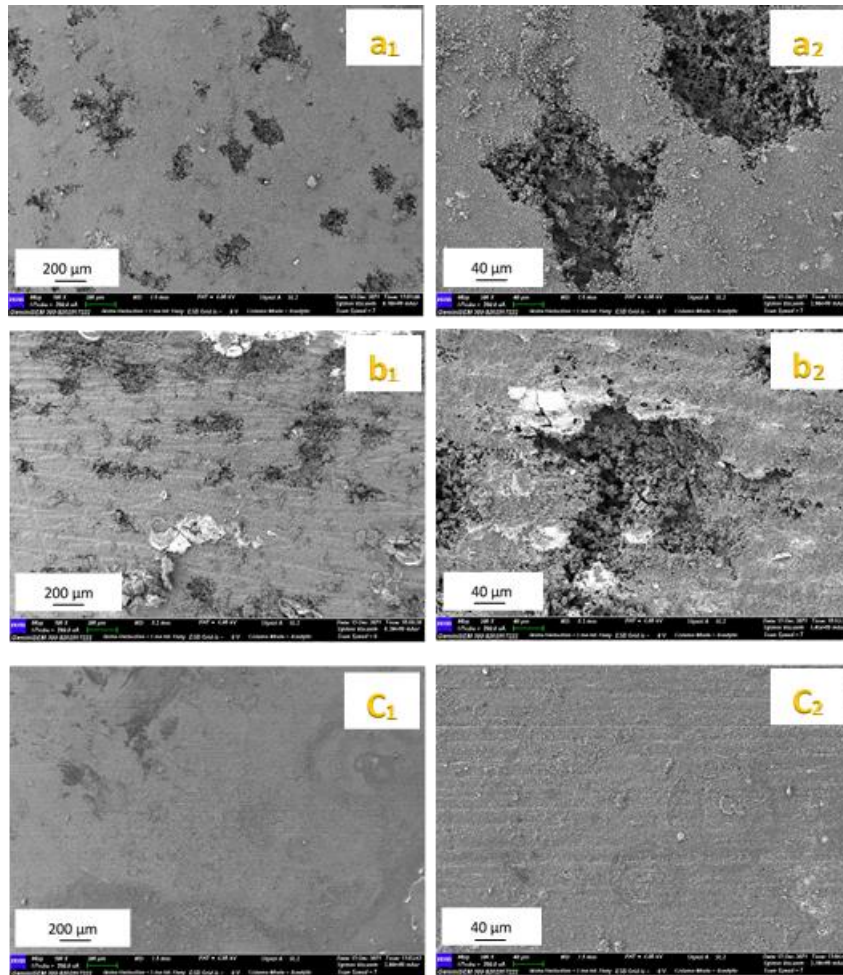


Figure 4.13 Surface morphology of (a) PS (b) UOS, and (c) BiS subjected to electrochemical corrosion.

In comparison to PS and UOS, the morphology of BiS appears less damaged, indicating that BiS offers good corrosion resistance against brackish water. This reduced susceptibility to corrosion is attributed to the partial coverage of BiS topography by lubricant puddles, limiting direct contact of the corrosion medium to solid islands and thereby reducing the extent of corrosion attack on BiS

4.3.2.2 Immersion corrosion

To comprehend the effect of temperature on metal degradation, immersion corrosion tests were performed at RT, 50 °C, and 75 °C; the corresponding results are shown in Fig 4.14. Brackish water, enriched with dissolved salts and ions, exhibits electrical conductivity. As temperature rises, the mobility of ions increases, intensifying the corrosion-inducing reactions. consequently, an upward trend in corrosion rate is observed on all surfaces as the temperature increases.

As depicted in the figure, the corrosion rate of BiS is consistently lower than that of PS and UoS at all respective temperatures. However, the corrosion rate of BiS experiences a significant increase of approximately 150% between RT and 75 °C, which is three times higher than the increase in corrosion rate observed for PS and UoS within the same temperature range. This observation suggests that the liquid lubricant begins to disperse as the temperature rises. This dispersion, in turn, reduces corrosion resistance capabilities of BiS in response to temperature variations.

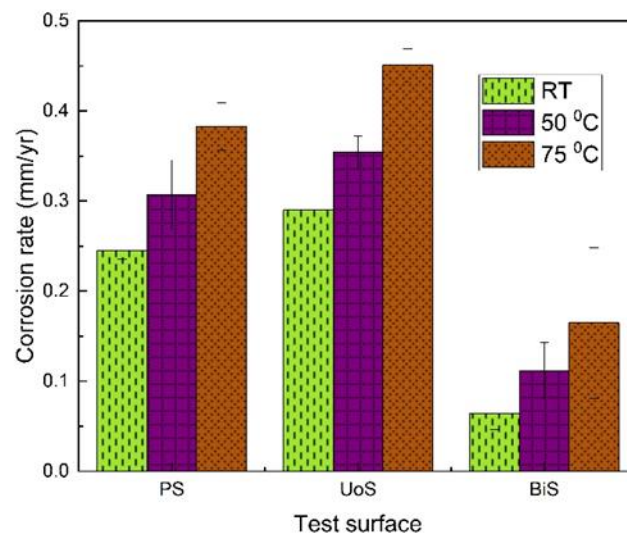


Figure 4.14 Corrosion rate of PS, UoS, and BiS at different temperatures obtained by weight loss method.

Further, to understand the kinetics and thermodynamics of corrosion process, parameters such as energy of activation (E_a), Enthalpy of activation (ΔH), and activation entropy (ΔS) were determined (Poornima et al. 2010). The E_a and ΔH share the similar significance, they both represent the energy barrier that must be overcome for a chemical reaction to occur. Therefore, higher E_a or ΔH indicates a slower corrosion rate. On the other hand, ΔS reflects the change in entropy associated with the transition state of a chemical reaction. A positive ΔS indicates that the transition state (activated complex) of the reaction has greater disorder than the reactants, making it easier for reactants to transform into corrosion products.

Figure 4.15 represents the $\ln(\text{CR})$ Vs $1/T$ plots for PS, UOS and BiS. These plots are graphical representation of Arrhenius law equation (equation 4.3). The curves of these plots yield collinear lines, and their slopes are equal to $-E_a/R$, from which E_a values of PS, UOS and BiS were obtained. Similarly, ΔH and ΔS values of PS, UOS and BiS are obtained by plotting $\ln(\text{CR}/T)$ values against $(1/T)$ as shown in Fig 4.16. These plots are the graphical representation of transition state equation (equation 4.4). The curves of these plots are collinear, whose slope is equal to $-\Delta H/RT$ and intercept is equal to $\ln(R/Nh) + \Delta S/R$.

$$\ln(\text{CR}) = B - \frac{E_a}{RT} \quad (4.3)$$

$$\text{CR} = \frac{RT}{Nh} \exp\left(\frac{\Delta S}{R}\right) + \exp\left(\frac{-\Delta H}{RT}\right) \quad (4.4)$$

Where B refers to the Arrhenius constant, T is the absolute temperature, R denotes the universal gas constant (8.314 J/mole·K), h is the planks constant (6.626×10^{-34} J·S), and N represents the Avogadro's number (6.023×10^{23} /mole). The obtained E_a , ΔH , and ΔS values are listed in Table 4.4.

Table 4.4 Activation parameters of PS UOS and BiS in simulated brackish water.

Specimen	E_a (kJ/mole)	ΔH (kJ/mole)	ΔS (J/mole · K)
PS	8.29	5.6	-158
UOS	8.18	5.49	-157
BiS	17.4	14.71	-176

From table 4.4, it can be noticed that E_a and ΔH values of BiS are much higher compared to those of PS, and UOS. This observation suggests that BiS hinders the charge transfer process during the corrosion reaction, which can be attributed to the presence of lubricant puddles on the BiS surface, which separates the substrate from the corrosion medium. In case of ΔS , all specimens exhibit negative values, indicating that the transition state of the corrosion reaction involves association rather than dissociation. However, the ΔS of BiS is more negative compared to PS and UOS. This greater negativity suggests a reduction in disorderliness and consequently a slower corrosion reaction when BiS is involved.

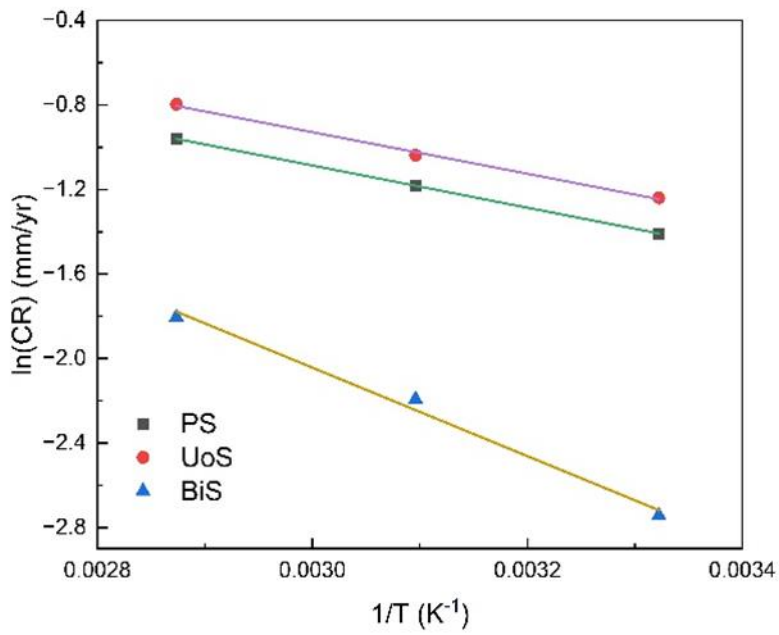


Figure 4.15 ln (CR) Vs 1/T plots of PS, UOS, and BiS.

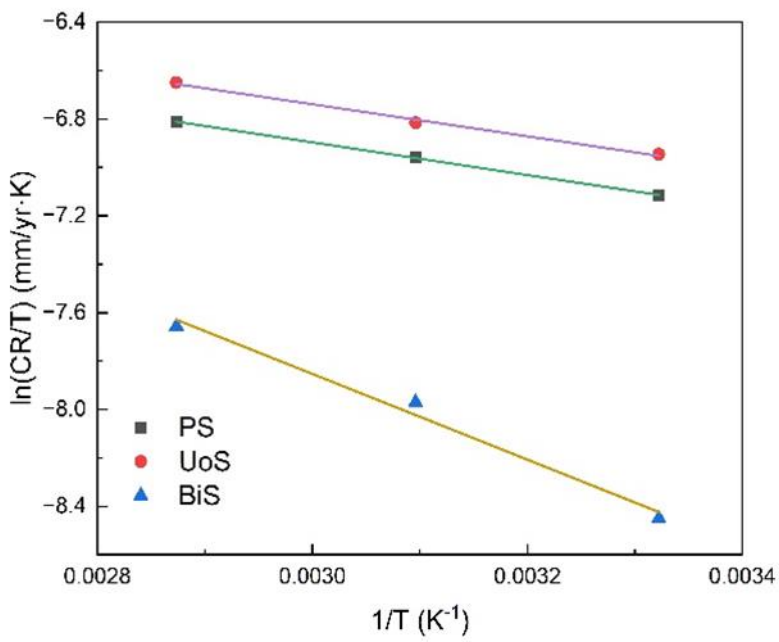


Figure 4.16 ln (CR/T) Vs 1/T plots of PS, UOS, and BiS.

CHAPTER 5

CONCLUSIONS AND FUTURE SCOPE

5.1 CONCLUSIVE REMARKS

In the present work, it was demonstrated that a surface partially covered with a liquid has the potential for enhancing BHT, mitigating inorganic fouling and corrosion. The liquid-infused surface called Binary surface or BiS has two distinct phases – solid phase as islands and liquid phase as liquid lubricant puddles. Boiling experiments were conducted at atmospheric pressure using DI water while inorganic scaling and corrosion tests were conducted in a simulated brackish water environment, on a PS (plain or polished surface), an UOS (ultra-omniphilic surface, which has extreme wetting properties to multiple liquids), and a BiS, all made of Al 6061-T6 alloy. The BiS was found to exhibit enhanced BHT, excellent resistance to corrosion and mineral deposition among all the tested surfaces. The key findings of this study are as follows.

1. The wall superheat required for the onset of nucleate boiling on the BiS was ~ 7 °C, which is approximately 35% lower than on the PS and 40.5% lower than on the UOS. The low wall superheat value for onset of boiling ascertains heterogeneous boiling on the BiS.
2. The CHF obtained on the BiS was 40% higher than on the PS, which is attributed to the presence of the liquid lubricant puddles on BiS. After analysing the high-speed videos and the major difference between BiS and the other two surfaces (which is the presence of lubricant on BiS), it is concluded that the lubricant puddles provide for easy and separate parallel pathways for liquid rewetting and vapor bubble removal in addition to denying the lateral bubble merger by preventing the growth of bubbles. These phenomena collectively extend the discrete bubble regime on the BiS resulting in an enhanced heat flux dissipation capacity. The CHF values recorded on both the BiS and the UOS were identical despite the large difference in the actual area available for boiling over them (due to liquid lubricant occupying a considerable area on the BiS).

3. The D_d values on the BiS were smaller than those on the PS and the UOS. Also, the departure frequency rate of the bubbles was higher on the BiS compared to the other two surfaces which ensured a larger $f \cdot D_d$ values for the BiS implying enhancement in BHT. This enhanced boiling effect was also confirmed by calculating the Ja on the BiS which were lower than those on the PS and the UOS.
4. The HTC on the BiS was approximately 100% and 35% higher compared to the corresponding values on the PS and UOS, respectively. This augmentation in the HTC is attributed to a low bubble incipience temperature, smaller D_d , higher $f \cdot D_d$, and improved convection which expands the span of nucleate pool boiling regime on the BiS.
5. Active NSD on the BiS is higher than on the PS and UOS, which is attributed to a higher wall superheat locally on the solid islands than on the adjacent liquid lubricant puddles of the BiS.
6. A comparison of the results between UOS and BiS suggests that, as far as boiling enhancement is concerned, mechanisms for tackling vapor bubbles (e.g., BiS) could be superior to those that involve improving surface wettability (i.e., UOS or highly wetting/hydrophilic surfaces).
7. The BiS demonstrated a low weight gain and a high condensate collection compared to the PS and UOS. This excellent performance of the BiS was attributed to the liquid puddles on BiS, which serve two purposes: (i) acting as a barrier to prevent the stabilization and agglomeration of deposited minerals, and (ii) enhanced the bubble activity and contributed to higher condensate formation.
8. The FESEM micrographs of fouled surfaces revealed that deposited precipitants grew larger and distributed across the entire surface on the PS and UOS, while on the BiS, precipitation was limited to solid islands. This phenomenon is due to incipience of SNS only on solid islands, as the smooth and defect-free liquid puddles inhibit SNS. This result was further confirmed by measuring the average roughness of the fouled surfaces using a 3D profilometer. The average roughness of the fouled BiS due to scale build up was $0.8793 \mu\text{m}$ (Ra), approximately 55% and 65% lower than that of the PS and UOS, respectively.

9. Potentiodynamic polarization curves reveal that the BiS exhibited lower corrosion current density (I_{corr}) and higher corrosion potential (E_{corr}) compared to those of the PS and UOS in a simulated brackish water environment. The liquid puddles on the BiS protect the metal beneath from the corrosion attack, resulting in lower I_{corr} and higher E_{corr} values.
10. Electrochemical impedance spectroscopy tests showed that the BiS exhibited higher charge transfer resistance (R_{ct}) and lower double layer capacitance (C_{dl}) at the metal-electrolyte interface compared to the PS and UOS. This is attributed to the smaller surface area in direct contact with Cl^- ions in the simulated brackish water for the BiS, increasing resistance and reducing the capacity for charge transfer.
11. FESEM images of the corroded surfaces reveal that BiS appears less damaged compared to PS and UOS, which experience a severe corrosion attack. The poor corrosion resistance of the PS and UOS was attributed to their larger surface areas in direct contact to the Cl^- ions, intensifying the corrosion reaction.
12. Immersion corrosion tests conducted on PS, UOS, and BiS at RT, 50 °C, and 75 °C. The BiS achieved lower corrosion rates and outperformed PS and UOS at all the tested temperatures. However, the corrosion rate of the BiS experienced a significant increase of approximately 150% between RT and 75 °C due to the dispersion of liquid lubricant at higher temperatures.
13. The analysis of chemical reaction kinetics reveals that corrosion reactions on the BiS occurred at much slower rate than on the PS and UOS. The BiS exhibited higher activation energy (E_a) and lower activation entropy (ΔS). The liquid puddles on the BiS creates a barrier between the metal and corrosion medium, leading to a higher activation energy for a corrosion reaction.

5.2 FUTURE SCOPE

Since BiS fabrication involves thermo-catalytic etching, there is potential for exploring controlled etching to regulate the locations and overall area covered by lubricant puddles. This approach could further enhance BHT on BiS.

Additionally, there is scope for developing analytical models that relate various aspects of the BiS, such as surface tension and thermal conductivity of the liquid lubricant, with BHT parameters like HTC, CHF, D_d , f , and active NSD. These models can aid in creating codes to computationally explore further enhancements in boiling heat transfer on BiS.

Despite the excellent scale inhibition and corrosion resistance offered by the BiS, further testing is required to assess its practical applications, such as in multi-stage flash desalination or solar stills. Real-world applications will determine the feasibility of the BiS. For instance, its reaction to actual brackish water containing various fouling agents, including bio-foulants, particulates, organic matter, and commercial desalination plant antiscalants, needs to be evaluated to understand its scaling mitigation and corrosion resistance capabilities.

5.3 CONTRIBUTION OF THE PRESENT WORK TO THE UNITED NATIONS SUSTAINABLE DEVELOPMENT GOAL

Conventional solar stills, although useful for decentralized freshwater production, typically require between 600–800 kWh/m³ to produce potable water. This energy demand often increases due to fouling and corrosion of the metal surfaces in contact with seawater. These issues not only elevate operational costs but also reduce the sustainability of solar stills, making them less viable as a solution to water scarcity in many parts of the world.

The current research addresses this challenge by demonstrating that BiS can mitigate corrosion and inorganic scaling, key factors that raise energy consumption. This mitigation effect of BiS translates into a notable reduction in maintenance needs and prolongs the longevity of the system, ensuring more consistent and efficient operation.

Moreover, the current investigation also shows that BiS surfaces achieve approximately 73% higher condensate accumulation than bare surfaces, significantly improving the yield of fresh water per unit of energy consumed.

By reducing the energy footprint and enhancing fresh water production, this study supports United Nations Sustainable Development Goal 6 by promoting a more cost-effective and resource-efficient approach to solar desalination. In areas with limited access to affordable drinking water, replacing plain solar-still basin with BiS could make solar stills a more feasible solution, contributing to the broader vision of sustainable, affordable, and accessible drinking water for all.

REFERENCES

- Aktinol, E., and Dhir, V. K. (2012). "Numerical simulation of nucleate boiling phenomenon coupled with thermal response of the solid." *Microgravity Sci. Technol.*, 24(4), 255–265.
- Al-Abri, M., Al-Ghafri, B., Bora, T., Dobretsov, S., Dutta, J., Castelletto, S., Rosa, L., and Boretti, A. (2019). "Chlorination disadvantages and alternative routes for biofouling control in reverse osmosis desalination." *npj Clean Water*, 2(1), 2.
- Al-Harashseh, M., Abu-Arabi, M., Ahmad, M., and Mousa, H. (2022). "Self-powered solar desalination using solar still enhanced by external solar collector and phase change material." *Appl. Therm. Eng.*, 206(January), 118118.
- Al-hotmani, O. M. A., Al-Obaidi, M. A., John, Y. M., Patel, R., Manenti, F., and Mujtaba, I. M. (2021). "Minimisation of energy consumption via optimisation of a simple hybrid system of multi effect distillation and permeate reprocessing reverse osmosis processes for seawater desalination." *Comput. Chem. Eng.*, 148, 107261.
- Al-Mutairi, N. N., Aleem, F. A., and Al-Ahmad, M. I. (2009). "Effect of antiscalants for inhibition of calcium sulfate deposition in thermal desalination systems." *Desalin. Water Treat.*, 10(1–3), 39–46.
- Allred, T. P., Weibel, J. A., and Garimella, S. V. (2018). "Enabling Highly Effective Boiling from Superhydrophobic Surfaces." *Phys. Rev. Lett.*, 120(17), 174501.
- Almuhanna, E. A. (2013). "Evaluation of Single Slope Solar Still Integrated With Evaporative Cooling System for Brackish Water Desalination." *J. Agric. Sci.*, 6(1).
- Amjad, Z., and Demadis, K. (2015). *Mineral Scales and Deposits*. Elsevier.
- Ansari, F. A., Verma, C., Siddiqui, Y. S., Ebenso, E. E., and Quraishi, M. A. (2018). "Volatile corrosion inhibitors for ferrous and non-ferrous metals and alloys: A review." *Int. J. Corros. Scale Inhib.*, 7(2), 126–150.
- Arunkumar, T., Denkenberger, D., Ahsan, A., and Jayaprakash, R. (2013). "The augmentation of distillate yield by using concentrator coupled solar still with phase change material." *Desalination*, 314, 189–192.

- Ayoub, G. M., Korban, L., Al-Hindi, M., and Zayyat, R. (2019). "Brackish Water Desalination: An Effective Pretreatment Process for Reverse Osmosis Systems." *Water. Air. Soil Pollut.*, 230(10).
- Bartman, A. R., Lyster, E., Rallo, R., Christofides, P. D., and Cohen, Y. (2011). "Mineral scale monitoring for reverse osmosis desalination via real-time membrane surface image analysis." *Desalination*, 273(1), 64–71.
- Betz, A. R., Jenkins, J., Kim, C. J., and Attinger, D. (2013). "Boiling heat transfer on superhydrophilic, superhydrophobic, and superbiphilic surfaces." *Int. J. Heat Mass Transf.*, 57(2), 733–741.
- Betz, A. R., Xu, J., Qiu, H., and Attinger, D. (2010). "Do surfaces with mixed hydrophilic and hydrophobic areas enhance pool boiling?" *Appl. Phys. Lett.*, 97(14), 2012–2015.
- Buros, O. K. (2000). "The ABCs of desalting". *Int. Desalin. Assoc.*, International Desalination Association.
- Cai, J., Gong, Z., and Tan, B. (2023). "Experimental and theoretical investigation of bubble dynamics on vertical surfaces with different wettability for pool boiling." *Int. J. Therm. Sci.*, 184(September 2022), 107966.
- Cai, Q., Xu, J., Lian, Z., Yu, Z., Yu, H., Yang, S., and Li, J. (2022). "Laser-Induced Slippery Liquid-Infused Surfaces with Anticorrosion and Wear Resistance Properties on Aluminum Alloy Substrates." *ACS Omega*, 7(32), 28160–28172.
- Chang, Y. H., and Ferng, Y. M. (2019). "Experimental investigation on bubble dynamics and boiling heat transfer for saturated pool boiling and comparison data with previous works." *Appl. Therm. Eng.*, 154(November 2018), 284–293.
- Charitha, B. P., and Rao, P. (2017). "Electrochemical and adsorption studies for the corrosion control of 6061 Al alloy using eco-friendly inhibitor." *Surf. Eng. Appl. Electrochem.*, 53(6), 551–559.
- Charpentier, T. V. J., Neville, A., Baudin, S., Smith, M. J., Euvrard, M., Bell, A., Wang, C., and Barker, R. (2015). "Liquid infused porous surfaces for mineral fouling mitigation." *J. Colloid Interface Sci.*, 444, 81–86.

- Chen, G., Jia, M., Zhang, S., Tang, Y., and Wan, Z. (2020). "Pool boiling enhancement of novel interconnected microchannels with reentrant cavities for high-power electronics cooling." *Int. J. Heat Mass Transf.*, 156.
- Chen, H. X., Sun, Y., Huang, L. Bin, and Wang, X. D. (2018). "Nucleation and sliding growth of boiling bubbles on locally heated silicon surfaces." *Appl. Therm. Eng.*, 143, 1068–1078.
- Cheong, W., Gaskell, P., and Neville, A. (2013). "Substrate effect on surface adhesion/crystallisation of calcium carbonate." *J. Cryst. Growth*, 363, 7–21.
- Chevalier, N. R. (2014). "Do Surface Wetting Properties Affect Calcium Carbonate Heterogeneous Nucleation and Adhesion?" *J. Phys. Chem. C*, 118(31), 17600–17607.
- Choi, C. H., David, M., Gao, Z., Chang, A., Allen, M., Wang, H., and Chang, C. H. (2016). "Large-scale Generation of Patterned Bubble Arrays on Printed Bi-functional Boiling Surfaces." *Sci. Rep.*, 6(April), 1–10.
- Choong, W. S., Ho, Z. Y., and Bahar, R. (2020). "Solar Desalination Using Fresnel Lens as Concentrated Solar Power Device: An Experimental Study in Tropical Climate." *Front. Energy Res.*, 8(October), 1–8.
- Cole, R. (1967). "Bubble frequencies and departure volumes at subatmospheric pressures." *AIChE J.*, 13(4), 779–783.
- Cvijovic, L., and Kota, K. (2018). "Creating highly wettable paper towel-like aluminum surfaces through tuned bulk micro-manufacturing." *Int. J. Adv. Manuf. Technol.*, 98(9–12), 2601–2609.
- Cvijovic, L., Sivakumar, P., Kuravi, S., Chaitanya, V., Teague, J., Ross, S., and Kota, K. (2022). "Infused Liquid Selection Criteria for Achieving Boiling Enhancements on Liquid-Infused Surfaces." *J. Thermophys. Heat Transf.*, 36(3), 784–788.
- Derjaguin, B. V. (1954). "A theory of the heterocoagulation, interaction and adhesion of dissimilar particles in solutions of electrolytes." *Discuss. Faraday Soc.*, 18, 85.
- El-Sebaey, M. S., Ellman, A., Hegazy, A., and Panchal, H. (2022). "Experimental study and mathematical model development for the effect of water depth on water production of a modified basin solar still." *Case Stud. Therm. Eng.*, 33(January), 101925.

- Elango, T., and Kalidasa Murugavel, K. (2015). "The effect of the water depth on the productivity for single and double basin double slope glass solar stills." *Desalination*, 359, 82–91.
- Elkholly, A., and Kempers, R. (2020). "Enhancement of pool boiling heat transfer using 3D-printed polymer fixtures." *Exp. Therm. Fluid Sci.*, 114(October 2019), 110056.
- Faegh, M., and Shafii, M. B. (2017). "Experimental investigation of a solar still equipped with an external heat storage system using phase change materials and heat pipes." *Desalination*, 409, 128–135.
- Friz, W. (1935). "Maximum volume of vapor bubbles." *Physic. Zeitschz.*, 36, 379–354.
- Gaertner, R. F. (1965). "Photographic study of nucleate pool boiling on a horizontal surface." *J. Heat Transfer*, 87(1), 17–27.
- Gates, G. L., and Caraway, W. H. (1967). *Deposition of barium sulfate from sea water in oil-well rotary pumps*. US Department of the Interior, Bureau of Mines ER -.
- Gerardi, C., Buongiorno, J., Hu, L. wen, and McKrell, T. (2010). "Study of bubble growth in water pool boiling through synchronized, infrared thermometry and high-speed video." *Int. J. Heat Mass Transf.*, 53(19–20), 4185–4192.
- Ghaffour, N., Missimer, T. M., and Amy, G. L. (2013). "Technical review and evaluation of the economics of water desalination: Current and future challenges for better water supply sustainability." *Desalination*, 309, 197–207.
- Gl, A. (2003). "Standard practice for preparing, cleaning, and evaluation corrosion test specimens." *ASTM Int. lggg*.
- Godinez, J. C., Fadda, D., Lee, J., and You, S. M. (2019). "Enhancement of pool boiling heat transfer in water on aluminum surface with high temperature conductive microporous coating." *Int. J. Heat Mass Transf.*, 132, 772–781.
- Goel, P., Nayak, A. K., Kulkarni, P. P., and Joshi, J. B. (2017). "Experimental study on bubble departure characteristics in subcooled nucleate pool boiling." *Int. J. Multiph. Flow*, 89, 163–176.
- Griffith, A. A. (1921). "VI. The phenomena of rupture and flow in solids." *Philos. Trans. R. Soc. London. Ser. A, Contain. Pap. a Math. or Phys. Character*, 221(582–

593), 163–198.

Hemkemeier, T. A., Almeida, F. C. R., Sales, A., and Klemm, A. J. (2022). “Corrosion monitoring by open circuit potential in steel reinforcements embedded in cementitious composites with industrial wastes.” *Case Stud. Constr. Mater.*, 16, e01042.

Holguin, R., Kota, K., Wootton, S., Chen, R. H., and Ross, S. (2017). “Enhanced boiling heat transfer on binary surfaces.” *Int. J. Heat Mass Transf.*, 114, 1105–1113.

Hong, M., Mo, D., and Heng, Y. (2024). “Bubble dynamics analysis of pool boiling heat transfer with honeycomb micro-nano porous structured surfaces.” *Int. Commun. Heat Mass Transf.*, 152(January), 107256.

Huang, J., Zheng, H., and Kong, H. (2024). “Key pathways for efficient solar thermal desalination.” *Energy Convers. Manag.*, 299(November 2023), 117806.

Izadi, M., Aidun, D. K., Marzocca, P., and Lee, H. (2010). “Effect of surface roughness on fouling of calcium carbonate: An experimental investigation.” *ASME Int. Mech. Eng. Congr. Expo. Proc.*, 7(PARTS A AND B), 869–876.

Jaikumar, A., Emery, T. S., and Kandlikar, S. G. (2018). “Interplay between developing flow length and bubble departure diameter during macroconvection enhanced pool boiling.” *Appl. Phys. Lett.*, 112(7).

Jakob, M., and Fritz, W. (1931). “Versuche über den verdampfungsvorgang.” *Forsch. auf dem Gebiet des Ingenieurwesens A*, 2(12), 435–447.

Jani, H. K., and Modi, K. V. (2018). “A review on numerous means of enhancing heat transfer rate in solar-thermal based desalination devices.” *Renew. Sustain. Energy Rev.*, 93, 302–317.

Jaswal, R., Sathyabhama, A., Singh, K., and Yandapalli, A. V. V. R. P. (2023). “Experimental and numerical investigation of pool boiling heat transfer from finned surfaces.” *Appl. Therm. Eng.*, 233, 121167.

Jiang, H., Xu, N., Wang, D., Yu, X., and Chu, H. (2021). “Experimental investigation of the effect of cylindrical array structure on heat transfer performance during nucleate boiling.” *Int. J. Heat Mass Transf.*, 174, 121319.

Jiang, S., Li, Y., and Ladewig, B. P. (2017). “A review of reverse osmosis membrane

fouling and control strategies.” *Sci. Total Environ.*, 595, 567–583.

Jo, H., Ahn, H. S., Kang, S., and Kim, M. H. (2011). “A study of nucleate boiling heat transfer on hydrophilic, hydrophobic and heterogeneous wetting surfaces.” *Int. J. Heat Mass Transf.*, 54(25–26), 5643–5652.

Jones, E., Qadir, M., Vliet, M. T. H. van, Smakhtin, V., and Kang, S. mu. (2019). “The state of desalination and brine production: A global outlook.” *Sci. Total Environ.*, 657, 1343–1356.

Jun, S., Kim, J., Son, D., Kim, H. Y., and You, S. M. (2016). “Enhancement of Pool Boiling Heat Transfer in Water Using Sintered Copper Microporous Coatings.” *Nucl. Eng. Technol.*, 48(4), 932–940.

Khechekhouche, A., Manokar, A. M., Sathyamurthy, R., Essa, F. A., Sadeghzadeh, M., and Issakhov, A. (2021). “Energy, Exergy Analysis, and Optimizations of Collector Cover Thickness of a Solar Still in El Oued Climate, Algeria.” *Int. J. Photoenergy*, 2021.

Kocamustafaogullari, G., and Ishii, M. (1983). “Aire interfaciale et densite de sites de nucleation dans les systemes en ebullition.” *Int. J. Heat Mass Transf.*, 26(9), 1377–1387.

Kumar, A., Kangude, P., and Srivastava, A. (2023). “Coupled bubble dynamics and interaction mechanisms of adjacently nucleated vapor bubbles under subcooled pool boiling regime.” *Phys. Fluids*, 35(8), 1070–6631.

Lemmert, M., and Chawla, J. (1977). “Influence of flow velocity on surface boiling heat transfer coefficient.” *Heat Transf. Boil.*, 237–247.

Lim, D. Y., and Bang, I. C. (2020). “Controlled bubble departure diameter on biphilic surfaces for enhanced pool boiling heat transfer performance.” *Int. J. Heat Mass Transf.*, 150.

Lin, S., Zhao, H., Zhu, L., He, T., Chen, S., Gao, C., and Zhang, L. (2021). “Seawater desalination technology and engineering in China: A review.” *Desalination*, 498, 114728.

Liyanaarachchi, S., Shu, L., Muthukumaran, S., Jegatheesan, V., and Baskaran, K.

- (2014). “Problems in seawater industrial desalination processes and potential sustainable solutions: A review.” *Rev. Environ. Sci. Biotechnol.*, 13(2), 203–214.
- Maliani, O. D., Bekkaoui, A., Baali, E. H., Guissi, K., Fellah, Y. El, and Errais, R. (2020). “Investigation on novel design of solar still coupled with two axis solar tracking system.” *Appl. Therm. Eng.*, 172(October 2019), 115144.
- Manikandan, V., Shanmugasundaram, K., Shanmugan, S., Janarthanan, B., and Chandrasekaran, J. (2014). “Energy, exergy and entropy analysis of a single-slope floating-cum-tilted wick-type solar still.” *Int. J. Ambient Energy*, 35(1), 2–12.
- Masoudi, A., Irajizad, P., Farokhnia, N., Kashyap, V., and Ghasemi, H. (2017). “Antiscalting Magnetic Slippery Surfaces.” *ACS Appl. Mater. Interfaces*, 9(24), 21025–21033.
- Matin, A., Rahman, F., Shafi, H. Z., and Zubair, S. M. (2019). “Scaling of reverse osmosis membranes used in water desalination: Phenomena, impact, and control; future directions.” *Desalination*, 455(September 2018), 135–157.
- Mchale, J. P., and Garimella, S. V. (2010). “International Journal of Multiphase Flow Bubble nucleation characteristics in pool boiling of a wetting liquid on smooth and rough surfaces.” *Int. J. Multiph. Flow*, 36(4), 249–260.
- Moita, A. S., Teodori, E., and Moreira, A. L. N. (2015). “Influence of surface topography in the boiling mechanisms.” *Int. J. Heat Fluid Flow*, 52, 50–63.
- Motezakker, A. R., Sadaghiani, A. K., Çelik, S., Larsen, T., Villanueva, L. G., and Koşar, A. (2019). “Optimum ratio of hydrophobic to hydrophilic areas of biphilic surfaces in thermal fluid systems involving boiling.” *Int. J. Heat Mass Transf.*, 135, 164–174.
- Mousavi, S. M. A., and Pitchumani, R. (2022). “Mineral scaling on brass and aluminum surfaces with a range of wettability.” *Surfaces and Interfaces*, 34(September), 102379.
- Može, M., Vajc, V., Zupančič, M., Šulc, R., and Golobič, I. (2021). “Pool Boiling Performance of Water and Self-Rewetting Fluids on Hybrid Functionalized Aluminum Surfaces.” *Processes*, 9(6), 1058.
- Može, M., Zupančič, M., and Golobič, I. (2020). “Pattern geometry optimization on

superbiphilic aluminum surfaces for enhanced pool boiling heat transfer.” *Int. J. Heat Mass Transf.*, 161.

Može, M., Zupančič, M., Steinbücher, M., Golobič, I., and Gjerkeš, H. (2022). “Nanosecond Laser-Textured Copper Surfaces Hydrophobized with Self-Assembled Monolayers for Enhanced Pool Boiling Heat Transfer.” *Nanomaterials*, 12(22).

Mu, L., Xu, X., Williams, T., Debroux, C., Gomez, R. C., Park, Y. H., Wang, H., Kota, K., Xu, P., and Kuravi, S. (2019). “Enhancing the performance of a single-basin single-slope solar still by using Fresnel lens: Experimental study.” *J. Clean. Prod.*, 239, 118094.

Najafpour, S., Moosavi, A., and Rad, S. V. (2020). “2-D microflow generation on superhydrophilic nanoporous substrates using epoxy spots for pool boiling enhancement.” *Int. Commun. Heat Mass Transf.*, 113, 104553.

Najid, N., Hakizimana, J. N., Kouzbour, S., Gourich, B., Ruiz-García, A., Vial, C., Stiriba, Y., and Semiat, R. (2022). “Fouling control and modeling in reverse osmosis for seawater desalination: A review.” *Comput. Chem. Eng.*, 162, 107794.

Panchal, H., and Sathyamurthy, R. (2020). “Experimental analysis of single-basin solar still with porous fins.” *Int. J. Ambient Energy*, 41(5), 563–569.

Pangwa, N., and Msomi, V. (2022). “Progress made in eliminating factors affecting solar stills productivity.” *Mater. Today Proc.*, 57, 969–974.

Peebles, F. N., and Garber, H. (1953). “Studies on the motion of gas bubbles in liquid.” *Chem. Eng. Prog.*, 49(2), 88–97.

Peng, C., Cao, G., Gu, T., Wang, C., Wang, Z., and Sun, C. (2022). “The corrosion behavior of the 6061 Al alloy in simulated Nansha marine atmosphere.” *J. Mater. Res. Technol.*, 19, 709–721.

Pontes, P., Cautela, R., Teodori, E., Moita, A., Liu, Y., Moreira, A. L. N., Nikulin, A., and Barrio, E. P. del. (2020a). “Effect of pattern geometry on bubble dynamics and heat transfer on biphilic surfaces.” *Exp. Therm. Fluid Sci.*, 115(February), 110088.

Pontes, P., Cautela, R., Teodori, E., Moita, A. S., and Moreira, A. L. N. (2020b). “Experimental description of bubble dynamics and heat transfer processes occurring on

the pool boiling of water on biphilic surfaces.” *Appl. Therm. Eng.*, 178(May), 115507.

Poornima, T., Jagannatha, N., and Nityananda Shetty, A. (2010). “Studies on corrosion of annealed and aged 18 Ni 250 grade maraging steel in sulphuric acid medium.” *Port. Electrochim. Acta*, 28(3), 173–188.

Popov, K., Oshchepkov, M., Pervov, A., Golovesov, V., Ryabova, A., Trukhina, M., and Tkachenko, S. (2022). “A Case Study of Calcium Carbonate Crystallization during Reverse Osmosis Water Desalination in Presence of Novel Fluorescent-Tagged Antiscalants.” *Membranes (Basel)*, 12(2).

Radebaugh, R., and Bradley, P. (2018). “Aluminum 6061-T6 (UNS AA96061).” <https://www.nist.gov/>.

Raghupathi, P. A., and Kandlikar, S. G. (2017). “Characterization of Pool Boiling of Seawater and Regulation of Crystallization Fouling by Physical Aberration.” *Heat Transf. Eng.*, 38(14–15), 1296–1304.

Rahman, M. M., and McCarthy, M. (2017). “Boiling Enhancement on Nanostructured Surfaces with Engineered Variations in Wettability and Thermal Conductivity.” *Heat Transf. Eng.*, 38(14–15), 1285–1295.

Rahman, M. M., Pollack, J., and McCarthy, M. (2015). “Increasing Boiling Heat Transfer using Low Conductivity Materials.” *Sci. Rep.*, 5(1), 13145.

Righetti, G., Doretto, L., Sadafi, H., and Hooman, K. (2020). “Water pool boiling across low pore density aluminum foams.” *Heat Transf. Eng.*, 41(19–20), 1673–1682.

Rohsenow, W. M. (1952). “A Method of Correlating Heat-Transfer Data for Surface Boiling of Liquids.” *J. Fluids Eng.*, 74(6), 969–975.

Rokkala, U., Bontha, S., Ramesh, M. R., Balla, V. K., Srinivasan, A., and Kailas, S. V. (2021). “Tailoring surface characteristics of bioabsorbable Mg-Zn-Dy alloy using friction stir processing for improved wettability and degradation behavior.” *J. Mater. Res. Technol.*, 12, 1530–1542.

Rosliza, R., Nora’ Aini, A., and Wan Nik, W. B. (2010). “Study on the effect of vanillin on the corrosion inhibition of aluminum alloy.” *J. Appl. Electrochem.*, 40(4), 833–840.

Saffari, H., Fathalizadeh, H., Moghadasi, H., Alipour, S., and Hosseinalipour, S. M.

(2020). “Experimental study of pool boiling enhancement for surface structuring with inclined intersected mesochannels using WEDM method on copper surfaces.” *J. Therm. Anal. Calorim.*, 139(3), 1849–1861.

Sakthivel, M., Shanmugasundaram, S., and Alwarsamy, T. (2010). “An experimental study on a regenerative solar still with energy storage medium — Jute cloth.” *Desalination*, 264(1–2), 24–31.

Shaffer, D. L., Arias Chavez, L. H., Ben-Sasson, M., Romero-Vargas Castrillón, S., Yip, N. Y., and Elimelech, M. (2013). “Desalination and Reuse of High-Salinity Shale Gas Produced Water: Drivers, Technologies, and Future Directions.” *Environ. Sci. Technol.*, 47(17), 9569–9583.

Shahid, M. K., Mainali, B., Rout, P. R., Lim, J. W., Aslam, M., Al-Rawajfeh, A. E., and Choi, Y. (2023). “A Review of Membrane-Based Desalination Systems Powered by Renewable Energy Sources.” *Water*, 15(3), 534.

Shakier, W. M., Kadhim, A., and Mohammed, A. Z. (2016). “Corrosion Inhibitor for St-37 Alloy by Laser Shock Peening Technique.” *J. Adv. Electrochem.*, 2(1), 56–59.

Shalaby, S. M., El-Bialy, E., and El-Sebaili, A. A. (2016). “An experimental investigation of a v-corrugated absorber single-basin solar still using PCM.” *Desalination*, 398, 247–255.

Shen, Z., Li, J., Xu, K., Ding, L., and Ren, H. (2012). “The effect of synthesized hydrolyzed polymaleic anhydride (HPMA) on the crystal of calcium carbonate.” *Desalination*, 284, 238–244.

Siegel, R., and Keshock, E. G. (1964). “Effects of reduced gravity on nucleate boiling bubble dynamics in saturated water.” *AIChE J.*, 10(4), 509–517.

Singh, H. N., and Tiwari, G. N. (2004). “Monthly performance of passive and active solar stills for different Indian climatic conditions.” *Desalination*, 168, 145–150.

Subramanyam, S. B., Azimi, G., and Varanasi, K. K. (2014). “Designing Lubricant-Impregnated Textured Surfaces to Resist Scale Formation.” *Adv. Mater. Interfaces*, 1(2), 1300068.

Suraparaju, S. K., Dhanusuraman, R., and Natarajan, S. K. (2021). “Performance

evaluation of single slope solar still with novel pond fibres.” *Process Saf. Environ. Prot.*, 154, 142–154.

Thiagarajan, S. J., Yang, R., King, C., and Narumanchi, S. (2015). “Bubble dynamics and nucleate pool boiling heat transfer on microporous copper surfaces.” *Int. J. Heat Mass Transf.*, 89, 1297–1315.

Tolubinsky, V. I., and Kostanchuk, D. M. (1970). “Vapour bubbles growth rate and heat transfer intensity at subcooled water boiling.” *Int. Heat Transf. Conf.*, 23(4).

Trdan, U., Ocaña, J. L., and Grum, J. (2011). “Surface modification of aluminium alloys with Laser Shock Processing.” *Stroj. Vestnik/Journal Mech. Eng.*, 57(5), 385–393.

Tuo, Y., Zhang, H., Chen, W., and Liu, X. (2017). “Corrosion protection application of slippery liquid-infused porous surface based on aluminum foil.” *Appl. Surf. Sci.*, 423, 365–374.

Tzachristas, A., Kanellopoulou, D. G., Koutsoukos, P. G., Paraskeva, C., and Sygouni, V. (2022). “The effect of surface wettability on calcium carbonate precipitation in packed beds.” *Surfaces and Interfaces*, 34(September), 102354.

Venkatesan, A., and Wankat, P. C. (2011). “Simulation of ion exchange water softening pretreatment for reverse osmosis desalination of brackish water.” *Desalination*, 271(1–3), 122–131.

Verwey, E. J. W. (1947). “Theory of the Stability of Lyophobic Colloids.” *J. Phys. Colloid Chem.*, 51(3), 631–636.

Visser, J. (1995). “Particle adhesion and removal: a review.” *Part. Sci. Technol.*, 13(3–4), 169–196.

Walunj, A., and Sathyabhama, A. (2018). “Comparative study of pool boiling heat transfer from various microchannel geometries.” *Appl. Therm. Eng.*, 128, 672–683.

Wang, P., Zhang, D., and Qiu, R. (2012). “Liquid/solid contact mode of superhydrophobic film in aqueous solution and its effect on corrosion resistance.” *Corros. Sci.*, 54, 77–84.

Wang, X., Liang, K., Xu, J., Wang, J., and Chen, X. (2023). “Experimental study on bubble dynamics and heat transfer of pool boiling at sub-atmospheric pressures.” *Int.*

Commun. Heat Mass Transf., 148(September), 107065.

Xhanari, K., and Finšgar, M. (2019). “Organic corrosion inhibitors for aluminum and its alloys in chloride and alkaline solutions: A review.” *Arab. J. Chem.*, 12(8), 4646–4663.

Yu, P., Lian, Z., Xu, J., and Yu, H. (2021). “Slippery liquid infused porous surfaces with corrosion resistance potential on aluminum alloy.” *RSC Adv.*, 11(2), 847–855.

Yu, X., Xu, N., Yu, S., Han, Y., and Chu, H. (2023). “Effect of orthogonal channel structure on the heat transfer in pool boiling and its heat flux prediction model.” *Int. J. Therm. Sci.*, 187(January), 108193.

Yuan, G., Liu, Y., Ngo, C.-V., and Guo, C. (2020). “Rapid fabrication of anti-corrosion and self-healing superhydrophobic aluminum surfaces through environmentally friendly femtosecond laser processing.” *Opt. Express*, 28(24), 35636.

Zhang, Y., Ma, X., Zhou, J., Lei, Z., and Wei, J. (2022). “Experimental investigation of pool boiling heat transfer on the radial micro-pillar surfaces.” *Appl. Therm. Eng.*, 214(28), 118843.

Zhao, J., Wang, M., Lababidi, H. M. S., Al-Adwani, H., and Gleason, K. K. (2018). “A review of heterogeneous nucleation of calcium carbonate and control strategies for scale formation in multi-stage flash (MSF) desalination plants.” *Desalination*, 442(January), 75–88.

Zhu, T., Yuan, Y., Yu, Q., Xiang, H., Liu, G., Dai, X., and Liao, R. (2023). “Enhanced corrosion resistance of slippery liquid infused porous aluminum surfaces prepared by anodizing in simulated marine atmosphere.” *Mater. Chem. Phys.*, 306, 128073.

Zuber, N. (1959). “Hydrodynamic Aspects Of Boiling Heat Transfer (Thesis).”

Zuber, N. (1963). “Nucleate boiling. The region of isolated bubbles and the similarity with natural convection.” *Int. J. Heat Mass Transf.*, 6(1), 53–78.

LIST OF PUBLICATIONS BASED ON PH.D. RESEARCH WORK

Sr. No.	Title of the paper	Authors	Journal Name, Year, Volume Number, Issue, Pages	Month, year of publication	Category*
1	“Enhanced boiling heat transfer of water on a liquid-infused surface.” https://doi.org/10.1016/j.applthermaleng.2023.120219	A. V. V. R. Prasad, Y., Erick Resendiz, M., Sarada, K., Sathyabhama, A., and Kota, K	<i>Applied Thermal Engineering</i> , 226, 120219 Impact factor: 6.1	February 2023	1
2	“Liquid-infused surfaces for mitigation of corrosion and inorganic scaling.” https://doi.org/10.1016/j.mtcomm.2024.108865	A. V. V. R. Prasad, Y., Sathyabhama, A., Sarada, K., and Kota, K.	<i>Materials Today Communications</i> 39, 108865. Impact factor: 3.7	April, 2024	1
3	“Recent trends in pool boiling enhancement - A qualitative approach”	A. V. V. R. Prasad, Y., Sathyabhama, A.	<i>Advances in Thermal-Fluid Engineering (ATFE 2021)</i> PDEU, Gandhinagar	25-26 March 2021	3

Category* 1: Journal paper, full paper reviewed

2: Journal paper, Abstract reviewed

3: Conference /Symposium paper, full paper reviewed

4: Conference /Symposium paper, Abstract reviewe

A V V R PRASAD Y

Prof. SATHYABHAMA A

Research Scholar

Research Guide

BIO-DATA

Name : A V V R PRASAD Y.
Date of Birth : 28/08/1989
Nationality : Indian
Marital status : Married
Address : Plot No.8-126/1, Veerabhadra Nilayam, Jaysingpur,
Tallapudi (Mandal), West Godavari (District)
Andhra Pradesh, India. 534341.
Mob No : 9533630257
E-Mail ID : avvrprasady@gmail.com, ram1002@gmail.com.



Details of Educational Qualifications: -

Sr. No.	Exam	Institute	Board/ University	Subject /Specialization	Year of passing	% of Marks / CGPA	Class Award
01	Ph.D.	National Institute of Technology, Karnataka, Surathkal, Mangalore, Karnataka, 575025, India	NITK	Mechanical (Boiling heat transfer)	-	8.5	First class with Distinction
02	M.Tech	BVC College of engineering, Odalrevu, Amalapuram, Andhra Pradesh, 533210, India.	JNTU Kakinada	Design Engineering	2013-2016	78	First class with Distinction
03	BE	S.R.K.R Engineering college, Chinnamiram, Bhimavaram,. Andhra Pradesh, 534204, India	Andhra University	Mechanical Engineering	2006-2010	70.31	First class with Distinction

Details of Employment: -

Sr. No.	Organization	Designation	Duration	Period (Years)	Work Done in Brief
01	Lakireddy Bakireddy College of Engineering, Mylavaram, Andhra Pradesh, 521230, India.	Assistant professor in Mechanical Engineering	24/07/2016 to 07/07/2018	2	Teaching
02	BVC Engineering college, Palacharla, Rajahmundry, Andhra Pradesh, 533102, India	Assistant professor in Mechanical Engineering	15-04-2015 To 30-04-2016	1	Teaching